PROCESS MONITORING AND UNCERTAINTY QUANTIFICATION FOR LASER POWDER BED FUSION ADDITIVE MANUFACTURING

A Thesis

by

MOHAMAD MAHMOUDI

Submitted to the Office of Graduate and Professional Studies of
Texas A&M University
in partial fulfillment of the requirements for the degree of

DOCTOR OF PHILOSOPHY

Chair of Committee,	Alaa Elwany
Committee Members,	Raymundo Arróyave
	Shiren Wang
	Bruce Tai
Head of Department,	Mark A. Lawley

August 2019

Major Subject: Industrial Engineering

ABSTRACT

Metal Additive manufacturing (AM) such as Laser Powder-Bed Fusion (LPBF) processes offer new opportunities for building parts with geometries and features that other traditional processes cannot match. At the same time, LPBF imposes new challenges on practitioners. These challenges include high complexity of simulating the AM process, anisotropic mechanical properties, need for new monitoring methods.

Part of this Dissertation develops a new method for layerwise anomaly detection during for LPBF. The method uses high-speed thermal imaging to capture melt pool temperature and is composed of a procedure utilizing spatial statistics and machine learning.

Another parts of this Dissertation solves problems for efficient use of computer simulation models. Simulation models are vital for accelerated development of LPBF because we can integrate multiple computer simulation models at different scales to optimize the process prior to the part fabrication. This integration of computer models often happens in a hierarchical fashion and final model predicts the behavior of the most important Quantity of Interest (QoI). Once all the models are coupled, a system of models is created for which a formal Uncertainty Quantification (UQ) is needed to calibrate the unknown model parameters and analyze the discrepancy between the models and the real-world in order to identify regions of missing physics.

This dissertation presents a framework for UQ of LPBF models with the following features: (1) models have multiple outputs instead of a single output, (2) models are coupled using the input and output variables that they share, and (3) models can have partially unobservable outputs for which no experimental data are present. This work proposes using Gaussian process (GP) and Bayesian networks (BN) as the main tool for handling UQ for a system of computer models with the aforementioned properties. For each of our methodologies, we present a case study of a specific alloy system. Experimental data are captured by additively manufacturing parts and single tracks to evaluate the proposed method. Our results show that the combination of GP and BN is a powerful and flexible tool to answer UQ problems for LPBF.

DEDICATION

To my mother.

ACKNOWLEDGMENTS

First and foremost, I would like to express my sincere gratitude to my adviser Dr. Alaa Elwany for the continuous support of my doctorate study. Without his patience, guidance, motivation, and excellent supervision this work could not have accomplished. His helped me in all the time of research and writing my papers and dissertation. I could not have imagines having a better mentor for my PhD study.

Second, I want to thank my committee members: Dr. Raymundo Arroyave, Dr. Shiren Wang, and Dr. Bruice Tai, as well as Dr. Ibrahim Karaman and Dr. Ji Ma, for their continued guidance, support, advice and suggestions that made possible reaching the objectives of this dissertation.

I also want to thank Dr. Jeffery Hart who always made time for me and answered my questions.

Many thanks to all my excellent and intelligent colleagues, Dr. Gustavo Tapia, Dr. Luke Johnson, Bing Zhang, Dr. Brian Franco, Kubra Karayagiz, and Raiyan Seede for always working extremely hard, while at the same time making work more enjoyable and motivating.

Doing research has its ups and downs, but something that kept me motivated and going particularly toward the end was my life partner, Mrs. Tessa Mahmoudi. I thank her and apologize for the nights I could not come home early.

Last but not the least, I would like to thank my family: my parents, my sister, and my lovely aunt. They supported my in so many ways throughout my PhD study and my life as well.

CONTRIBUTORS AND FUNDING SOURCES

Contributors

This work was supervised by a dissertation committee consisting of committee chair, Professor Alaa Elwany of the Department of Industrial and Systems Engineering, and committee members, Professor Raymundo Arroyave of the Department of Materials Science and Engineering, Professor Shiren Wang of the Department of Industrial and Systems Engineering, and Professor Bruce Tai of the Department of Mechanical Engineering.

Section 2.2 of this dissertation was conducted in collaboration with Dr. Ahmed Aziz Ezzat of Rutgers University.

Chapter 3.2, 3.3, and 4.3 of this dissertation were conducted in collaboration with Professor Ibrahim Karaman of the Department of Materials Science and Engineering and Dr. Ji Ma of University of Virginia School of Engineering and Applied Sciences.

Portions of this dissertation were conducted with the advanced computing resources and consultation provided by Texas A&M High Performance Research Computing.

All other work conducted for the dissertation was completed by the student independently.

Funding Sources

Portions of this dissertation were supported by an Early Stage Innovations grant from NASA's Space Technology Research Grants Program, Grant No. NNX15AD71G.

Portions of this dissertation were supported by National Science Foundation through the NSF Research Traineeship (NRT) program under Grant No. NSF-DGE-1545403, "NRT-DESE: Data Enabled Discovery and Design of Energy Materials (D3EM)".

ortions of this dissertation were supported by Army Research Office (ARO) under Grant number W911NF-18-1-0278.

The contents of this dissertation are solely the responsibility of the authors and do not necessarily represent the official views of Texas A&M University, National Aeronautics and Space

Administration (NASA), National Science Foundation (NSF), or Army Research Office (ARO).

NOMENCLATURE

AM	Additive Manufacturing
LPBF	Laser Powder Bed Fusion
UQ	Uncertainty Quantification
UP	Uncertainty Propagation
ICME	Integrated Computational Materials Engineering
GP	Gaussian Process
BN	Bayesian Network
FE	Finite Element
PF	Phase Field
MCMC	Markov Chain Monte Carlo
SIZER	SIgnificant ZERo crossing of the derivatives
PDAS	Primary Dendrite Arm Spacing
IN718	Inconel alloy 718
Ti-6Al-4V	Titanium alloy with 6 wt.%Al and 4 wt.%V
NiNb	Nickel alloy with 5 wt.%Nb
NiTi	Nickel Titanium alloy
LHS	Latin Hypercube Sampling
MAPE	Mean Average Prediction Error
CV	Cross-validation
FOV	Field of View
GSA	Global Sensitivity Analysis
i.i.d.	Independent and Identically Distributed

QoI	Quantity of Interest
SEM	Scanning Electron Microscopy
EDM	Electrical Discharge Machining
BSE	Back Scattered Electron
OM	Optical Microscopy

TABLE OF CONTENTS

Page

ABSTRACT ii

DEDICATION iii

ACKNOWLEDGMENTS iv

CONTRIBUTORS AND FUNDING SOURCES v

NOMENCLATURE vii

TABLE OF CONTENTS ix

LIST OF FIGURES xi

LIST OF TABLES xiv

1. INTRODUCTION 1

    1.1 Additive Manufacturing 1
        1.1.1 Laser Powder-Bed Fusion 1
        1.1.2 Challenges of L-PBF 2
    1.2 Role of Process Monitoring 3
    1.3 Role of Computer Models 3
        1.3.1 Integrated Computational Materials Engineering (ICME) 4
    1.4 Uncertainty Quantification for AM 4
    1.5 Key definitions 5
    1.6 Gaussian processes 7
    1.7 Organization of the Dissertation 7

2. TOWARDS MONITORING: NOVEL ANOMALY DETECTION FOR LPBF 9

    2.1 Process Monitoring for LPBF 10
    2.2 Methodology 13
        2.2.1 Step 1: Data acquisition 15
        2.2.2 Step 2: Screening 19
        2.2.3 Step 3: Identify and flag 21
        2.2.4 Step 4: Classify 25
    2.3 Experiments 26
        2.3.1 Experimental testbed 26
        2.3.2 Results 28

2.3.3 Comparison of approaches 36

3. MULTI-OUTPUT CALIBRATION OF A SINGLE COMPUTER MODEL 38

3.1 Methodology 38
3.1.1 Multivariate Surrogate Model 39
3.1.2 Multivariate Calibration Model 45
3.2 Experimental setup 50
3.2.1 Melt pool depth and width 50
3.2.2 Melt pool peak temperature 52
3.3 Multivariate calibration of Ti-6Al-4V single tracks 53
3.3.1 Melt pool Modeling through FEM based thermal modeling 54
3.3.2 Building the surrogate model 58
3.3.3 Performance of the calibration 62

4. CALIBRATION OF HIERARCHICAL COMPUTER MODELS 69

4.1 Hierarchical Models 69
4.1.1 UQ for hierarchical models 70
4.2 Methodology 71
4.2.1 Bayesian calibration of hierarchical models 71
4.2.2 Handling lack-of-data 74
4.2.2.1 Prediction 76
4.2.3 Illustrative example 76
4.3 Case Study of LPBF 78
4.3.1 The hierarchical models 78
4.3.1.1 The melt pool model 79
4.3.1.2 The phase field model 81
4.3.2 Coupling models using GP surrogates 83
4.3.3 Experiments 86
4.3.4 Calibration results 88
4.3.5 Discussion 90

5. SUMMARY 94

5.1 Contributions of the Dissertation 94
5.1.1 Contributions of Process Monitoring 94
5.1.2 Contributions of Uncertainty Quantification 95
5.2 Future work 97

REFERENCES 98

APPENDIX A. BAYESIAN NETWORKS 116

APPENDIX B. GLOBAL SENSITIVITY ANALYSIS 119

LIST OF FIGURES

FIGURE Page

1.1 Light Rider ™ is the world's first additively manufactured motorcycle weighing only 35 kilograms 2

2.1 Representative melt pool thermal image captured during laser melting. Reprinted with permission. Copyright © 2019 by ASME. 16

2.2 Process of generating a thermal signature for a rectangular layer. (a) The very first melt pool image captured can be seen at the bottom right corner; (b) more melt pool images are combined as the laser progresses and scans the rest of the rectangle; the arrows schematically show the laser scan path. (c) The complete thermal signature of the layer. Reprinted with permission. Copyright © 2019 by ASME. 18

2.3 (a) Grayscale image for a sample rectangular layer, (b) the binary image with the islands detected after thresholding indicating possible anomalies, (c) ROIs positioned at the centers of the island clusters. Reprinted with permission. Copyright © 2019 by ASME. 20

2.4 The pyrometer used for temperature measurement. Reprinted with permission. Copyright © 2019 by ASME. 28

2.5 (a) Schematic of the prism showing the cavity, (b) as-printed prism. Reprinted with permission. Copyright © 2019 by ASME. 29

2.6 Thermal signature corresponding to layer 151 with the cavity in the center. Reprinted with permission. Copyright © 2019 by ASME. 31

2.7 ROIs detected in the screening step corresponding to the thermal signature of the faulty layer 151. Reprinted with permission. Copyright © 2019 by ASME. 32

2.8 Top row: SIZER Output for a faulty ROI, (a) Spatial Detection, (b) Independent Detection. Bottom row: SIZER Output for a faultless ROI, (c) Spatial Detection, (d) Independent Detection. Reprinted with permission. Copyright © 2019 by ASME. 33

2.9 ROC for LR classifier with Spatial Detection (solid red line), with Independent Detection (solid blue line). Dashed green line corresponds to random guess. Reprinted with permission. Copyright © 2019 by ASME. 36

3.1 Approximation of T distributions to a normal distribution. 47

3.2 Representative SEM images used for measuring the melt pool depth and width 51

3.3 The two-wavelength pyrometer used for temperature measurement mounted inside the L-PBF machine..... 52

3.4 Temperature map of a sample melt pool captured using the pyrometer 53

3.5 Sample output of the melt pool model for Ti-6Al-4V powder on a Ti-6Al-4V substrate, showing the melt pool temperature profiles in three-dimensions [1]..... 55

3.6 Histograms and kernel density estimates of the posterior distributions for the roughness parameters $\boldsymbol{r}$ for the surrogate model..... 60

3.7 Results of a 10-fold cross validation of the surrogate model for (a) melt pool depth, (b) melt pool width, and (c) melt pool peak temperature..... 61

3.8 Histograms and kernel density estimates of the posterior distributions for calibration parameters (a) θ_1: laser absorptivity, (b) θ_2: powder-bed porosity, and (c) θ_3: thermal conductivity of the liquid 64

3.9 Results of the 6-fold cross validation for the predictions using the calibrated model for (a) y_1: melt pool depth, (b) y_2: melt pool width, and (c) y_3: melt pool peak temperature 66

3.10 Results of the 6-fold cross validation for the predictions using the calibrated model with only two outputs (a) y_1, (b) y_2 68

4.1 Hierarchical modeling in LPBF 70

4.2 Schematic showing the process of coupling a melt pool model with a solidification (phase field) model using the intermediate data processing..... 71

4.3 Graph of a sample hierarchical network of simulation models 72

4.4 Bayesian network for a two-model system with unobservable variables..... 73

4.5 Bayesian network of a two-model system with unobservable response for model 1 .. 74

4.6 Histograms and kernel density estimates of the posterior distributions for the example parameters and hyperparameters..... 77

4.7 Cross validation for M_2 78

4.8 Relationships between the variables of a two-model system..... 79

4.9 A sample outputs of the melt pool model 80

4.10 A sample output of the phase field model..... 83

4.11 Cross-validation of GP surrogates for (a) melt pool width, W; (b) solidification gradient at the tail, G_0; and (c) primary dendrite arm spacing, λ 86

4.12 Sample melt pool from a single track and segregation 87

4.13 Histograms and kernel density estimates of the posterior distributions for calibration parameters for (a) the melt pool model, and (b) the phase field model 89

4.14 Posterior mean estimates for $\hat{y}_{1Q}(\boldsymbol{x};\boldsymbol{\theta}^*), \delta_{1Q}$, and their sum, $y_{1Q}(\boldsymbol{x};\boldsymbol{\theta}^*)$. The experimental observations are shown by the red dots. 91

4.15 Experimental data grid 92

4.16 Contour plots of the prediction error after calibration for (a) $y_{1Q}(\boldsymbol{x};\boldsymbol{\theta_1^*})$ and (b) $y_2(y_{1U}(\boldsymbol{x});\boldsymbol{\theta_2^*})$ 93

A.1 An example of a Bayesian network 117

A.2 Bayesian network representation of a calibration problem 117

A.3 Bayesian network for a system with two hierarchically built models 118

LIST OF TABLES

TABLE Page

2.1 Chemical composition of the 17-4 PH stainless steel powder. Reused with permission. Copyright © 2019 by ASME. 27

2.2 Performance of the four competing classifiers. Bold-faced values indicate lowest errors. Reused with permission. Copyright © 2019 by ASME. 35

2.3 Comparison of the current study with the most relevant commercial and academic studies. Reused with permission. Copyright © 2019 by ASME. 37

3.1 Mean absolute predictive error (MAPE) of the surrogate model for the three outputs 62

3.2 Posterior distribution parameters for the calibration parameters 63

3.3 Mean absolute predictive error (MAPE) of the predictions using the calibrated model 67

4.1 Specifications of the melt pool model 81

4.2 Specifications of the phase field model 84

4.3 Posterior estimates of the calibration parameters 90

1. INTRODUCTION

1.1 Additive Manufacturing

Additive manufacturing (AM) is formally defined by the American Society for Testing and Materials (ASTM) as "the process of joining materials to make objects from 3D model data, usually layer upon layer, as opposed to subtractive manufacturing technologies" [2]. Multiple synonyms have been used to refer to AM since its inception in the early 1980s such as additive layer manufacturing (ALM), 3D printing, solid freeform fabrication (SFF), direct manufacturing, rapid manufacturing and rapid prototyping.

1.1.1 Laser Powder-Bed Fusion

Laser powder-bed fusion (L-PBF) is one of the most common additive manufacturing (AM) processes that produces physical objects directly from a digital computer model through selectively fusing raw material in powder form using a high energy laser beam [3]. Commercial L-PBF technologies include selective laser sintering (SLS) for processing polymeric powders, and selective laser melting (SLM) or direct metal laser sintering (DMLS) for processing metallic powders. The focus of the current work is on metal L-PBF processes that have been reported to successfully process a variety of metallic materials and alloys including stainless steels [4, 5, 6, 7, 8, 9], titanium alloys [10, 11], thermoelectric materials [12], nickel-based super alloys [13], and shape memory alloys [14, 15, 16, 17, 18, 19, 20].

Metal L-PBF is characterized by a broad spectrum of capabilities, often associated with AM technologies, such as high degrees of geometric freedom, ability to customize parts, and material saving through design and topology optimization. An example of design optimization is shown in Fig. 1.1 where a motorcycle was manufactured with minimum weight while ensuring the frame was strong enough to handle the stresses of various driving scenarios. Other emerging capabilities continue to evolve, including the potential of producing parts with tailored spatially-varying properties, commonly known as functional grading [21, 22].

Figure 1.1: Light Rider ™ is the world's first additively manufactured motorcycle weighing only 35 kilograms

Mechanical properties of L-PBF parts depend primarily on their microstructure (e.g. grain size and morphology), which, in turn, is influenced by the thermal history during manufacturing, i.e. cooling rates, thermal gradients and reheating cycles [23, 24]. Careful characterization of part microstructure under various process settings is pivotal toward understanding process-property relationships.

1.1.2 Challenges of L-PBF

Metal L-PBF is characterized by a broad spectrum of capabilities, often associated with AM technologies, such as high degrees of geometric freedom, ability to customize parts, and material saving through design and topology optimization. Other emerging capabilities continue to evolve, including the potential of producing parts with tailored spatially-varying properties, commonly known as functional grading [21, 22]. Despite the promising potential, the process is highly prone to defects that are likely to compromise part quality such as delamination[25, 26], pores and cracks, [27, 10], insufficient fusion [28], and poorly formed weld beads [29], among many others. Kleszczynski et al [28] provide a detailed overview of defects in metal L-PBF. Consequently, a myriad of research efforts focus on addressing this challenge.

1.2 Role of Process Monitoring

One approach calls for experimentally identifying process maps. These are windows of manufacturing process parameter combinations within which certain types of defects are avoided or minimized; see for example [30, 31, 32]. This approach is both time- and cost-intensive, but also material- and sometimes even system-specific. That is, a processing map developed for a particular material or on a particular commercial AM system is not agnostic and cannot be generalized to other materials and systems. Another approach is to use process modeling and simulation to understand the underlying physics of the process and identify the root causes of these defects; see for example [33, 34, 35, 36]. This approach circumvents the challenge associated with the experimental approach since these models are based on first principles. One drawback in this approach is the fact that physics-based models that simulate L-PBF are very complex and computationally expensive, making them more suited for understanding the physical phenomena associated with the process than practically conducting process design and optimization. Hence, the use of process monitoring and control to identify and mitigate defects has been suggested as an alternative approach.

1.3 Role of Computer Models

L-PBF processes offer attractive advantages and capabilities over conventional manufacturing techniques. These include, for example, higher geometric freedom, flexibility to customize parts, and recently the potential capability of tailoring the microstructures (and hence the properties) of fabricated parts. However, they are in the meantime very complex processes that involve several physical mechanisms most of which are not yet fully understood. Therefore, it is crucial to develop better understanding of these mechanisms that drive the thermal history within the part during fabrication. Ideally, in-situ thermal monitoring can be used to capture information about thermal histories during fabrication. However, experimental measurement of the thermal field in L-PBF is extremely difficult due to a number of challenges such as very high thermal gradients and cooling rates, micro-scale melt pool size, and emissivity variations, among many other challenges. Conse-

quently, numerical methods are needed to complement experiments in understanding the thermal history during the fabrication of L-PBF parts.

The disagreement between the real-world and the model outputs can be attributed to one or more of the following factors: (1) incomplete understanding of the physical system, (2) incomplete information about model parameters, (3) incorrect values for the model inputs, (4) natural stochastic behavior of the system, and (5) uncertainties associated with available numerical simulation algorithms [37, 38, 39, 40, 41]. Hence, identification, characterization, and quantification of the uncertainties associated with these models become necessary in order to strengthen the robustness of model predictions, which is in turn essential if one is to use the models to guide the design/optimization of the systems (in this case, materials).

1.3.1 Integrated Computational Materials Engineering (ICME)

Integrated Computational Materials Engineering (ICME) prescribes a framework for the acceleration in the development and deployment of materials through the establishment and exploitation of process-structure-property-performance (PSPP) relationships. PSPPs in turn can be established through linking materials models at multiple length (and possibly time) scales. The goal in ICME is to optimize the materials, manufacturing process, and component designs prior to part fabrication [38]. Inherently, ICME involves utilization of physics-based simulation models that help understand the behavior of complex systems. These models use the system governing equations to compute and predict specific quantities of interest (QoIs). As a well-established fact, all of these simulation models are imperfect and thus their predictions will differ from the actual physical phenomena they are trying to describe.

1.4 Uncertainty Quantification for AM

As an independent field of study, Uncertainty Quantification (UQ) seeks to address the challenges associated with the (unknown) uncertainties in models used to describe the behavior of complex systems. UQ is an established field that has been successfully applied to many areas including climate models [42], computational fluid dynamics [43], forestry [44], nuclear engineer-

ing [45], and econometrics [46]. Although UQ is a key need for computational materials models [47, 48], there is a literature gap in this area [16]. Chernatynskiy et al. [39] present a review of the few existing works on UQ of multi-scale simulation models. More recently, Tapia et al. [16] conduct UQ for a physics-based precipitation model of nickel-titanium shape memory alloys through combining experimental and computer simulation data.

In this work we conduct formal UQ for a computational materials model used to predict melt pool characteristics in L-PBF metal AM processes. More specifically, we perform statistical calibration of an FEM based thermal model via surrogate (or reduced order) modeling and Bayesian inference. The statistical calibration problem (also known as the inverse UQ problem) refers to making inference on the posterior distributions of a set of calibration parameters such that model predictions are in agreement with experimental observations [49]. To the best of the authors' knowledge, the current work is the first to conduct such rigorous calibration using a multivariate Gaussian Process-based (GP) surrogate model. While the focus of the work is on specific physical phenomena associated with L-PBF AM, the overall framework can be readily adapted to address similar problems that involve systematic calibration of complex multiple-output computational materials models.

1.5 Key definitions

Before we introduce the mathematical formulations, we establish notation and some definitions. Since the word *model* will be employed to refer to different types of models that constitute the building blocks of the framework, we clearly define specific cases to avoid misinterpretation and ambiguity. We use *computer model* to denote a computational model implemented via a computer code that simulates and recreates any process (physical, social, mathematical, etc.) by a set of calculations derived from proper study of the process. One example of a computer model is the thermal model explained in Section 3.3.1. The term *statistical model* will refer to the calibration methodology presented in this section, and is sub-divided in two key components: the *surrogate model* and the *calibration model*, which will be defined in the following paragraphs.

Previous approaches for the calibration of computer models using rigorous statistics rely on

Monte Carlo (MC) methods. While MC methods are extremely valuable and well-studied, the fact that they necessitate generating sufficiently large numbers of simulations (sometimes in the order of 15,000 - 20,000 simulations) makes them impractical for calibrating computationally expensive models. One possible approach to overcome this challenge is using a two-stage approach based on surrogate modeling (also called meta-modeling or emulation) and suggested in a series of works [50, 51, 52, 53]. The *surrogate model* is thus the computationally efficient statistical approximation of the original computer model.

In the calibration problem, whether or not a surrogate model is used, we distinguish between two different types of inputs to the computer model [16]:

- *Control inputs* (denoted by $\boldsymbol{x}$) are inputs to the computer model that are directly set to known pre-determined values by the user. Examples of control inputs in some computer models include temperature, pressure, or velocity.

- *Calibration parameters* (denoted by $\boldsymbol{\theta}$) are inputs or parameters to the computer model that are unknown with certainty, or not measurable, at the time of simulation, but do influence the results of the computations. Examples include material properties or unknown physical constants.

The goal of the *calibration model* is thus to estimate the calibration parameters such that the computer model simulations agree with experimental observations of the real process being simulated [16]. In mathematical notation, the statistical model follows the equation:

$$\boldsymbol{y}^E(\boldsymbol{x}) = \boldsymbol{y}^S(\boldsymbol{x}, \boldsymbol{\theta}^\star) + \boldsymbol{\delta}(\boldsymbol{x}) + \boldsymbol{\epsilon} \tag{1.1}$$

where the experimental observation $\boldsymbol{y}^E$ of the real process run at some values of control inputs $\boldsymbol{x}$ is equal to the summation of the response of the computer model $\boldsymbol{y}^S$, a discrepancy (or inadequacy) function $\boldsymbol{\delta}$, and some measurement error $\boldsymbol{\epsilon}$, and the objective is to estimate the values of the calibration parameters $\boldsymbol{\theta}^\star$. Detailed definitions for each term in Equation (1.1) will be provided as we describe the two stages of the statistical model in the following subsections.

1.6 Gaussian processes

The statistical models in this work are developed based on Gaussian process . Gaussian processes offer appealing mathematical and computational properties, flexibility and richness in modeling dependence among data observed in space, and the ability to incorporate a wide range of smoothness assumptions [54, 55, 16]. It is important to point out that a wide variety of powerful data-driven predictive modeling techniques exists, such as artificial neural networks, support vector machines, and logistic regression. These techniques are more commonly used in the context of the classification problem in machine learning [56], and typically rely on the availability of datasets with large enough sizes, since with small datasets there may exist gaps between samples, or only limited different classification cases may be provided [57].

1.7 Organization of the Dissertation

This Dissertation is organized in the following structure. In Chapter 2 we propose a method for layerwise anomaly detection LPBF. The method uses high speed thermal imaging to capture melt pool temperature and is composed of the a four-step anomaly detection procedure. We validate the proposed method using a case study on a commercial LPBF system custom-instrumented with a dual-wavelength imaging pyrometer for capturing the thermal images during fabrication.

Next, in Chapter 3 we switch to UQ for LPBF, because in-situ monitoring only provides partial information and simulations may be necessary to have a comprehensive understanding of the thermo-physical conditions to which the deposited material is subjected. We address this challenge through linking thermal models to experiments via a computationally efficient surrogate modeling approach based on multivariate Gaussian processes (MVGPs). The MVGPs are used to calibrate the parameters of the thermal model against experiments, sidestepping the use of prohibitively expensive Monte Carlo-based calibration. We demonstrate the framework on the calibration of a thermal model for laser powder bed fusion AM of Ti-6Al-4V against experiments carried out over a wide window in the process parameter space. Our work's applicability is wide as the proposed framework could potentially be used in many other ICME-based problems where it is essential to

link expensive computational materials science models to available experimental data.

In Chapter 4, we take the next step toward ICME and present a framework for calibration of multiple models when they are connected in a hierarchical fashion. Additionally, we address an important problem of existence of unobservable response in the network of simulation models using the notion of Bayesian networks. A case study of NiNb singlet tracks is then presented where two models are connected hierarchically with unobservable variables present.

The dissertation is concluded in Chapter 5 where a summary of implications, concluding remarks and potential future extensions are outlined.

2. TOWARDS MONITORING: NOVEL ANOMALY DETECTION FOR LPBF*

In this Chapter we present a novel anomaly detection framework for LPBF processes. Our focus is on detecting anomalies as a proxy for monitoring the process health. Prior works on monitoring L-PBF processes can be generally classified according to the *process signatures* under consideration. According to the report by NIST [59], process signatures are 'dynamic characteristics of the powder heating, melting, and solidification processes as they occur during the build'. The majority of works in the L-PBF process monitoring literature focus on sensing and analyzing the *melt pool* (the liquid interface between the laser beam and the raw material), because it is well-established that melt pool characteristics such as temperature gradients and geometry are critical factors influencing the outcome of the process [60, 61, 59].

Notable advances in developing hardware and sensors to monitor L-PBF processes have been reported to date, and more ongoing research is being conducted to improve existing sensors and develop new ones. In the meantime, these advances have not been adequately matched with methods to analyze the data acquired by these sensors to improve part quality as is the case in traditional manufacturing technologies. Some recent works have started to emerge for polymer AM processes including [62, 63, 64] that focus on polymer-based AM processes such as Fused Deposition Modeling (FDM). Fewer works have developed methods for metal AM such as [65, 66, 67]. The current work focuses on addressing this literature gap in metal AM processes, with focus on L-PBF.

Process control in metal L-PBF starts with providing the capability to detect deviations in process conditions that are potentially correlated with defects. Only upon being able to detect these deviations can actions and protocols be devised to mitigate their undesirable outcomes through feedback or feedforward control. Our focus is on the first step noted above. More specifically, we propose a data-driven framework for detecting layer-wise process anomalies in metal L-PBF through leveraging process monitoring data. The framework involves the use of data anlaytics

*Parts of this section have been reprinted with permission from M. Mahmoudi, A. A. Ezzat, and A. Elwany, "Layerwise anomaly detection in laser powder-bed fusion metal additive manufacturing," *Journal of Manufacturing Science and Engineering*, vol. 141, no. 3, p. 031002, 2019. Copyright © 2019 by ASME.

to detect process anomalies through analyzing melt pool characteristics captured using high speed thermal imaging. The thermal imaging system captures the temperature of the melt pools generated by the fast-moving laser beam within a given layer. These thermal images of the melt pools at a given layer are then processed to generate a process signature. Details of the process signature used in this work can be found in Section 2.2. Next, a spatial statistics model is used synergistically with supervised and unsupervised machine learning techniques to detect process anomalies within the layer, prior to processing the next layer. In this context, we define process anomalies to be regions of the process signatures that deviate from reference conditions. The performance of our proposed framework is tested for anomalies that are caused by a particular class of cavity defects. It has been reported in previous studies that cavity defects ranging between $50\,\mu\mathrm{m}$ to $750\,\mu\mathrm{m}$ in size are common in metal L-PBF and are usually attributed to inadequate fusion between successive layers [68, 69]. In addition to identifying whether or not a certain layer is defective, the framework also determines the location of defects on a micro scale. As will be demonstrated in the case study, we have been able to detect $750\,\mu\mathrm{m}$ diameter cavities.

2.1 Process Monitoring for LPBF

As noted previously, the literature on developing hardware and sensors for monitoring AM processes is rich. Mani et al [59] and Spears and Gold [70] review in-situ sensing techniques in the literature on selective laser melting (SLM). Tapia and Elwany [3] and Everton et al. [71] present more general surveys of process monitoring for metal AM. More recently, Grasso and Colosimo [60] conduct a comprehensive review on process defects and in-situ monitoring methods for metal L-PBF.

In the specific case of L-PBF, thermal imaging systems comprise a large proportion of the published works. In a series of studies [72, 73, 74, 75, 76], two types of detectors, namely, a photodiode and a near-IR CMOS camera, are used to capture melt pool radiation intensity and dimensions (length, width, and area). In [72, 73], a feedback control method is proposed where the observed process variable is the melt pool area, and the control input is the laser power. A controller acts on the difference between the observed area and a reference set point. Although the

authors show that the feedback control method can improve the geometric accuracy at overhang regions, the set point needs to be determined experimentally for every different set of process parameters. In [76], the melt pool data is logged at comparatively high frame rates ($10\,\mathrm{kHz}$ to $20\,\mathrm{kHz}$). Next, depending on whether the melt pool is along the internal hatches or along the slice contours, the melt pool signals are compared to corresponding reference values for possible process errors that might be a result of overheating phenomena at the edges of the part or pores inside the part. Krauss et al [77, 78] use an IR camera to monitor the scanning tracks for detecting process deviations. In [77], the authors study the effect of artificial flaws on the irradiance profile during the scanning of single tracks. In [78], a heat dissipation model is employed to monitor the local changes in heat flow that causes inhomogeneity in the part. Both of these works [77, 78], focus on process 'sensing' rather than 'monitoring'. In other words, they focus on analyzing the effects of process parameters and scan strategies on measured quantities. In another series of works [79, 80, 81, 82, 83] a two-wavelength pyrometer and a CCD camera are used to measure melt pool radiations and heat affected zone (HAZ) radiations, respectively. Again, instead of developing an effective monitoring method, it is only shown that the signals from the sensing devices are sensitive to the variation in process parameters (e.g. laser power and hatch spacing). More recently, an in-situ monitoring method that conducts data mining for infrared images taken from the process plume is proposed in [84] for a particular defect encountered in the fabrication of alloys with low melting points. The proposed method aims at detecting unstable melting conditions caused by excessive heat via analyzing the salient properties of the plume. The method uses a multivariate control-charting scheme to monitor plume emissions for detecting anomalies. The authors rely on the assumption that statistical descriptors of plume radiations are stable over time under in-control fabrication conditions.

The advances in hardware and sensor systems for L-PBF have allowed most of the original equipment manufacturers (OEMs) to integrate in-situ sensing modules and some preliminary data analysis into their commercial systems. EOS [85] has developed a monitoring suite with the potential for quality assurance, which has multiple components for evaluating process conditions

such as powder bed integrity, melt pool characteristics, and chamber temperature. Particularly, the EOSTATE MeltPool Monitoring uses a photodiode to measure the light emitted from the melt pool, and the EOSTATE Exposure OT uses a near-IR sCMOS camera that takes pictures of the entire layer. Multiple algorithms are available in the EOS proprietary software that require threshold parameters from the user, potentially offering the capability of drawing conclusions regarding part quality. Similarly, Renishaw [86] has developed a melt pool monitoring system comprised of three photodiodes: one for in-situ sensing of the input intensity of the laser, and two other photodiodes that separately measure the IR melt pool radiations and the visible plasma emissions. These sensor data is combined with time-synchronized motion control position instructions which can be used to generate 2D and 3D mappings for every build. These mappings have the potential to be combined with appropriate data analysis algorithms for further process monitoring.

Additionally, some preliminary studies use high resolution visual imaging techniques, in contrast to thermal imaging, for monitoring metal L-PBF. In [66], a high resolution consumer grade digital camera is used to obtain images of the powder bed just after recoating and immediately after laser scanning is done. These images are then indexed to the part geometry using a binary template created from the sliced 3D model of the part. Next, image segmentation techniques are used to detect lack-of-fusion flaws during fabrication and anomalies of the powder bed. Although a high rate of true positives in prediction was achieved after artificially induced defects are detected in a test part, the rate of false positive predictions was also high. Grasso et al. [87] propose a method for detecting L-PBF defects caused by the local overheating phenomena using a high-speed and high-resolution commercial camera and a combination of data analyses and machine vision system in the visible range. Their method consists of using T-mode Principal Component Analysis (PCA) for image data to identify 'hot spots' whose behaviors are different from other portions of the same layer in terms of pixel intensity patterns over time. An example of applying data analytics for real-time monitoring of FDM can be found in [64]. The authors propose a novel sparse estimation-based classification method to use heterogeneous sensor signals for detecting process anomalies. Other examples of using data analytics for monitoring AM processes can be found in [88, 89].

We conclude that there is a lack of works in the particular case of metal L-PBF to leverage sensor data for conducting process monitoring and subsequent control. This can be attributed to two main reasons. First, the melt pool is small ($100-1000\,\mu\mathrm{m}$ in diameter) and fast-moving ($100-2000\,\mathrm{mm/s}$). Hence, accurately measuring melt pool temperature (or other process characteristics) is a challenging task that is still an active research area. Second, the physics involved in metal L-PBF is more complex than other AM processes (such as fused filament fabrication for polymers), and hence correlating monitored melt pool dynamics with process conditions is difficult.

We address this gap through proposing a framework for generating process signatures using melt pool information to detect process anomalies. The process signatures contain thermal and spatial information from different melt pools within each layer. Next, guided by the process physics, we propose a data-driven framework that exploits the spatial dependence within the thermal image to identify regions with statistically significant temperature deviations from reference conditions.

2.2 Methodology

For the purpose of anomaly detection, we rely on a process signature which is generated using the thermal data from successive melt pools. The reason we utilize the melt pool information for process monitoring is that as a well established fact in metal L-PBF, the melt pool is a proxy for process stability. It is important to point out that although experimental measurement of the true melt pool temperature during metal L-PBF still suffers measurement inaccuracies, we rely on detecting deviations from references conditions. Our proposed methodology is designed to detect 'changes' that happen to the process signature, rather than looking at absolute melt pool temperatures. In other words, if our experimental thermal imaging system has some intrinsic measurement error, nothing will be detected as anomaly as long as the process conditions are unchanged, i.e. their signature matches with that of a benchmark reference part. Additionally, careful calibration of our thermal imaging system which was conducted using a tungsten filament (halogen tungsten lamp) for a range of temperatures between $1500\,^{\circ}\mathrm{C}$ and $2500\,^{\circ}\mathrm{C}$, and high repeatability in the measurements were acknowledged. Put more simply, systematic measurement errors will not be detrimental to the anomaly detection task as long as measurements are conducted with enough

repeatability, because it is based on deviations, in contrast to true values of the temperature. The proposed anomaly detection procedure is comprised of the following steps:

1. **Data acquisition**: acquire process monitoring data for each layer while the part is being fabricated. The process monitoring data from the thermal imaging system is subsequently processed to obtain thermal signatures. For every layer, a signature difference image is generated by subtracting the signature of that particular layer signature from a pre-specified reference signature.

2. **Screening**: for a just-fabricated layer, identify regions of interest (ROIs) representing subsets within the layer that are likely to include an anomaly. This is in contrast to analyzing the entire layer.

3. **Identify and flag**: characterize spatial dependence within these ROIs using a Gaussian process (GP) model, then flag pixels with statistically significant deviations.

4. **Classify**: use a classifier to determine whether an ROI is deemed faulty or faultless. A layer is considered faulty if at least one of the ROIs is faulty.

Before discussing the details of each step, we briefly point out important considerations related to this procedure. First, incorporating domain knowledge from the underlying physics of the process often results in refining and improving data-driven models. In the case of metal L-PBF, the melt pool thermally interacts with its surroundings (through heat transfer mechanisms such as conduction and convection) and thus, thermal images of melt pools naturally exhibit spatial correlations within themselves, i.e., spatially-close thermal measurements are strongly correlated. As such, implicitly assuming independence between thermal measurements is not physically justifiable, and any data-driven method that does not take into account the within-image spatial dependence during anomaly detection is most likely prone to severe false positive rates by mistaking artifacts of inherent spatial dependence for actual process anomalies.

In our research, we model spatial dependence using a GP model, and then employ a statistical test, called spatial SIZER (SIgnificant ZERo crossing of the derivatives) to detect significant

deviations in spatially correlated images [90]. Since fitting spatial models to large datasets often involves heavy computations associated with computationally intensive covariance matrix operations, analyzing thermal signatures of an entire layer is impractical (in fact, likely infeasible), especially in the case of high resolution thermal images, or parts with large cross section areas. For example, in our case study presented in later sections, a $30 \times 27\,\mathrm{mm}^2$ area results in an image with $1300 \times 1000\,\mathrm{pixel}$ for which the covariance matrix will have $1,300,000^2$ elements. Hence, the screening step is needed to narrow down the entire layer into a subset of small regions that are feasible to analyze. This leads to 1) better characterization of local correlation structures through making the assumption of stationarity more credible within sub-regions of the thermal image, also known in geostatistical literature as local stationarity [91], 2) better detection capability through focusing the detection efforts on few, but critical regions of the image, and 3) reducing the computational burden often associated with fitting spatial models to large datasets.

Once the spatial dependence is modeled and pixels with statistically significant deviations are flagged, the classification step is needed to make a final decision on the current status of the process. The classifier takes into account important features corresponding to the flagged pixels including the total number of flagged pixels, position and spatial pattern of the flagged pixels, etc. to indicate if an ROI is anomalous (faulty) or not. The following subsections elaborate the details of the procedure outlined above.

2.2.1 Step 1: Data acquisition

In this study, the melt pool thermal images are captured using a two-wavelength imaging pyrometer by Stratonics Inc. with spatial resolution of $25\,\mu\mathrm{m/pixel}$. Pyrometry is defined as the non-contact measurement of the temperature of a body based on emitted thermal radiations [92]. The two-wavelength pyrometry technique utilized in this work has the important characteristic of being tolerant to emissivity [93, 94]; that is, it is relatively resilient to the change in emissivity in the target being measured. This is important for an application like L-PBF where the processed material goes through different molten and solid phases, each with distinct value of emissivity that might not be known. The pyrometer used in this work takes images at an approximately constant

frame rate that can be adjusted by the user.

A representative melt pool thermal image is depicted in Figure 2.1. The X and Y coordinates are pixel numbers and the Z coordinate is temperature. The thermal image only shows temperatures above $1500\,^{\circ}\mathrm{C}$ that fall within the calibration range of the pyrometer. It can be seen that the melt pool has an oval geometric profile, with its major axis being along the laser scan direction. Other researchers have observed similar melt pool shapes during L-PBF, see for example [95]. Note that high temperature measurements (above $2900\,^{\circ}\mathrm{C}$) are observed at the center of the melt pool. These observations suggest that the metal powder reaches its evaporation temperature, which is consistent with other recent works [33, 96, 97, 98, 99] investigating the physics of melt pool for metal L-PBF. We can generally split each thermal image into two regions: 1) a 'hot region' encompassing the melt pool and its surrounding, and 2) a 'cold region' with low temperatures below the calibration range of the pyrometer. No reliable temperature measurement is available for a cold region. For the melt pool shown in Figure 2.1, the hot region is the color-coded area with temperatures above $1500\,^{\circ}\mathrm{C}$, and the cold region is the remainder of the image.

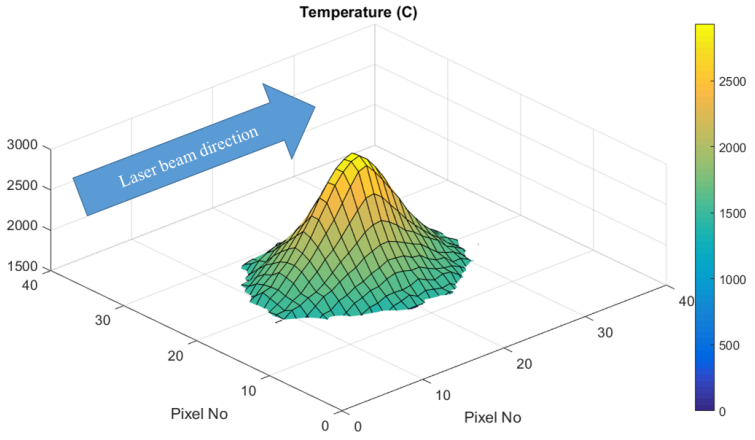

Figure 2.1: Representative melt pool thermal image captured during laser melting. Reprinted with permission. Copyright © 2019 by ASME.

Here, we illustrate the process of generating a (thermal) process signature for a layer with simple geometry in Figure 2.2. Consider an L-PBF machine fabricating a rectangular layer using

45° straight line scans. The thermal imaging system monitors the process and takes images at an approximately constant frame rate. A process signature is then generated for each layer through processing the monitored data and combining all the successive melt pool thermal images within that layer. Figures 2.2a-2.2c show the process of combining the successive melt pool images. Compared to Figure 2.1, the pixel density in Figures 2.2a-2.2c has been decreased by a factor of 3 to reduce the image size and allow for faster computation, which is necessary for a practical layer-wise monitoring application similar to the one proposed in the current work. The very first image can be seen in Figure 2.2a with the melt pool observed in the bottom right corner. Note that the image covers a relatively large area surrounding the melt pool. Using a proprietary algorithm developed by the sensor manufacturer, the imaging system identifies the 'hot spot' in each image, which corresponds to the molten pool boundaries. The measured temperature values are color-coded according to the scale on the right. In Figure 2.2b, we notice that the laser has progressed as schematically shown using the arrows. The arrows show the laser scan path, and the letter h represents a constant hatch spacing. Finally, Figure 2.2c shows the complete layer signature using 950 melt pool images.

For the areas where melt pools overlap (multiple temperature values were measured for a single pixel), the average of the measured temperatures is assigned to each pixel. For the pixels without any temperature measurements (cold regions), we use the 'grand average', defined as the average temperature over all of the pixels in hot regions. The image margins – where no temperature measurement is available – are colored dark blue which corresponds to the grand average. The process signature for the layer under consideration is then used for the next step in the analysis.

Since we are interested in detecting anomalous 'changes' in the process, we compute the difference between the signature shown above, and what we call a corresponding "reference signature". The reference signature can be defined as a signature from a process for which the L-PBF process parameters have been optimized to produce a fully dense defect-free part. An example of process parameter optimization for L-PBF can be found in [100]. Hereinafter, the actual anomaly detection procedure is then performed on the signature difference image, which is obtained by subtracting

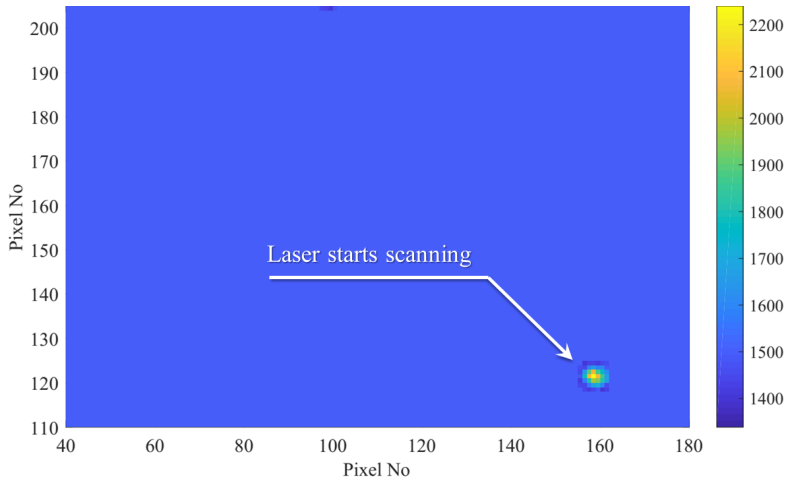

(a)

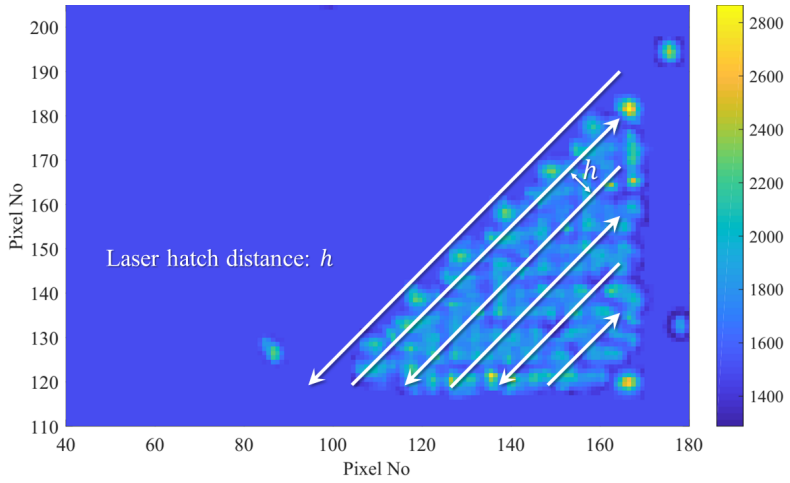

(b)

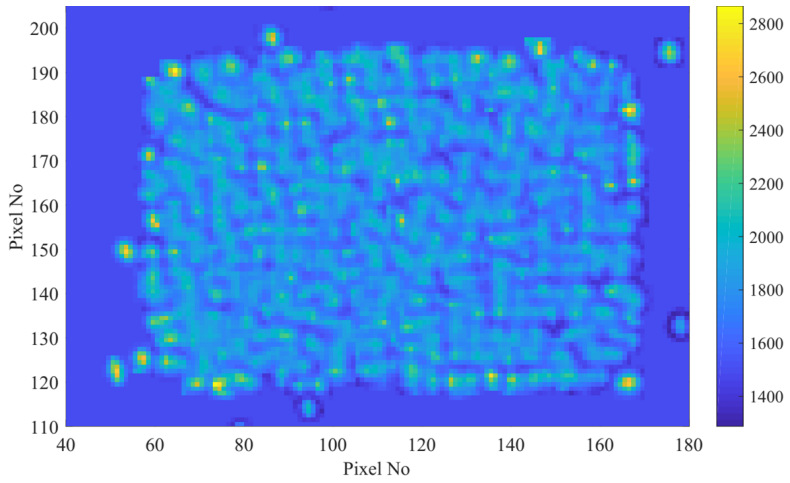

(c)

Figure 2.2: Process of generating a thermal signature for a rectangular layer. (a) The very first melt pool image captured can be seen at the bottom right corner; (b) more melt pool images are combined as the laser progresses and scans the rest of the rectangle; the arrows schematically show the laser scan path. (c) The complete thermal signature of the layer. Reprinted with permission. Copyright © 2019 by ASME.

the layer signature and the corresponding reference signature. In Section 2.3.2, we discuss the choice of reference signatures used to obtain the signature difference, in light of the case study.

2.2.2 Step 2: Screening

The high spatial resolution of the thermal imaging pyrometer ($1300 \times 1000\,\text{pixel}$) and the small size of the melt pool deems the implementation of data-driven anomaly detection on the entire signature difference impractical and time-intensive. The screening step is thus necessary to narrow down the spatial domain to be analyzed, through electing smaller ROIs with higher likelihood of containing anomalies.

Screening consists of the following steps:

1. **Convert to grayscale image**: with intensity values between 0 and 1 from the signature difference. Figure 2.3a shows a grayscale image for a sample layer with rectangular cross section.

2. **Construct binary image**: using the thresholding technique in image segmentation (refer to [101]) to locate pixels whose intensities are too high or too low (below 20th percentile or above 80th percentile of the intensity levels), indicating deviation of the thermal signature from the reference signature. Representative output from this thresholding step is shown in Figure 2.3b. The light colored areas are in fact groups of interconnected deviating pixels (called 'islands' in the text) that are the results of applying thresholding to the grayscale image in Figure 2.3a.

3. **Clustering**: use k-means clustering to find the cluster centroids for these clusters of islands, as shown in Figure 2.3c. The colored dots mark the centroids of each island, and the crosses mark the cluster centroids. This step essentially enables defining ROIs with high density of potential faults. We position the ROI centers at the cluster centroids. The ROI boundaries are shown in Figure 2.3c using rectangles. These ROIs are the ones that will be spatially modeled and analyzed using the spatial SIZER method and the classifier presented next.

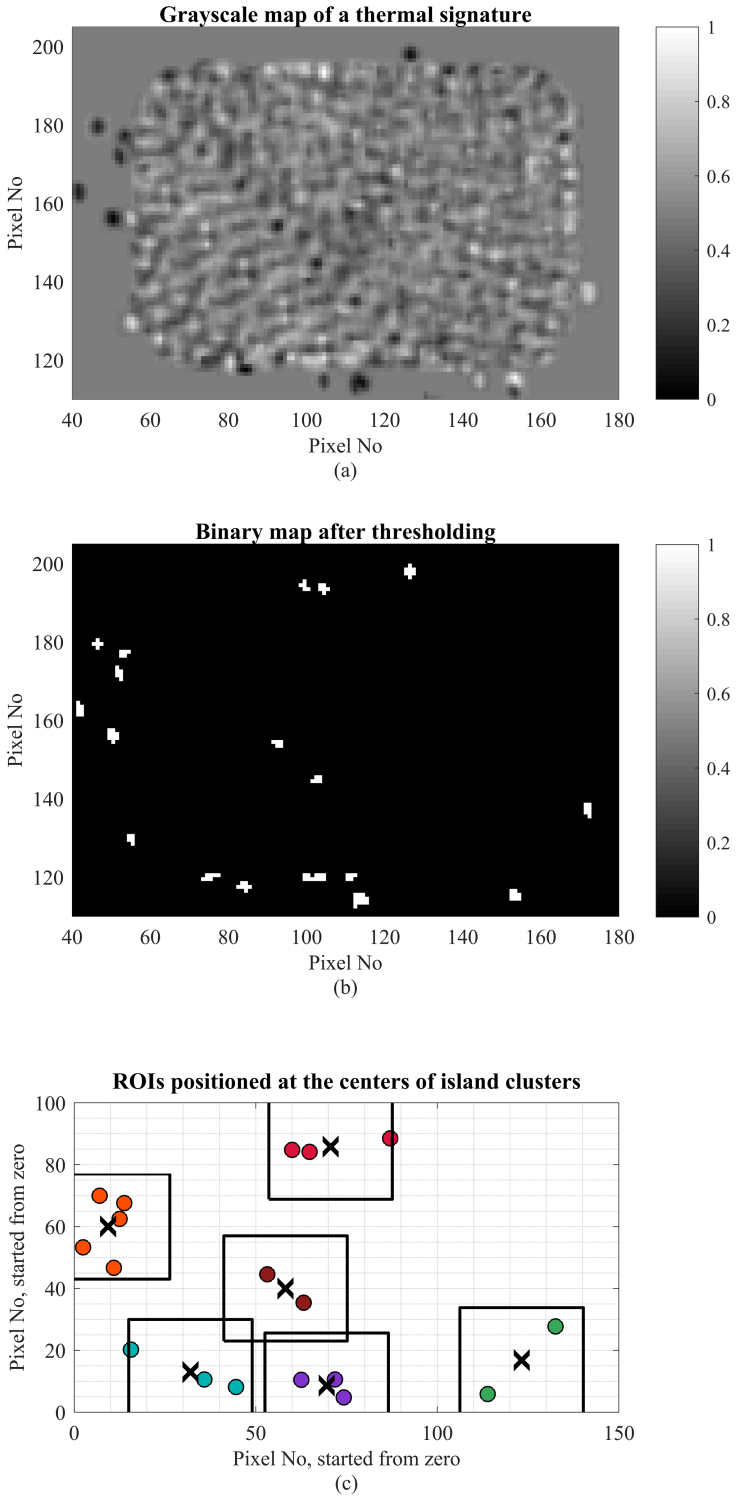

Figure 2.3: (a) Grayscale image for a sample rectangular layer, (b) the binary image with the islands detected after thresholding indicating possible anomalies, (c) ROIs positioned at the centers of the island clusters. Reprinted with permission. Copyright © 2019 by ASME.

We highlight some implementation aspects to the reader's attention. First, note that the thresholding method used in the screening step involves a number of parameters, e.g. cut-off intensity values and minimum island size. In our study, these parameters are selected conservative screening is guaranteed at the layer level. In later stages of the methodology (Steps 3-4), we perform the final and more accurate anomaly detection at the ROI level. Second, in this work the ROIs are assumed to have a rectangular shape due to their convenience when using the spatial SIZER method. Third, the size (dimensions) of ROIs can vary depending on the available computation power. Larger ROIs require longer computation times and one should adjust the ROI size in a way that allows for reasonably fast anomaly detection. Finally, the number of clusters should be adjusted such that minimum overlap exists between the ROIs. Hence, this parameter also depends on the choice of ROI dimensions.

2.2.3 Step 3: Identify and flag

Consider a set of signature difference data, which is regarded as a matrix of temperature difference observations denoted by $\boldsymbol{Y} = Y_{ij}$, where $i = 1, .., n$ and $j = 1, ..., m$ are indices of the pixel locations at which Y_{ij} is observed. To account for spatial dependence, we model $\boldsymbol{Y}$ using a GP model, defined as the sum of a signal value $\boldsymbol{s} = \{s_{ij}\}$ and an error term $\boldsymbol{\epsilon} = \{\epsilon_{ij}\}$, $\forall\, i, j$, such that

$$Y_{ij} = s_{ij} + \epsilon_{ij}, \tag{2.1}$$

where the terms ϵ_{ij} are zero-mean normally distributed errors with a covariance matrix, for which the entries are computed using a pre-specified covariance structure. The challenge in GPs is how to model this covariance structure between any pair of observations through a positive-definite parametric form. Assuming isotropy, the Matérn covariance function is a popular choice [54], which only depends on the spatial distance between any pair of locations, and is denoted hereinafter by $C(d; \Theta)$, where Θ is the vector of covariance parameters and d is the spatial distance.

Since we are interested in detecting potential anomalies in spatially dependent signature difference images, we extend the spatial SIZER method, initially proposed for signalling significant

temperature changes in climate applications [90], to our problem setting. Earlier versions of SIZER which assumed statistical independence were first proposed in the statistical literature [102, 103]. Recently, the spatial SIZER method was proposed, which takes into account spatial correlations to detect statistically significant decadal temperature changes taking place over some regions of the Earth. In Algorithm 1, we present the main steps of the spatial SIZER method in the context of detecting anomalies in spatially correlated signature differences. In the sequel, these steps are explained, however, we refer the interested reader to [90] for details regarding general underlying theory and implementation.

Algorithm 1 Spatial SIZER method for spatially-dependent signature differences

0. Input the observations $\boldsymbol{Y}$ peculiar to an ROI obtained through the screening step, as outlined in Section 2.2.2.
1. Estimate the signal $\boldsymbol{s}$ by convolving a bivariate Gaussian kernel with the data $\boldsymbol{Y}$.
2. Get the MLE estimates $\hat{\Theta}$ for the covariance parameters.
3. Estimate the norm of the signal's gradient, denoted by $\boldsymbol{G}(\boldsymbol{s}) = \{G(s_{ij})\}\ \forall\, i, j$.

repeat

4. Initialize $i = 1$.

repeat

5. Initialize $j = 1$.
6. Conduct a test of hypothesis with $H_0 : \hat{G}(s_{ij}) = 0$.

if H_0 is rejected **then**

7. Y_{ij} is flagged as a potential anomaly.

end if

8. $j = j + 1$

until $j > m$

9. $i = i + 1$

until $i > n$

10. Compute $r^f \equiv$ ratio of the number flagged pixels to the total number of pixels in the ROI.
11. Compute $n^f \equiv$ number of flagged islands in the ROI.
12. Compute $C_{max} \equiv$ maximum island size in the ROI.

As prescribed in Algorithm 1, the procedure of spatial SIZER goes as follows. The spatial SIZER takes as input each ROI obtained through the screening step. First, estimates for the signal

$\boldsymbol{s}$ are obtained by convolving a bivariate Gaussian kernel with the data $\boldsymbol{Y}$, such that

$$\hat{\boldsymbol{s}}_\ell = \boldsymbol{K}_\ell * \boldsymbol{Y}, \tag{2.2}$$

where $*$ denotes the discrete bivariate convolution operator, $\boldsymbol{K}_\ell = K_\ell(i,j)\ \forall\ i,j$; and ℓ is the kernel bandwidth, which is assumed to be the same for both dimensions. The kernel K_ℓ is modeled as the product of two univariate Gaussian kernels such that $K_\ell(i,j) = K_\ell(i)K_\ell(j)$, where

$$K_\ell(i) = \frac{\exp(-(\frac{i}{\ell})^2/2)}{\sum_{i'=1-n}^{n-1}\exp(-(\frac{i'}{\ell})^2/2)}. \tag{2.3}$$

Next, spatial dependence is modeled by estimating Θ through Maximum Likelihood Estimation (MLE). To perform anomaly detection, the norm of the signal's gradient, denoted by $\boldsymbol{G(s)}$ is estimated as

$$\hat{\boldsymbol{G}}(\boldsymbol{s}) = \sqrt{\hat{\boldsymbol{g}}_1^2 + \hat{\boldsymbol{g}}_2^2}, \tag{2.4}$$

where $\hat{\boldsymbol{g}}_1$ and $\hat{\boldsymbol{g}}_2$ are the estimates for the partial derivatives in the vertical and horizontal directions, respectively, and are computed as

$$\hat{\boldsymbol{g}}_1 = \boldsymbol{K}_{\ell,1} * \boldsymbol{Y}, \tag{2.5}$$

$$\hat{\boldsymbol{g}}_2 = \boldsymbol{K}_{\ell,2} * \boldsymbol{Y}, \tag{2.6}$$

where $K_{\ell,1}(i,j) = K'_\ell(i)K_\ell(j)$, $K_{\ell,2}(i,j) = K_\ell(i)K'_\ell(j)$ and $K'_\ell(i) = (-\frac{i}{\ell})K_\ell(i)$.

Once the estimates of the signal's gradient are obtained, a test of hypothesis is conducted for each pixel with the null hypothesis $H_0 : \hat{G}(s_{ij}) = 0$. Simply speaking, at any given pixel, if the gradient of the signal is close to zero, then the observation at that pixel would be deemed faultless. Otherwise, the null hypothesis is rejected, indicating a potential anomaly (fault) at that pixel location. Assuming bivariate Gaussian distribution for $(\hat{g}_1, \hat{g}_2)^T$, the null hypothesis can be re-written as $H_0 : (\hat{g}_1, \hat{g}_2)^T \sim \mathcal{N}(\mathbf{0}, \boldsymbol{\tau})$, where $\boldsymbol{\tau} = \begin{pmatrix} \tau_1^2 & \tau_{12}^2 \\ \tau_{21}^2 & \tau_2^2 \end{pmatrix}$.

Spatial dependence in the anomaly detection is accounted for in the hypothesis test through the entries of $\boldsymbol{\tau}$, which are expressed in terms of the parametric covariance C, where

$$\hat{\tau}_1^2 = Var(\hat{g}_1(i,j)) = \sum_{i'=1}^{n}\sum_{j'=1}^{m}\sum_{i''=1}^{n}\sum_{j''=1}^{m} K_{\ell,1}(i-i',j-j')K_{\ell,1}(i-i'',j-j'')C(d_{(i',j'),(i'',j'')};\hat{\Theta}). \tag{2.7}$$

The entry $\hat{\tau}_2^2$ is computed similary, and

$$\hat{\tau}_{12}^2 = \hat{\tau}_{21}^2 = Cov(\hat{g}_1,\hat{g}_2) = \sum_{i'=1}^{n}\sum_{j'=1}^{m}\sum_{i''=1}^{n}\sum_{j''=1}^{m} K_{\ell,1}(i-i',j-j')K_{\ell,2}(i-i'',j-j'')C(d_{(i',j'),(i'',j'')};\hat{\Theta}). \tag{2.8}$$

More details about the derivations of these expressions are explained in [90]. Once these values have been computed, they are plugged in to compute the quantities $(\hat{t}_1,\hat{t}_2)^T$, which are the test statistics of this hypothesis test and are defined as $\hat{\boldsymbol{\tau}}^{-0.5}(\hat{g}_1,\hat{g}_2)^T = (\hat{t}_1,\hat{t}_2)^T \sim \mathcal{N}(\mathbf{0},\boldsymbol{I})$, where $\boldsymbol{I}$ is a 2×2 identity matrix. As such, the summation of the squares of $(\hat{t}_1,\hat{t}_2)$ follows a χ^2-distribution. Only when $\hat{t}_1^2+\hat{t}_2^2 > q_{\chi_2^2}(\alpha)$, is the null hypothesis rejected, i.e. Y_{ij} is flagged as a potential anomaly, where α is a pre-specified confidence level and $q_{\chi_2^2}$ is the corresponding quantile.

Once the procedure has been implemented on each pixel in the ROI and pixels with statistically significant deviations are flagged, a decision on whether the entire ROI is considered as an anomaly or not has yet to be taken. For that purpose, we collect some useful information about the spatial pattern of the flagged pixels. Similar to our definition in Section 2.2.2, by 'islands' we refer to a group of interconnected flagged pixels (1's) from a background of unflagged pixels (0's). Finding these islands is a standard problem in computer science referred to as the island count problem and is solved using the standard Depth First Search (DFS) algorithm [104]. As such, the following features are extracted from the output of spatial SIZER to guide the final decision:

1. ratio of the number flagged pixels to the total number of pixels in the ROI, denoted by r^f,
2. number of flagged islands in the ROI, denoted by n^f,
3. maximum island size in the ROI, denoted by C_{max},

Our choice of the above features is motivated by the following observations. First, the choice of r^f is straightforward; it is intuitive that the higher the number of flagged pixels in an ROI, the higher the likelihood that the entire ROI is anomalous. Our experimental observations, however, suggest that r^f alone, despite being an important factor, often fails to find a clear-cutting threshold between faulty and faultless ROIs, and that the pattern of the flagged pixels within the ROI is another equally important factor that should not be overlooked. For example, consider two ROIs with equal number of flagged pixels, then an ROI that has large groups of interconnected flagged pixels concentrated in a specific area is more likely to contain a fault, in contrast to an ROI with randomly scattered flagged pixels. A similar observation was made in [105] for quality control in high-precision manufacturing. As such, in addition to r^f as an important feature at the pixel level, important features related to the spatial pattern of the flagged pixels need to be considered. Our feature selection experiments have revealed that the number of islands, and the maximum size of these islands have high explanatory power in detecting whether an entire ROI represents an anomaly. These features are used as inputs to the classifier discussed in the subsequent section.

2.2.4 Step 4: Classify

The objective of the final step in our anomaly detection framework is to indicate whether the current process status is in- or out-of-control, which is accomplished by performing the anomaly detection at the ROI level (in contrast to the higher resolution analysis at the pixel level). Ideally, we would like to have at hand a ready-to-use classifier that, given the outputs of spatial SIZER, namely r^f, n^f, and C_{max}, would render a final output as either “0" or “1" indicating a faultless and faulty ROI, respectively.

In reality, however, such classifier does not exist, and we need to build that classifier based on observed data. For that purpose, we generate a training dataset that includes both faulty and faultless ROIs to train that classifier. In practice, that would correspond to the phase of L-PBF process optimization which typically involves some trial-and-error experiments that result in the fabrication of both faulty and faultless parts. The thermal data corresponding to these parts can then be analyzed as described in Sections 2.2.2 and 2.2.3 and used as training data for the classifier. In

Section 2.3, we discuss in detail the experiments carried out to generate these training data.

Given the training data, we can use one of the widely used classifiers in the machine learning literature to carry out the final anomaly detection step. In this work, we compared the performance of the following common classifiers: (1) logistic regression (LR), (2) k-Nearest Neighbors (kNN) ,(3) support vector machines (SVM) and (4) random forests (RF) [106]. In Section 2.3.2, we the result of comparing these classifiers in our problem setting is presented.

2.3 Experiments

We validate and assess the performance of the proposed anomaly detection framework outlined in Section 2.2 through experiments conducted on a commercial L-PBF system custom instrumented with a thermal monitoring sensor as detailed next.

2.3.1 Experimental testbed

Test specimens were fabricated on a 3D Systems ProX$^{\text{TM}}$ DMP 100 equipped with a Gaussian profile fiber laser with wavelength $\lambda = 1070\,\mathrm{nm}$, beam spot size of approximately $70\,\mu\mathrm{m}$-diameter and a maximum power of $50\,\mathrm{W}$. Metallic parts can be fabricated within a build envelope of $10 \times 10 \times 10\,\mathrm{cm}$ under an Argon inert protective atmosphere to minimize oxidation. The user has control over the manufacturing process parameters used during fabrication such as laser power, laser scanning speed, hatch spacing (distance between two successive passes of the beam within the same layer), layer thickness, inert gas concentration, among others.

Test parts for this study were built in 17-4 precipitation hardening Stainless Steel (SS) powder produced using gas atomization under argon inert atmosphere. The chemical composition is given in Table 2.1. The powder size distribution (PSD) is $10\,\mu\mathrm{m} < \mathrm{D50} < 13.5\,\mu\mathrm{m}$ and $\mathrm{D80} < 22\,\mu\mathrm{m}$, where D*xx* denotes the cumulative distribution, that is, *xx*% of the particles in a given powder batch have diameters that size or smaller. Samples were fabricated on a 430F SS substrate plate, and subsequently removed from the plate using wire electric discharge machining (EDM).

A high-speed two-wavelength imaging pyrometer (ThermaVIZ$^{\text{TM}}$ by Stratonics Inc.) was integrated with the system through a custom-designed mounting bracket shown in Figure 2.4. The

Table 2.1: Chemical composition of the 17-4 PH stainless steel powder. Reused with permission. Copyright © 2019 by ASME.

Element	Fe	Cr	Ni	HC Cu
Concentration (%)	70 – 80	10 – 25	1.0 – 10	1.0 – 10

pyrometer consists of two high resolution CMOS imaging detectors for measuring the melt pool radiations and converting them into temperature values using two-wavelength pyrometry. Both detectors have a field of view (FOV) of $1300 \times 1000\,\mathrm{pixel}$ mapped to a $30 \times 27\,\mathrm{mm}$ area, which yields a spatial resolution of $24\,\mu\mathrm{m}$ per pixel. When recording at the full FOV size ($1300 \times 1000\,\mathrm{pixel}$), a frame rate of $100\,\mathrm{Hz}$ can be achieved. Both the spatial and temporal resolution can be increased through decreasing the FOV, e.g. a $2.8\,\mathrm{kHz}$ frame rate is achieved when working with a $600 \times 50\,\mathrm{pixel}$ FOV. These settings of the imaging system present a number of advantages. First, the adjustable frame rate is useful to achieve the desired imaging rate according to the laser scan velocity. Faster imaging rates are needed for generating the process signatures in builds with high laser scan velocity. As we will mention in Section 2.3.2, for the case study in this work a frame rate of $250\,\mathrm{Hz}$ proved to work. Second, the fine spatial resolution allows us to get a detailed temperature profile across the melt pool along with spatial temperature gradients – see Figure 2.1. The high resolution is vital for generating the process signature required for our anomaly detection framework. Third, when the pyrometer is operated fast enough, temporal temperature gradients can be measured. The temperature gradients give insight about heating and cooling rates across the melt pool, which are indeed important for studying the physical phenomena that occur in during L-PBF.

A rectangular prism with dimensions $5.5 \times 8 \times 9\,\mathrm{mm}$ was fabricated using the setup described above. The part was fabricated with a powder layer thickness of $30\,\mu\mathrm{m}$, thus it consisted of exactly 300 layers. Optimized values of the process parameters including laser scan speed and laser power were chosen based on an earlier study by the co-authors [100] to maximize part density. The study conducted a novel accelerated process optimization that significantly reduced the number of experiments by utilizing experimental data from previous studies in the literature as the initial data

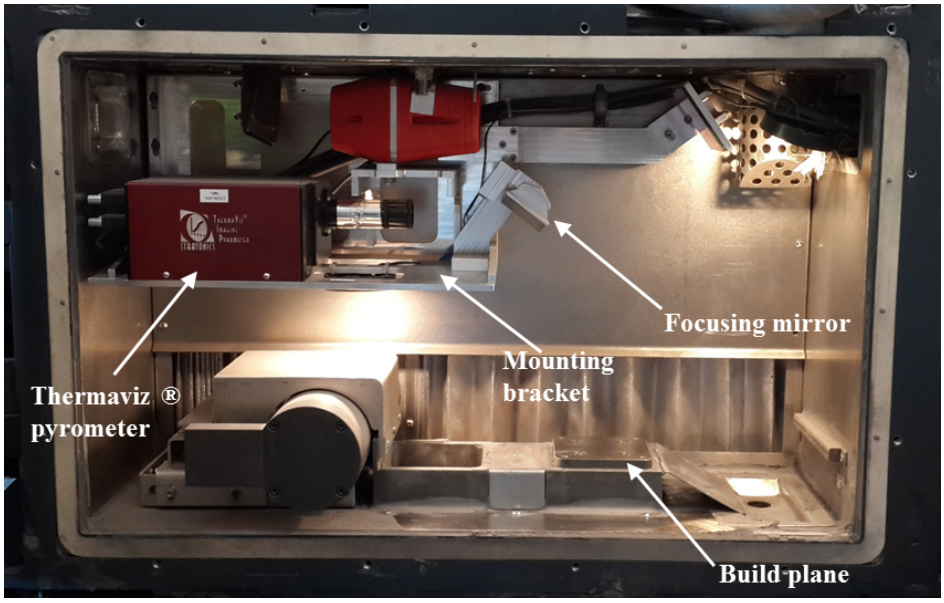

Figure 2.4: The pyrometer used for temperature measurement. Reprinted with permission. Copyright © 2019 by ASME.

to guide the sequential optimization experiments. The final average part density was reported to be 99.20% [100]. An artificial defect was induced into the solid model of the part, represented by the cylindrical cavity illustrated in Figure 2.5a. The part was then fabricated within the pyrometer FOV to capture the thermal images from each layer (Figure 2.5b). We induced a cylindrical cavity with diameter $750\,\mu\mathrm{m}$ and height $150\,\mu\mathrm{m}$ at the center of the part to mimic porosity defects for metal L-PBF. A similar defect generation method has been used in other works that study defects in metal L-PBF, see for example [66, 107]. The $150\,\mu\mathrm{m}$ height of the artificial defect implies that only 5 layers located in the center of the part (layers 150-154) are faulty and the rest of the layers (295 layers) are faultless.

2.3.2 Results

We start by selecting a specific layer among the 5 faulty layers including the cavity as a “test layer" that we will use to evaluate the performance of our proposed method. Figure 2.6 shows the thermal signature for layer 151 corresponding to one of the faulty layers. This process signature was captured with the pyrometer operating at $250\,\mathrm{Hz}$ frame rate following the procedure in Section

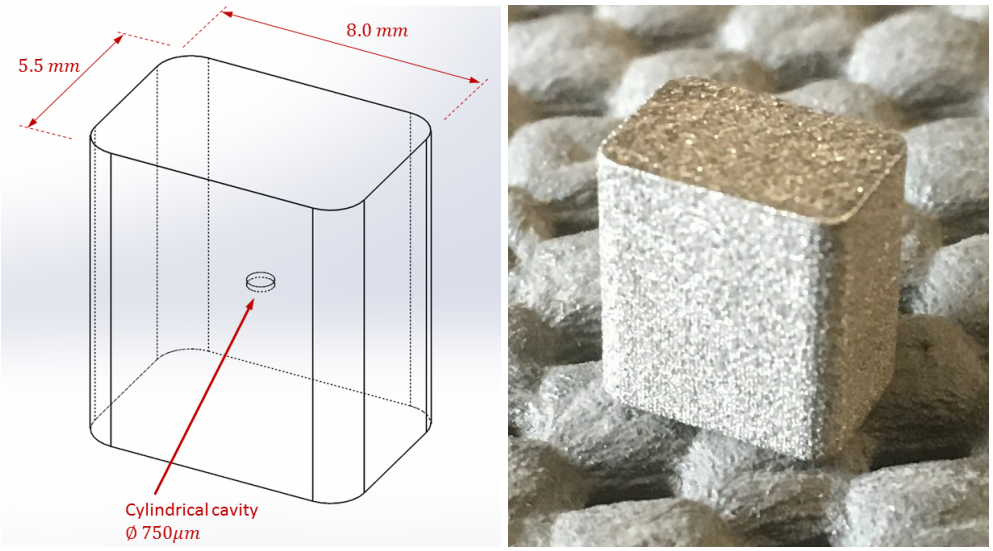

(a) (b)

Figure 2.5: (a) Schematic of the prism showing the cavity, (b) as-printed prism. Reprinted with permission. Copyright © 2019 by ASME.

2.2.1 through superimposing approximately 1000 individual melt pool thermal images. A cold region near the center due to the artificially induced defect is easily observed.

It is worth mentioning that the choice of frame rate depends on a number of factors such as the build size, laser scan speed, and melt pool size. If the laser runs at very high speeds, the imaging system should be set to capture thermal images at higher frame rates. Generally, the more melt pool images captured per layer, the more information the corresponding process signature contains. Our anomaly detection framework requires a process signature composed of a sufficient number of melt pools; an example is shown in Figure 2.2(c). In this paper, our objective is to demonstrate the capabilities of our proposed anomaly detection framework given a fast enough imaging system. A more thorough analysis of optimizing the imaging system settings necessitates further investigation beyond the scope of the current work.

After selecting that test layer and generating its thermal signature, we need to generate the signature difference $\boldsymbol{Y}$. As explained in Section 2.2.2, a reference signature is needed to generate this signature difference. In our case, any of the 295 layers that were printed without the cavity

defect can be used for generating the reference signature since the sample was manufactured with optimal process parameters ensuring a fully dense part. It is important to point out that in practical settings, the reference signature is ideally extracted from a defect-free part that has been tested after fabrication. In the most general case, for a specific part with complex geometry, different layers indeed have distinct shapes. This means that successful detection of anomalies requires 'layer-specific' reference signatures. In other words, a fully dense certified part should accompany a database of reference signatures. This database can be generated automatically as the part is fabricated. Note that the reference signature does not have to belong to a single fully dense part. In fact, a specific layer can have multiple reference signatures taken from the same layer of multiple fully dense parts. Based on our experiments, using multiple fully dense parts to generate the reference signatures improves anomaly detection accuracy because the additional information from multiple reference parts enables the supervised learning (classifier algorithm) to capture natural variability inheret to the fabrication process.

In the current study, we make the simplifying assumption that the reference signature is extracted from a previous layer within the same part since we know that these previous layers were fabricated using optimized process parameters, have an identical shape to the test layer, and do not include an artificially induced defect.

Although one reference signature out of the 295 suffices to generate a signature difference (since these layers are identical), we selected 5 reference signatures to generate more data for testing the proposed method. The thermal signature of the test layer 151 was subtracted from those of the 5 reference signatures, resulting in 5 signature differences. Each of these 5 signature differences has 15 distinct ROIs (obtained using the screening step) randomly scattered throughout. Since the the exact position of the induced cavity is known a priori, only the ROIs that included the cavity were labeled as faulty, and the remainder of the ROIs were labeled faultless. For illustration, Figure 2.7 shows only five out of the fifteen 30×30 pixel ROIs in one of the 5 signature difference images corresponding to the test layer 151. Only the ROI positioned in the center of the thermal image with red outline is known to be faulty. The rest of the ROIs outlined in green are labeled

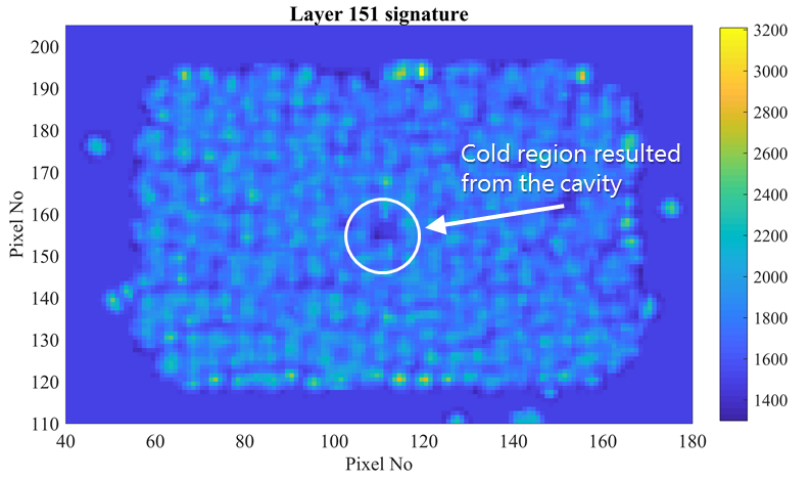

Figure 2.6: Thermal signature corresponding to layer 151 with the cavity in the center. Reprinted with permission. Copyright © 2019 by ASME.

faultless. The size of the ROIs can be adjusted based on the available computational resources, since larger ROIs need more time for implementing spatial SIZER. As such, we have a total of 5 signature differences $\times 15$ ROIs $= 75$ ROIs. These 75 ROIs represent the test dataset needed for classification.

Next, we generate a training dataset to train the classifier using a similar procedure. More specifically, we select 2 additional layers from the 5 layers including the cavity, and 1 faultless layer from the available 295 faultless layers. For each layer, we generate 5 signature difference images, and for each of them we identify 15 ROIs. This results in a training dataset of size 5 signature differences $\times 15$ ROIs $\times 3$ layers $= 225$ ROIs, each labeled as faulty, or as faultless, respectively. The final step is then to train the classifier using this dataset, and then test it using the 75 ROIs from the test layer 151 as described next.

The training and testing ROIs were analyzed using the spatial SIZER method described in detail in Algorithm 1, Section 2.2.3. This implementation took $30\,\text{sec}$ on average using a PC with eight 64-bit cores and 32 GB RAM. Note that in practice, the total computation time for a specific part is directly proportional to the number of ROIs that are detected across all layers during the build process (Total computation time $\approx$ 30 sec $\times$ Number of detected ROIs). Considering most

L-PBF builds take hours and sometimes a few days, computational speed of the proposed method is suitable for online monitoring and control. As described in Section 2.2.4, we then use the outputs of spatial SIZER for all the ROIs to extract values of the explanatory features, which will be used in the classifier. For each ROI, we can assign the three explanatory features $\boldsymbol{x} = \{r^f, n^f, C_{max}\}$, in addition to the ROI label: $y = 1$ (faulty), or $y = 0$ (faultless).

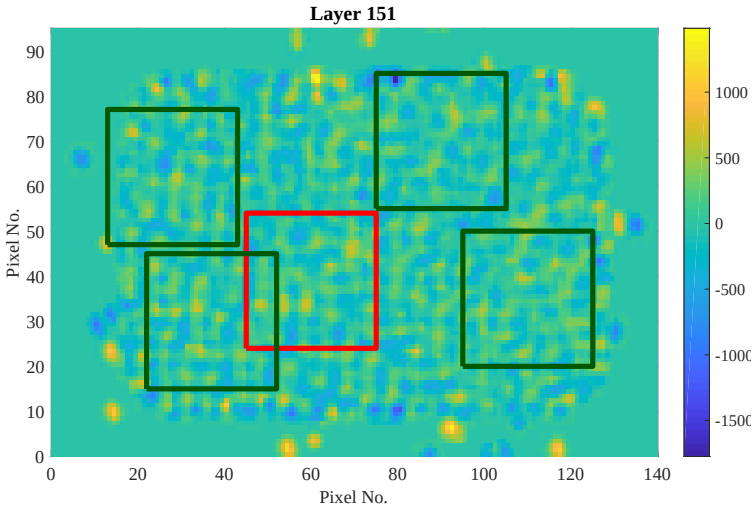

Figure 2.7: ROIs detected in the screening step corresponding to the thermal signature of the faulty layer 151. Reprinted with permission. Copyright © 2019 by ASME.

Four standard classifiers were implemented to obtain predictions for the classes of the 75 test ROIs; namely: LR, SVM, kNN, and RF. For LR, we used a probability threshold of 0.15, above which the ROI was deemed anomalous. The choice of a low threshold value is motivated by the imbalanced nature of anomaly detection problems, where one class (faultless ROIs) is much more abundant than the other (faulty ROIs) in the experimental data. Therefore, a probability threshold that is lower than 0.5 corresponds to assigning higher cost towards misdetecting the anomalous class. This simple adjustment is a common approach in the imbalanced classification literature, often referred to as “cost-sensitive learning" [108]. For kNN, we set the number of neighbors $k = 7$. For SVM, the cost parameter was set at 2.00 and a radial basis kernel was used, while

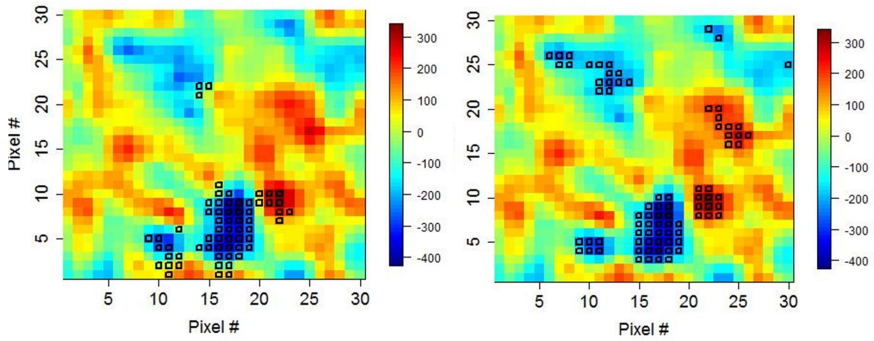

(a) Spatial Detection – Faulty ROI **(b) Independent Detection – Faulty ROI**

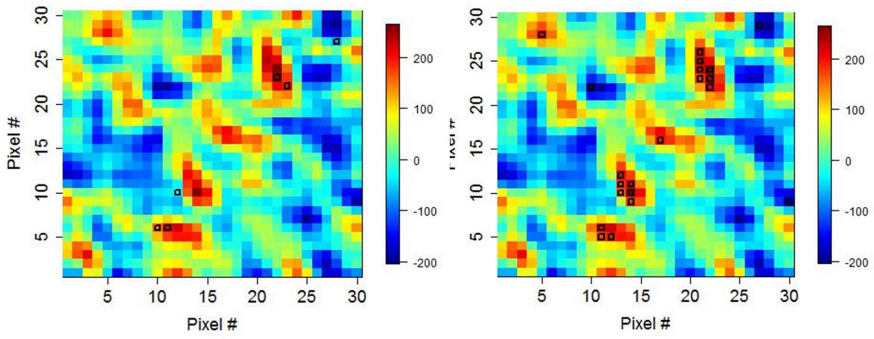

(c) Spatial Detection – Faultless ROI **(d) Independent Detection – Faultless ROI**

Figure 2.8: Top row: SIZER Output for a faulty ROI, (a) Spatial Detection, (b) Independent Detection. Bottom row: SIZER Output for a faultless ROI, (c) Spatial Detection, (d) Independent Detection. Reprinted with permission. Copyright © 2019 by ASME.

for the random forest classifier, the number of trees was set to 100. These parameter values were found to yield reasonable results in our experiments.

In addition, we benchmark our proposed approach against a simpler alternate scenario that does not take into account the spatial dependence between thermal measurements when performing the anomaly detection task. This scenario follows the exact same procedure, with the exception that during the spatial SIZER implementation, as discussed in Section 2.2.3, we substitute the off-diagonal elements in the $\boldsymbol{\tau}$ matrix with zero values, that is $\tau_{12}^2 = \tau_{21}^2 = 0$. We refer to this alternative approach as *Independent Detection*, since it assumes independence between thermal measurements while detecting anomalies, as opposed to our approach, to which we refer as *Spatial Detection*.

Figure 2.8 shows the outputs of SIZER on two different ROIs, where the top row (Panels a and b) correspond to a faulty ROI, and the bottom row (Panels c and d) correspond to a faultless ROI. In all the panels, the flagged pixels showing the detected anomalous features are indicated with dark marks. Figure 2.8a shows the output from Spatial Detection, which is able to specifically pinpoint the exact location of the fault corresponding to the cold region illustrated in Figure 2.6. On the other hand, the Independent Detection, as shown in Figure 2.8b, appears to be associated with an overdetection of faultless features as anomalies (high positive rates). Similarly, for the bottom row, the Spatial Detection hardly signals any features corresponding to a faultless ROI, as opposed to the Independent Detection which falsely flags some pixels as anomalous.

Table 2.2 summarizes the results for the four classifiers in terms of the classification error rate, number of false positives (FPs), and number of false negatives (FNs), for the two scenarios of Spatial and Independent Detection. Classification error rate quantifies the ratio of of mis-classifications to the total number of test points, and is defined as $E = \sum_{i=1}^{n^t} \frac{I(\hat{y}_i \neq y_i)}{n^t}$, where $\hat{y}_i$ and y_i are the predicted and observed classes for the i^{th} ROI, respectively, $I(\cdot)$ is an indicator function which returns 1 when $\hat{y_i} \neq y_i$ and 0 otherwise, and n^t is the total number of test points , i.e. $n^t = 75$ in our case study.

Upon inspecting Table 2.2, it appears that LR outperforms the other four classifiers in terms of

Table 2.2: Performance of the four competing classifiers. Bold-faced values indicate lowest errors. Reused with permission. Copyright © 2019 by ASME.

	Spatial Detection			Independent Detection		
Method	Error rate	FPs	FNs	Error rate	FPs	FNs
LR	**0.04**	2.00	**1.00**	0.13	8.00	2.00
kNN	0.09	**0.00**	7.00	0.08	0.00	6.00
SVM	0.05	1.00	3.00	0.16	6.00	6.00
RF	0.09	**0.00**	7.00	0.12	2.00	7.00

the classification error rate and FNs. For LR with Spatial Detection, only one anomaly is misdetected, while two faulteless ROIs are signaled as anomalies. However, the LR with Independent Detection misses two true faulty ROIs and misclassifies eight faultless ROIs as faulty. Such high rate of false positives, which was noted in Figure 2.8, is most likely due to mistaking the natural artifacts of spatial dependence as anomalies due to the assumption of independence, which agrees with our motivation in Section **??** regarding the importance of taking spatial dependence into account when designing data-driven anomaly detection procedures. Figure 2.9 presents the ROC curve for the LR classifier with Spatial Detection (solid red line) obtained by varying the probability threshold from 0 to 1 with an increment of 0.001 and plotting their respective false positive rate (FPR) versus corresponding true positive rate (TPR). The ROC curve appears to be well far from the diagonal line corresponding to a random classifier, indicating reasonable performance. Choice of a suitable probability threshold for LR can be guided by the ROC. For instance, thresholds in the range between 0.10 to 0.25 appear to maximize the sum of the sensitivity and specificity. The ROC curve for the LR with Spatial Detection appears to dominate the one obtained from the LR classifier with Independent Detection (solid blue line). The area under the curve for the Spatial Detection ROC is found to be 0.95, as opposed to an area of 0.84 corresponding to the Independent Detection, which is a good indicator of classification accuracy.

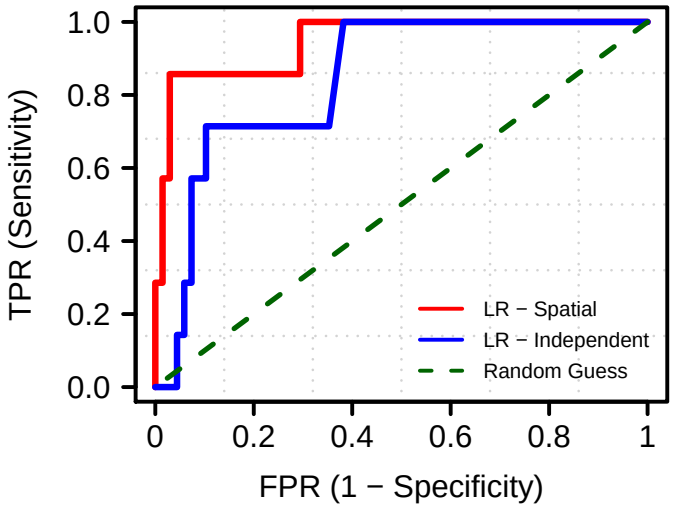

Figure 2.9: ROC for LR classifier with Spatial Detection (solid red line), with Independent Detection (solid blue line). Dashed green line corresponds to random guess. Reprinted with permission. Copyright © 2019 by ASME.

2.3.3 Comparison of approaches

As pointed out in Section 2.1, process monitoring and anomaly detection in metal AM and particularly L-PBF are emerging fields still undergoing development. Hence, benchmark methodologies do not exist to gauge the performance of our anomaly detection framework. Nonetheless, many of the published works share similarities and differences worthy of comparison. Table 2.3 sheds some light on how the current study stands among the most recent and relevant commercial and academic studies. The first important observation is that most studies only consider a specific type of defect that occur in L-PBF and their proposed approach cannot be generalized for detecting other types of defects. Defects of different natures require different sensor setups. One can argue that a comprehensive monitoring system for L-PBF necessitates a select combination of special-purpose sensing modules. From Table 2.3, we notice that depending on the sensor type (photodiode, visual camera, thermal camera, etc.) and its resolution researchers and practitioners have recommended a wide range for the operating frame rates. Thus, very high frame rates do not

necessarily correspond to more effective solutions. On the contrary, appropriately choosing the sensor and process signature might avoid the redundant high costs associated with high-resolution high-frame rate instruments. It can be seen that while most of the prior studies use indirect measurements (visual images or radiations) to generate a process signature, our framework utilizes two-wavelength pyrometry to capture the melt pool temperature which is directly affected by the process dynamics. Lastly, we notice that the accuracy that our framework offers is higher than other approaches reported in the literature.

Table 2.3: Comparison of the current study with the most relevant commercial and academic studies. Reused with permission. Copyright © 2019 by ASME.

	EOS [85]	Renishaw [86]	Grasso et al. [87]	Grasso et al. [84]	Abdelrahman et al. [66]	Current study
Type of defect	NA (only sensing and detection of abnormalities)	NA (only sensing)	Local overheating in over-hang acute corners	Unstable melting due to excessive heat for alloys with low melting point	Lack-of-fusion defects	Lack-of-fusion defects
Sensor setup	One photodiode and one NIR camera	Three photodiodes at different wavelengths	Visible-range camera (Olympus I-speed 3)	IR Camera (FLIR SC3000)	Visible-range camera (Nikon D8003)	Two-wavelength pyrometer (Stratonics)
Frame rate	60 kHz (photodiode), 10 Hz (camera)	100 kHz	300 Hz	50 Hz	2 images per layer	250 Hz
Signature	Radiations from both the melt pool and the entire build plate	Radiations from the melt pool, plasma, and the laser beam	Visual images of the powder bed	Thermal images of the plume	Visual images of the powder bed	Melt pool temperature profiles
Accuracy	NA	NA	Not quantified	Not quantified	Sensitivity: 91.5%, Specificity: 84.0%	Accuracy: 96%, Sensitivity: 85.7%, Specificity: 97.1%

3. MULTI-OUTPUT CALIBRATION OF A SINGLE COMPUTER MODEL*

In this Chapter we present a framework for uncertainty quantification and calibration of a single-computer model with multiple outputs. Prior to this work, UQ of ICME simulation models has been classically conducted using Monte Carlo methods (see [110, 111, 112, 113, 114]). However, for many computationally expensive models, Monte Carlo methods are impractical, and sometimes even unfeasible, as they require sufficiently large numbers of simulation runs in order to acquire the statistics necessary to adequately characterize model uncertainty. This is especially true in the specific case of computational models for AM that tend to be computationally demanding, which precludes the utilization of Monte Carlo methods. To address this, we construct a surrogate model (also known as an emulator or meta-model). This represents a statistical approximation that can be used in lieu of the original computationally expensive simulation model without sacrificing too much accuracy. Although surrogate modeling has been studied in prior works, one important distinguishing feature of the surrogate model developed in the present study is its ability of approximating simulation models that have multiple outputs or QoIs. This is an important feature since multi-output simulation models are quite common in science and engineering applications [115, 116]. Conventional UQ approaches for multi-output models typically ignore correlations that might exist among model outputs, and thus usually conduct independent UQ analysis for each output independently. Clearly, this de-coupling overlooks inherent coupling or interdependence that may exist among multiple outputs of a single model.

3.1 Methodology

After describing the melt pool FEM based simulation model in Section 3.3.1, we now describe in details the multivariate statistical framework that will be employed to calibrate that model. This approach is referred to as *calibration of computer models* by Kennedy and O'Hagan [52]. We

*Parts of this section have been reprinted with permission from M. Mahmoudi, G. Tapia, K. Karayagiz, B. Franco, J. Ma, R. Arroyave, I. Karaman, and A. Elwany, "Multivariate calibration and experimental validation of a 3d finite element thermal model for laser powder bed fusion metal additive manufacturing," *Integrating Materials and Manufacturing Innovation*, vol. 7, no. 3, pp. 116–135, 2018. Copyright © 2018 by Springer-Verlag London Ltd.

emphasize that although AM is our focus application platform, the framework developed in this section can be readily generalized to other problems.

3.1.1 Multivariate Surrogate Model

In this section, we build a multivariate surrogate model that replaces the computer model $\boldsymbol{y}^S(\boldsymbol{x}, \boldsymbol{\theta})$ in Equation (1.1). For detailed derivations, the interested reader is encouraged to study the work by Conti and O'Hagan [117]. Note that, we define the computer model as a function $\boldsymbol{y}^S = f(\cdot)$ that takes as input the control inputs $\boldsymbol{x}$ and the calibration parameters $\boldsymbol{\theta}$, and returns a q-dimensional response vector $\boldsymbol{y}^S \in \mathbb{R}^q$. The inputs $\boldsymbol{x}$ and parameters $\boldsymbol{\theta}$ lie in some multidimensional spaces $\mathcal{X} \subseteq \mathbb{R}^p$ and $\mathcal{T} \subseteq \mathbb{R}^t$, respectively. Thus, the computer model f is essentially a mapping $f : \mathcal{X} \times \mathcal{T} \mapsto \mathbb{R}^q$. Although f is a deterministic function (that is, if run multiple times at same input values, it will return the same value for responses), in order to approximate it with a surrogate model, we can regard f as an stochastic process [117].

We employ GP models that are known for their attractive mathematical and computational properties [54]. In the simple univariate case, a GP model is a non-parametric statistical model in which a stochastic process $f(\cdot)$ is assumed to have all of its finite-dimensional distributions as multivariate normal [118]. Therefore, the joint probability distribution of the outputs from the stochastic process at any finite set of inputs $\{\boldsymbol{x}_1, \ldots, \boldsymbol{x}_n\}$ (assuming f only takes $\boldsymbol{x}$ as inputs for now) is modeled as an n-dimensional multivariate normal distribution

$$p\left(f\left(\boldsymbol{x}_1\right), \ldots, f\left(\boldsymbol{x}_n\right) | \boldsymbol{\Phi}\right) \sim \mathcal{MVN}_n\left(\boldsymbol{m}, \boldsymbol{C}\right)$$

where the mean vector $\boldsymbol{m}$ is defined by a mean function $m(\cdot)$, and covariance matrix $\boldsymbol{C}$ is defined by a covariance function $c(\cdot, \cdot)$, with $\mathbb{E}\left[f\left(\boldsymbol{x}\right) | \boldsymbol{\Phi}\right] = m\left(\boldsymbol{x}\right)$ and $\operatorname{cov}\left[f\left(\boldsymbol{x}_i\right), f\left(\boldsymbol{x}_j\right) | \boldsymbol{\Phi}\right] = c\left(\boldsymbol{x}_i, \boldsymbol{x}_j\right)$. The whole distribution is fully defined by some set of hyperparameters $\boldsymbol{\Phi}$. Hence, we denote a univariate GP by

$$f(\cdot) \mid \boldsymbol{\Phi} \sim \mathrm{GP}\left(m(\cdot), c(\cdot, \cdot)\right)$$

Now, generalizing the univariate formulation to a multivariate case, the joint probability distri-

bution follows a *matrix-variate* normal distribution

$$p\left(f\left(\boldsymbol{x}_1\right), \ldots, f\left(\boldsymbol{x}_n\right) | \boldsymbol{\Phi}\right) \sim \mathcal{MVN}_{n,q}\left(\boldsymbol{m}, \boldsymbol{C}\right) \tag{3.1}$$

with *mean matrix* $\boldsymbol{m}$ and *cross-covariance matrix* $\boldsymbol{C}$, and fully defined by some set of hyperparameters $\boldsymbol{\Phi}$. The multivariate q-dimensional GP is denoted as

$$f\left(\cdot\right) \mid \boldsymbol{\Phi} \sim \mathcal{GP}_q\left(m\left(\cdot\right), c\left(\cdot, \cdot\right) \boldsymbol{\Sigma}\right) \tag{3.2}$$

where $c\left(\cdot, \cdot\right)$ is a positive definite correlation function accounting for correlation in the input space with $c\left(\boldsymbol{x}, \boldsymbol{x}\right) = 1$, and $\boldsymbol{\Sigma} \in \mathbb{R}_{+}^{q,q}$ is a positive definite matrix accounting for correlations between outputs. After this brief digression to set notation, we translate all these definitions into our original context, $\boldsymbol{y}^S = f\left(\boldsymbol{x}, \boldsymbol{\theta}\right)$. We build a multivariate GP-based on Equation (3.2), with the *i*-th input tuple denoted as $\left(\boldsymbol{x}, \boldsymbol{\theta}\right)_i = \left[x_{i,1}, \ldots, x_{i,p}, \theta_{i,1}, \ldots, \theta_{i,t}\right]^\top$. Mean and correlation functions are defined as follows:

$$m\left(\boldsymbol{x}, \boldsymbol{\theta}\right) = \boldsymbol{B}^\top h\left(\boldsymbol{x}, \boldsymbol{\theta}\right) \tag{3.3}$$

$$c\left(\left(\boldsymbol{x}, \boldsymbol{\theta}\right)_i, \left(\boldsymbol{x}, \boldsymbol{\theta}\right)_j\right) = \exp\left[-\left(\left(\boldsymbol{x}, \boldsymbol{\theta}\right)_i - \left(\boldsymbol{x}, \boldsymbol{\theta}\right)_j\right)^\top R\left(\left(\boldsymbol{x}, \boldsymbol{\theta}\right)_i - \left(\boldsymbol{x}, \boldsymbol{\theta}\right)_j\right)\right] \tag{3.4}$$

where $h : \mathcal{X} \times \mathcal{T} \rightarrow \mathbb{R}^m$ is a function (defined by the modeler) that maps the input space to *m* basis functions, $\boldsymbol{B} = \left[\boldsymbol{\beta}_1, \ldots, \boldsymbol{\beta}_q\right] \in \mathbb{R}^{m,q}$ is a matrix of regression coefficients, and $R = \operatorname{diag}\left(\boldsymbol{r}\right)$ is a diagonal matrix of positive roughness parameters with $\boldsymbol{r} = \left[r_1, \ldots, r_p, r_{p+1}, \ldots, r_{p+t}\right] \in \mathbb{R}_{+}^{p+t}$. The roughness parameter vector $\boldsymbol{r}$ explains how rough (or smooth) the function is, i.e. how quickly its values change across the input domain.

With the choices of linear regression mean function in Equation (3.3), stationary squared exponential correlation function in Equation (3.4), and separable covariance structure (with $\boldsymbol{\Sigma} \in \mathbb{R}_{+}^{q,q}$

accounting for correlations between outputs), the model is fully defined by

$$\boldsymbol{\Phi}_{\text{sim}} = \{\boldsymbol{B}, \boldsymbol{\Sigma}, \boldsymbol{r}\} \tag{3.5}$$

Under these settings, we run the computer model for several simulations to gather a set of data that will be used to train and build the surrogate model. There are different approaches to optimally select the points at which these simulations will be run to generate the training data set (given the computational burden of the computer model). However, we choose to employ the Latin Hypercube Sampling (LHS) method given its ability to explore the input space uniformly and homogeneously. The training data set consists of *N* points and is denoted by

$$\boldsymbol{X}^S = \begin{bmatrix} (\boldsymbol{x}, \boldsymbol{\theta})_1 \\ \vdots \\ (\boldsymbol{x}, \boldsymbol{\theta})_N \end{bmatrix} \in \mathbb{R}^{N,p+t} \quad \text{and} \quad \boldsymbol{Y}^S = \begin{bmatrix} \boldsymbol{y}^S(\boldsymbol{x}, \boldsymbol{\theta})_1 \\ \vdots \\ \boldsymbol{y}^S(\boldsymbol{x}, \boldsymbol{\theta})_N \end{bmatrix} \in \mathbb{R}^{N,q}$$

where $\boldsymbol{X}^S$ is an $N \times (p+t)$ input matrix and $\boldsymbol{Y}^S$ is an $N \times q$ output matrix. It can then be shown, as presented in Conti and O'Hagan [117], that the conditional posterior distribution of f given $\boldsymbol{r}$, after integrating out $\boldsymbol{B}$ and $\boldsymbol{\Sigma}$, is a multivariate q-dimensional T Process, such that the probability distribution it yields is a matrix-variate T distribution:

$$f(\cdot) \mid \boldsymbol{X}^S, \boldsymbol{Y}^S, \boldsymbol{r} \sim \mathcal{TP}_q\left(m^\star(\cdot), c^\star(\cdot,\cdot)\,\hat{\boldsymbol{\Sigma}}, N-m\right) \tag{3.6}$$

with $N - m$ degrees of freedom (denoted as *dof* henceforth), and

$$m^\star(\boldsymbol{x}, \boldsymbol{\theta}) = \hat{\boldsymbol{B}}^\top h(\boldsymbol{x}, \boldsymbol{\theta}) + \left(\boldsymbol{Y}^S - \boldsymbol{H}\hat{\boldsymbol{B}}\right)^\top \boldsymbol{A}^{-1}\boldsymbol{t}(\boldsymbol{x}, \boldsymbol{\theta}) \tag{3.7}$$

$$\begin{aligned} c^\star\left((\boldsymbol{x}, \boldsymbol{\theta})_i, (\boldsymbol{x}, \boldsymbol{\theta})_j\right) &= c\left((\boldsymbol{x}, \boldsymbol{\theta})_i, (\boldsymbol{x}, \boldsymbol{\theta})_j\right) - \boldsymbol{t}^\top(\boldsymbol{x}, \boldsymbol{\theta})_i \boldsymbol{A}^{-1}\boldsymbol{t}(\boldsymbol{x}, \boldsymbol{\theta})_j \\ &\quad + \left[h(\boldsymbol{x}, \boldsymbol{\theta})_i - \boldsymbol{H}^\top \boldsymbol{A}^{-1}\boldsymbol{t}(\boldsymbol{x}, \boldsymbol{\theta})_i\right]^\top \left(\boldsymbol{H}^\top \boldsymbol{A}^{-1}\boldsymbol{H}\right)^{-1} \left[h(\boldsymbol{x}, \boldsymbol{\theta})_j - \boldsymbol{H}^\top \boldsymbol{A}^{-1}\boldsymbol{t}(\boldsymbol{x}, \boldsymbol{\theta})_j\right] \end{aligned} \tag{3.8}$$

where

$$
\begin{aligned}
\boldsymbol{H}^{\top} &= \left[h\left(\boldsymbol{x},\boldsymbol{\theta}\right)_1,\ldots,h\left(\boldsymbol{x},\boldsymbol{\theta}\right)_N\right] \in \mathbb{R}^{m,N} \\
\boldsymbol{A} &= \left[c\left(\left(\boldsymbol{x},\boldsymbol{\theta}\right)_i,\left(\boldsymbol{x},\boldsymbol{\theta}\right)_j\right)\right]_{i,j=1:N} \in \mathbb{R}_{+}^{N,N} \\
\boldsymbol{t}^{\top}\left(\boldsymbol{x},\boldsymbol{\theta}\right)_i &= \left[c\left(\left(\boldsymbol{x},\boldsymbol{\theta}\right)_i,\left(\boldsymbol{x},\boldsymbol{\theta}\right)_1\right),\ldots,c\left(\left(\boldsymbol{x},\boldsymbol{\theta}\right)_i,\left(\boldsymbol{x},\boldsymbol{\theta}\right)_N\right)\right] \in \mathbb{R}^{N} \\
\hat{\boldsymbol{B}} &= \left(\boldsymbol{H}^{\top}\boldsymbol{A}^{-1}\boldsymbol{H}\right)^{-1}\boldsymbol{H}^{\top}\boldsymbol{A}^{-1}\boldsymbol{Y}^{S} \\
\hat{\boldsymbol{\Sigma}} &= \left(N-m\right)^{-1}\left(\boldsymbol{Y}^{S}-\boldsymbol{H}\hat{\boldsymbol{B}}\right)^{\top}\boldsymbol{A}^{-1}\left(\boldsymbol{Y}^{S}-\boldsymbol{H}\hat{\boldsymbol{B}}\right)
\end{aligned}
$$

To summarize, the T process defined in Equations (3.6)-(3.8) can be used as a fast surrogate model for the simulation model. Its mean function $m^{\star}$ interpolates the training data $\left(\boldsymbol{X}^{S},\boldsymbol{Y}^{S}\right)$ exactly and provides an approximation to $f\left(\cdot\right)$. For the surrogate model to be only dependent on the data, we need to integrate out the roughness parameters $\boldsymbol{r}$. This step is achieved through a Bayesian approach, for which the posterior distribution of the roughness parameters (again after proper integration of $\boldsymbol{B}$ and $\boldsymbol{\Sigma}$, see [117]) is given by:

$$
\pi\left(\boldsymbol{r}\middle|\boldsymbol{X}^{S},\boldsymbol{Y}^{S}\right) \propto \pi\left(\boldsymbol{r}\right)\left|\boldsymbol{A}\right|^{-\frac{q}{2}}\left|\boldsymbol{H}^{\top}\boldsymbol{A}^{-1}\boldsymbol{H}\right|^{-\frac{q}{2}}\left|\boldsymbol{Y}^{S^{\top}}\boldsymbol{G}\boldsymbol{Y}^{S}\right|^{-\frac{N-m}{2}}, \tag{3.9}
$$

with

$$
\boldsymbol{G} = \boldsymbol{A}^{-1} - \boldsymbol{A}^{-1}\boldsymbol{H}\left(\boldsymbol{H}^{\top}\boldsymbol{A}^{-1}\boldsymbol{H}\right)^{-1}\boldsymbol{H}^{\top}\boldsymbol{A}^{-1}.
$$

Subsequently, we set the prior distribution for $\boldsymbol{r}$ to follow a joint log-logistic distribution as below:

$$
\pi\left(\boldsymbol{r}\right) = \prod_{i=1}^{p+t}\left(1+r_i^2\right)^{-1}. \tag{3.10}
$$

We estimate posterior distributions of these roughness parameters using the *Metropolis Hastings* algorithm and select their mode as the values to be used in the surrogate model defined in Equations (3.6), (3.7) and (3.8). Once the roughness parameters $\boldsymbol{r}$ have been estimated, the sur-

rogate model in Equation (3.6) is fully defined. At this point, we assess its performance through *k-fold cross validation* (CV). CV is a common technique to evaluate the adequacy of predictive models, including surrogate models, through computing a metric that captures the deviation of the predictions obtained using the predictive model (the surrogate model in our case) and the true quantity being predicted (computer model predictions in our case). Put simply, our target to ensure that predictions obtained using the surrogate model are close to those obtained using the original computer model. In a CV procedure, we partition the training dataset $\left(\boldsymbol{X}^S, \boldsymbol{Y}^S\right)$ into *k* disjoint partitions. $k-1$ of these partitions are used to train the surrogate model, and then predictions are made on the left-out partition using Equation (3.7). These predictions are then compared with the computer model predictions. This process is iterated *k* times, such that at every iteration, a different partition is left out, and after all *k* iterations all partitions have been left out once and only once. Finally, the performance metric is computed. Many metrics have been reported in the literature on predictive modeling and machine learning. We utilize the well-known *mean absolute percentage error* (MAPE) defined as

$$\mathrm{MAPE}_j = \frac{1}{N}\sum_{i=1}^{N}\left|y_{i,j}^S - \hat{y}_{i,j}^S\right| \quad \forall j \in \{1,\ldots,q\}\,,$$

where $y_{i,j}^S$ is j-th element of the computer model output at input $(\boldsymbol{x},\boldsymbol{\theta})_i$, and $\hat{y}_{i,j}^S$ is the j-th element of the surrogate model prediction evaluated at the same input $(\boldsymbol{x},\boldsymbol{\theta})_i$ using the estimated values for $\boldsymbol{r}$.

If CV results are satisfactory (i.e. MAPE is low), then we can move to the next step of the calibration procedure in Section 3.1.2. Otherwise, we seek to improve the predictive power of the surrogate model. More specifically, we run an additional number of computer model simulations, such that we have a larger training data set that results in a better surrogate model. We achieve this through an *adaptive sampling* (AS) technique to select new data points to sample based on present results. The algorithm devised for this purpose is similar to a *grid search*, where we subdivide each dimension from the $(p+t)$-dimensional input spatial domain into grids (perhaps

with different number of divisions per dimension) yielding N_{AS} number of different data points within the grid,

$$\boldsymbol{X}^{\mathrm{grid}} = \begin{bmatrix} (\boldsymbol{x},\boldsymbol{\theta})_1^{\mathrm{grid}} \\ \vdots \\ (\boldsymbol{x},\boldsymbol{\theta})_{N_{\mathrm{AS}}}^{\mathrm{grid}} \end{bmatrix} \in \mathbb{R}^{N_{\mathrm{AS}},p+t}$$

and calculate the predictive variance for each point based on the probability distribution from Equation (3.6):

$$\mathrm{AS} = \left[\frac{1}{q} \sum_{j=1}^{q} c^{\star}\left((\boldsymbol{x},\boldsymbol{\theta})_i^{\mathrm{grid}}, (\boldsymbol{x},\boldsymbol{\theta})_i^{\mathrm{grid}} \right) \hat{\boldsymbol{\Sigma}}_{j,j} \right]_{i=1:N_{\mathrm{AS}}} \in \mathbb{R}_{+}^{N_{\mathrm{AS}}}$$

where $\hat{\boldsymbol{\Sigma}}_{j,j}$ is the *j*-th element in the diagonal of matrix $\hat{\boldsymbol{\Sigma}}$.

Elements of the vector AS represent the average predictive variance among all outputs at a specific input point. The vector is then sorted in descending order, and the corresponding points for the first 20 elements (with largest average predictive variance) are selected to be evaluated using the expensive computer model. The underlying hypothesis is that adding these points that showed high predictive variance to the training data set $\boldsymbol{X}^S$ will improve the predictive power of the surrogate model. We denote the set with these new appended data points by $\boldsymbol{X}^{\mathrm{AS}}$.

In implementing the adaptive sampling procedure as outlined above, we include two filters that ensure better sampling of new points. The first filter flags points that are very close to one other. This filter essentially avoids sampling more than one point from within a small sub-set of the input space, since this is not likely to provide more information. The filter takes the first 20 elements of the vector AS with largest predictive variance, and selects those that are at least some distance threshold τ_{AS} apart from one another. When a point is flagged and excluded, the next point from vector AS becomes a candidate to be added to $\boldsymbol{X}^{\mathrm{AS}}$ if it satisfies the filter criterion.

The second filter for the AS algorithm addresses the issue of extrapolation. It is well-known that GP predictive models have less predictive power at regions outside the domain of the training set $\boldsymbol{X}^S$. Hence, this filter excludes points within vector AS that are located outside of that domain.

It is important to point out that if the initial selection of design points in the data set $\boldsymbol{X}^S$ uniformly covers the input space (as is the case with Latin Hypercube Design), then this second filter will not be employed too often.

The AS algorithm can be iteratively conducted until a satisfactory value of the cross validation predictive error, MAPE, set by the user is achieved.

3.1.2 Multivariate Calibration Model

Once the surrogate model has been adequately constructed, it can now be used in lieu of the the original computer model in Equation (1.1) to generate sufficiently large number of simulations needed to conduct calibration of the parameters $\boldsymbol{\theta}$. Some of the steps in developing the following calibration procedure follow the work of Bhat et al. [119].

We start by elucidating the two remaining terms of the statistical model given in Equation (1.1). The term $\delta(\boldsymbol{x})$ is a discrepancy or model inadequacy function. This function accounts for factors that result in deviation between the computer model predictions and the real process being simulated, including missing physics, simplifying assumptions, and numerical errors. The term $\epsilon(\boldsymbol{x})$ models the measurement error associated with experimental observations. Note that both of these terms depend only on control inputs $\boldsymbol{x}$, since the calibration parameters are not changed or controlled in experiments.

Similar to what was done with the surrogate model in Section 3.1.1, we model $\delta(\cdot)$ as a multivariate q-dimensional GP,

$$\delta(\cdot) \mid \boldsymbol{r}_\delta, \boldsymbol{\sigma}_\delta \sim \mathcal{GP}_q\left(\mathbf{0}, c_\delta(\cdot,\cdot)\,\boldsymbol{\Sigma}_\delta\right) \tag{3.11}$$

with mean function that is equal to 0 for all elements, and a stationary squared exponential correlation function

$$c_\delta(\boldsymbol{x}_i, \boldsymbol{x}_j) = \exp\left[-(\boldsymbol{x}_i - \boldsymbol{x}_j)^\top R_\delta(\boldsymbol{x}_i - \boldsymbol{x}_j)\right]$$

where $R_\delta = \operatorname{diag}(\boldsymbol{r}_\delta)$ is a diagonal matrix of positive roughness parameters with $\boldsymbol{r}_\delta = \left[r_1^{(\delta)}, \ldots, r_p^{(\delta)}\right] \in \mathbb{R}_+^p$, and the covariance matrix of the model outputs $\boldsymbol{\Sigma}_\delta = \operatorname{diag}(\boldsymbol{\sigma}_\delta)$ is a diagonal matrix with positive variances $\boldsymbol{\sigma}_\delta = [\sigma_1, \ldots, \sigma_q] \in \mathbb{R}_+^q$.

The measurement error term $\epsilon(\cdot)$ is also modeled as a multivariate q-dimensional GP,

$$\epsilon(\cdot) \mid \boldsymbol{\psi} \sim \mathcal{GP}_q\left(\mathbf{0}, c_\epsilon(\cdot,\cdot)\,\boldsymbol{\Sigma}_\epsilon\right) \tag{3.12}$$

with mean function equal to 0 for all elements, and correlation function given by the Kronecker delta function

$$c_\epsilon(\boldsymbol{x}_i, \boldsymbol{x}_j) = \begin{cases} 1 & \text{if } \boldsymbol{x}_i = \boldsymbol{x}_j \\ 0 & \text{if } \boldsymbol{x}_i \neq \boldsymbol{x}_j \end{cases}$$

and noise matrix $\boldsymbol{\Sigma}_\epsilon = \operatorname{diag}(\boldsymbol{\psi})$ with positive noise variances $\boldsymbol{\psi} = [\psi_1, \ldots, \psi_q] \in \mathbb{R}^q_+$.

Notice that the model introduced in Equation (1.1) involves a summation of three random processes defined in Equations (3.6), (3.11) and (3.12). Here, we approximate the multivariate T process (the surrogate model) with a Gaussian Process, so that the summation in the RHS of Equation (1.1) becomes another Gaussian Process due to the property of addition of statistically independent Gaussian random variables [120]. This approximation can be justified using an analogous case in a univariate setting. Figure 3.1 shows several univariate T distributions with different dof, in addition to a standard Normal distribution. It can be seen that as the value of dof increases (values larger than 10), the T distributions approximate perfectly to the standard Normal distribution. Therefore, if a T distribution is defined with dof equal to $N - m$ with $N > m$ for some $N \in \mathbb{N}$ and $m \in \mathbb{N}$, then a T distribution with relative large $N - m$ dof can be approximated with a Normal distribution. This is the case specially in our setting where the size of the training dataset for surrogate model *N* is relative larger than the dimension *m* from the mean function linear regression.

With this approximation, the calibration model resulting from Equation (1.1) is a multivariate q-dimensional GP given by

$$\boldsymbol{y}^E(\cdot) \mid \boldsymbol{\Phi}_{\text{cal}} \sim \mathcal{GP}_q\left(m^\star(\cdot, \boldsymbol{\theta}), c^\star(\cdot,\cdot)\,\hat{\boldsymbol{\Sigma}} + c_\delta(\cdot,\cdot)\,\boldsymbol{\Sigma}_\delta + c_\epsilon(\cdot,\cdot)\,\boldsymbol{\Sigma}_\epsilon\right) \tag{3.13}$$

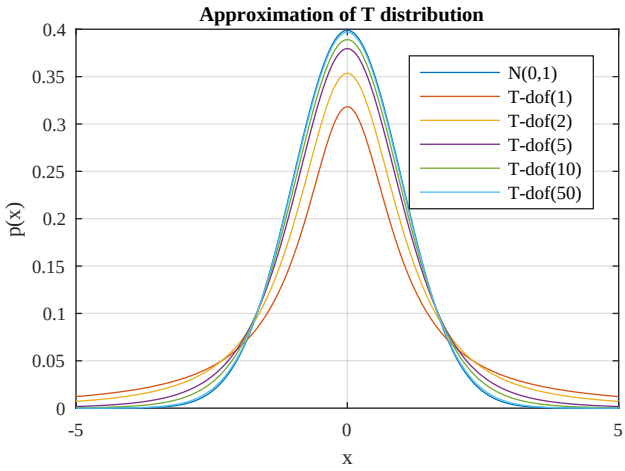

Figure 3.1: Approximation of T distributions to a normal distribution. Reprinted with permission. Copyright © 2018 by Springer-Verlag London Ltd.

where $\boldsymbol{\Phi}_{\text{cal}} = \{\boldsymbol{\theta}, \boldsymbol{r}_\delta, \boldsymbol{\sigma}_\delta, \boldsymbol{\psi}\}$ is the set of hyperparameters that will be estimated (including the calibration parameters $\boldsymbol{\theta}$).

In order to build the calibration model, we need another data set which is constructed from experimental observations. The procedure to obtain the experimental data is explained in Section 3.2. We denote this data set as

$$\boldsymbol{X}^E = \begin{bmatrix} \boldsymbol{x}_1^E \\ \vdots \\ \boldsymbol{x}_n^E \end{bmatrix} \in \mathbb{R}^{n,p} \quad \text{and} \quad \boldsymbol{Y}^E = \begin{bmatrix} \boldsymbol{y}^E\left(\boldsymbol{x}_1^E\right) \\ \vdots \\ \boldsymbol{y}^E\left(\boldsymbol{x}_n^E\right) \end{bmatrix} \in \mathbb{R}^{n,q}$$

where $\boldsymbol{X}^E$ is an $n \times p$ controllable input matrix and $\boldsymbol{y}^E(\boldsymbol{x})$ is the result of the experiment observed at $\boldsymbol{x}$, thus $\boldsymbol{Y}^E$ is a $n \times q$ matrix. It is worth to mention that the size *n* of this dataset may be different from simulation dataset size *N*, and that only control inputs $\boldsymbol{x}$ are used in the context of physical experiments (as opposed to $(\boldsymbol{x}, \boldsymbol{\theta})$ tuples for both the computer and surrogate models).

For implementation purposes, we rearrange the distribution resulting from Equation (3.13), by stacking each vector $\boldsymbol{y}^E\left(\boldsymbol{x}_i^E\right)$ and forming a single column vector with length $n \cdot q$, resulting in

the following distribution,

$$p\left(\boldsymbol{Y}^E \mid \boldsymbol{\Phi}_{\text{cal}}, \boldsymbol{X}^E, \boldsymbol{X}^S, \boldsymbol{Y}^S\right) \sim \mathcal{MVN}_{n\cdot q}\left(\boldsymbol{m}^\star, \boldsymbol{\Sigma}_{\text{cal}}\right) \tag{3.14}$$

with

$$\begin{aligned}
\boldsymbol{Y}^E &= \left[Y^E_{1,1}, \ldots, Y^E_{1,q}, \ldots, Y^E_{n,1}, \ldots, Y^E_{n,q}\right]^\top \in \mathbb{R}^{n\cdot q} \\
\boldsymbol{m}^\star &= \left[m^\star\left(\boldsymbol{x}^E_1, \boldsymbol{\theta}\right), \ldots, m^\star\left(\boldsymbol{x}^E_n, \boldsymbol{\theta}\right)\right]^\top \in \mathbb{R}^{n\cdot q} \\
\boldsymbol{\Sigma}_{\text{cal}} &= \boldsymbol{C}^{\text{cal}}_{\text{sur}} \otimes \hat{\boldsymbol{\Sigma}} + \boldsymbol{C}^{\text{cal}}_{\delta} \otimes \boldsymbol{\Sigma}_{\delta} + \boldsymbol{C}^{\text{cal}}_{\epsilon} \otimes \boldsymbol{\Sigma}_{\epsilon} \in \mathbb{R}^{n\cdot q, n\cdot q} \\
\boldsymbol{C}^{\text{cal}}_{\text{sur}} &= \left[c^\star\left(\left(\boldsymbol{x}^E_i, \boldsymbol{\theta}\right), \left(\boldsymbol{x}^E_j, \boldsymbol{\theta}\right)\right)\right]_{i,j=1:n} \in \mathbb{R}^{n,n} \\
\boldsymbol{C}^{\text{cal}}_{\delta} &= \left[c_\delta\left(\boldsymbol{x}^E_i, \boldsymbol{x}^E_j\right)\right]_{i,j=1:n} \in \mathbb{R}^{n,n} \\
\boldsymbol{C}^{\text{cal}}_{\epsilon} &= \left[c_\epsilon\left(\boldsymbol{x}^E_i, \boldsymbol{x}^E_j\right)\right]_{i,j=1:n} = \boldsymbol{I}_{n,n} \in \mathbb{R}^{n,n}
\end{aligned}$$

where $\otimes$ denotes the Kronecker matrix product employed to calculate cross-covariance matrix $\boldsymbol{\Sigma}_{\text{cal}}$ that accounts for the spatial dependence between inputs and outputs altogether.

The next step is to estimate the posterior distributions for the calibration parameters and hyperparameters. We conduct a Bayesian methodology to achieve this, where the posterior distributions of the hyperparameters $\boldsymbol{\Phi}_{\text{cal}}$ is given by

$$\boldsymbol{\theta}, \boldsymbol{r}_\delta, \boldsymbol{\sigma}_\delta, \boldsymbol{\psi} \mid \boldsymbol{X}^E, \boldsymbol{Y}^E, \boldsymbol{X}^S, \boldsymbol{Y}^S \propto p\left(\boldsymbol{Y}^E \mid \boldsymbol{\Phi}_{\text{cal}}, \boldsymbol{X}^E, \boldsymbol{X}^S, \boldsymbol{Y}^S\right) \pi\left(\boldsymbol{\theta}, \boldsymbol{r}_\delta, \boldsymbol{\sigma}_\delta, \boldsymbol{\psi}\right)$$

The distributions are computed using the Metropolis Hastings algorithm after adequate selection of the prior distributions $\pi\left(\boldsymbol{\theta}, \boldsymbol{r}_\delta, \boldsymbol{\sigma}_\delta, \boldsymbol{\psi}\right)$.

After determining these posterior distributions, the last remaining step is to construct a predictor that can be used to compute model predictions at input settings that have not been previously simulated or experimentally measured, and we rely on the *Kriging* technique, also known as the Best Linear Unbiased Estimator (BLUP) [32].

Let $\boldsymbol{X}^{\text{pred}}$ denote a set of s control inputs $\boldsymbol{x}^{\text{pred}}_i$, that have not been previously simulated or

experimentally measured

$$\boldsymbol{X}^{\text{pred}} = \begin{bmatrix} \boldsymbol{x}_1^{\text{pred}} \\ \vdots \\ \boldsymbol{x}_s^{\text{pred}} \end{bmatrix} \in \mathbb{R}^{s,p}$$

Then the predictive distribution of model outputs, $p\left(\boldsymbol{Y}_{\text{pred}}^{E} \middle| \boldsymbol{X}^{\text{pred}}, \boldsymbol{X}^{E}, \boldsymbol{Y}^{E}, \boldsymbol{X}^{S}, \boldsymbol{Y}^{S}, \boldsymbol{\Phi}_{\text{cal}}, \boldsymbol{\Phi}_{\text{sim}}\right)$, is an s-dimensional multivariate normal distribution with the following parameters:

- Expected value is given by:

$$\mathbb{E}\left[\boldsymbol{Y}_{\text{pred}}^{E} \middle| \boldsymbol{X}^{\text{pred}}, \boldsymbol{X}^{E}, \boldsymbol{Y}^{E}, \boldsymbol{X}^{S}, \boldsymbol{Y}^{S}, \boldsymbol{\Phi}_{\text{cal}}, \boldsymbol{\Phi}_{\text{sim}}\right] = \boldsymbol{m}_{\text{pred}}^{\star} + \boldsymbol{\Sigma}_0 \boldsymbol{\Sigma}_{\text{cal}}^{-1}\left(\boldsymbol{Y}^{E} - \boldsymbol{m}^{\star}\right) \quad (3.15)$$

  where

$$\begin{aligned}
\boldsymbol{m}_{\text{pred}}^{\star} &= \left[m^{\star}\left(\boldsymbol{x}_1^{\text{pred}}, \boldsymbol{\theta}\right), \ldots, m^{\star}\left(\boldsymbol{x}_s^{\text{pred}}, \boldsymbol{\theta}\right)\right]^{\top} \in \mathbb{R}^{s \cdot q} \\
\boldsymbol{\Sigma}_0 &= \boldsymbol{C}_{\text{sur}}^{\text{pred,cal}} \otimes \hat{\boldsymbol{\Sigma}} + \boldsymbol{C}_{\delta}^{\text{pred,cal}} \otimes \boldsymbol{\Sigma}_{\delta} \in \mathbb{R}^{s \cdot q, n \cdot q} \\
\boldsymbol{C}_{\text{sur}}^{\text{pred,cal}} &= \left[c^{\star}\left(\left(\boldsymbol{x}_i^{\text{pred}}, \boldsymbol{\theta}\right), \left(\boldsymbol{x}_j^{E}, \boldsymbol{\theta}\right)\right)\right]_{i=1:s, j=1:n} \in \mathbb{R}^{s,n} \\
\boldsymbol{C}_{\delta}^{\text{pred,cal}} &= \left[c_{\delta}\left(\boldsymbol{x}_i^{\text{pred}}, \boldsymbol{x}_j^{E}\right)\right]_{i=1:s, j=1:n} \in \mathbb{R}^{s,n}
\end{aligned}$$

- Variance is given by

$$\text{Var}\left[\boldsymbol{Y}_{\text{pred}}^{E} \middle| \boldsymbol{X}^{\text{pred}}, \boldsymbol{X}^{E}, \boldsymbol{Y}^{E}, \boldsymbol{X}^{S}, \boldsymbol{Y}^{S}, \boldsymbol{\Phi}_{\text{cal}}, \boldsymbol{\Phi}_{\text{sim}}\right] = \boldsymbol{\Sigma}_{\text{pred}} - \boldsymbol{\Sigma}_0 \boldsymbol{\Sigma}_{\text{cal}}^{-1} \boldsymbol{\Sigma}_0^{\top}, \quad (3.16)$$

where

$$\boldsymbol{\Sigma}_{\text{pred}} = \boldsymbol{C}_{\text{sur}}^{\text{pred}} \otimes \hat{\boldsymbol{\Sigma}} + \boldsymbol{C}_{\delta}^{\text{pred}} \otimes \boldsymbol{\Sigma}_{\delta} + \boldsymbol{C}_{\epsilon}^{\text{pred}} \otimes \boldsymbol{\Sigma}_{\epsilon} \in \mathbb{R}^{s \cdot q, s \cdot q}$$

$$\boldsymbol{C}_{\text{sur}}^{\text{pred}} = \left[c^{\star} \left(\left(\boldsymbol{x}_i^{\text{pred}}, \boldsymbol{\theta} \right), \left(\boldsymbol{x}_j^{\text{pred}}, \boldsymbol{\theta} \right) \right) \right]_{i,j=1:s} \in \mathbb{R}^{s,s}$$

$$\boldsymbol{C}_{\delta}^{\text{pred}} = \left[c_{\delta} \left(\boldsymbol{x}_i^{\text{pred}}, \boldsymbol{x}_j^{\text{pred}} \right) \right]_{i,j=1:s} \in \mathbb{R}^{s,s}$$

$$\boldsymbol{C}_{\epsilon}^{\text{pred}} = \left[c_{\epsilon} \left(\boldsymbol{x}_i^{\text{pred}}, \boldsymbol{x}_j^{\text{pred}} \right) \right]_{i,j=1:s} \in \mathbb{R}^{s,s}$$

To assess the performance of the calibrated model, a cross validation (CV) procedure similar to the one described for the surrogate model in Section 3.1.1 can be used. The mean absolute percentage error (MAPE) can be computed using Equations (3.15) and (3.16). The key difference is the fact that in this case, simulations from the calibrated surrogate model are compared with experimental measurements, in contrast to comparing surrogate model predictions with the computer model predictions.

3.2 Experimental setup

As mentioned in Section **??**, experimental data is needed to calibrate the computer model. LHS design was also used to uniformly explore the control input space $\mathcal{X}$. A total of $n = 24$ different configurations of $\boldsymbol{x}$ were determined, which constitute $\boldsymbol{X}^E$. Next, the fabrication and characterization were conducted to obtain the corresponding outputs $\boldsymbol{Y}^E$.

3.2.1 Melt pool depth and width

Single tracks of length $20\,\text{mm}$ were fabricated on a $30\,\mu\text{m}$ powder-bed using a ProX 100 DMP commercial L-PBF system by 3D Systems. The system is equipped with a Gaussian profile fiber laser beam with wavelength $\lambda = 1070\,\text{nm}$ and beam spot size of approximately $70\,\mu\text{m}$-diameter. Argon was used as inert protective atmosphere during fabrication. The raw Ti-6Al-4V powder was produced by LPW Technology. Single tracks were built on a Ti-6Al-4V substrate, which was subsequently cut with a Buehler precision saw and mounted for cross-section analysis. Metallographic grinding was performed with silicon carbide papers (320 to 600 grit size) followed by

manual polishing with $1\ \mu\mathrm{m}$ diamond suspension and final precision polishing with colloidal silica suspension. To make melt pool boundary lines more visible, chemical etching was performed using a 3:1 volume mixture of HCl and HNO_3 solution. Melt pool depth and width were measured using optical microscopy (Nikon Optiphot - POL) and verified with scanning electron microscopy (FEG-SEM/FIB TESCAN LYRA3). Representative SEM images that were used for measuring the melt pool depth and width are shown in Figure 3.2. We visually ascertain from the figure that both higher laser powers and lower scan speed increase the melt pool size; however, the impact of laser speed on the melt pool dimensions is higher, primarily due to the low maximum power on the system (50 W).

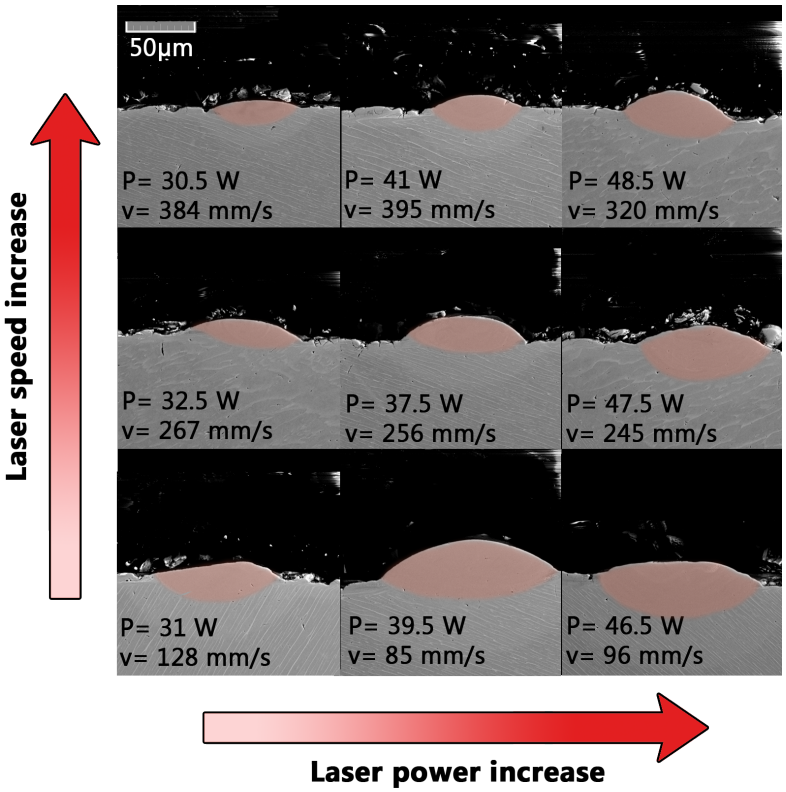

Figure 3.2: Representative SEM images used for measuring the melt pool depth and width. Reprinted with permission. Copyright © 2018 by Springer-Verlag London Ltd.

3.2.2 Melt pool peak temperature

The L-PBF system was custom integrated with a thermal imaging sensor to conduct in-situ monitoring of melt pool temperature during fabrication. The sensor is a two-wavelength imaging pyrometer (ThermaVIZ® by Stratonics Inc.) that consists of two high resolution CMOS imaging detectors. Both detectors have a field of view (FOV) with 1300×1000 pixel resolution mapped to a 30×27 mm area, which yields a resolution of $24\,\mu\mathrm{m}$ per pixel. Figure 3.3 shows the pyrometer integrated inside the ProX100 DMP build chamber. Experimental Calibration of the pyrometer (which is to be distinguished from statistical calibration of the model) was performed in-situ after integration using a tungsten filament (halogen tungsten-lamp) for a range of temperatures between $1500 - 2500\,^{\circ}\mathrm{C}$. By fabricating the single tracks within the FOV of the pyrometer, thermal images of the melt pools were taken at approximately $250\,\mathrm{Hz}$. These images were used to compute the melt pool peak temperature.

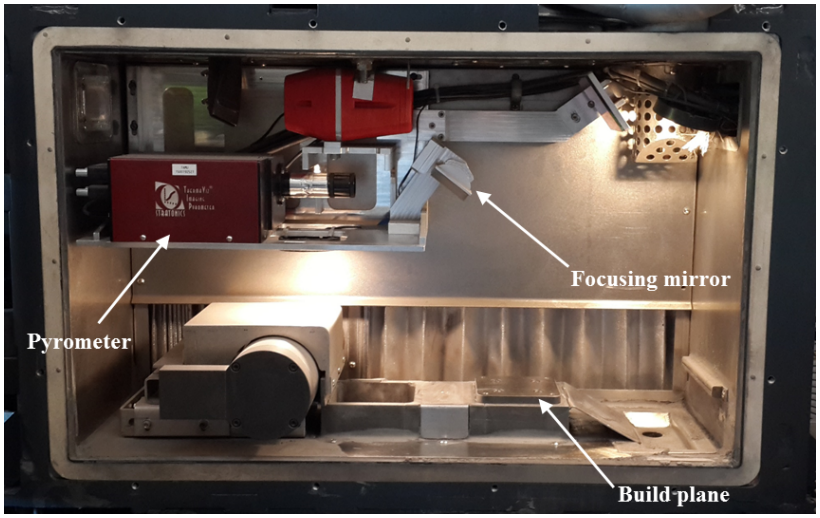

Figure 3.3: The two-wavelength pyrometer used for temperature measurement mounted inside the L-PBF machine. Reprinted with permission. Copyright © 2018 by Springer-Verlag London Ltd.

A sample melt pool temperature map taken from a representative thermal image is shown Figure 3.4 where X and Y coordinates are pixels resolved by the pyrometer and the color scale

represents temperature. The temperature map shows zero for temperature values below $1500\,^{\circ}\mathrm{C}$ that fall outside the calibration range of the pyrometer.

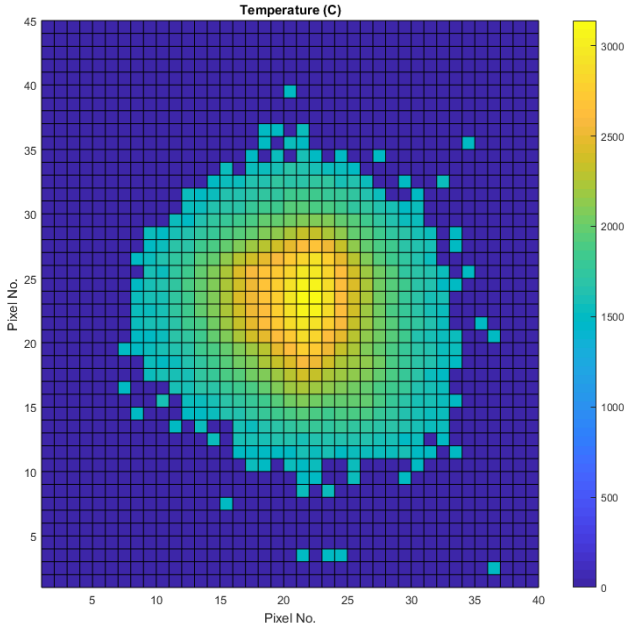

Figure 3.4: Temperature map of a sample melt pool captured using the pyrometer. Reprinted with permission. Copyright © 2018 by Springer-Verlag London Ltd.

3.3 Multivariate calibration of Ti-6Al-4V single tracks

In this section we link thermal models to experiments via a computationally efficient surrogate modeling approach based on multivariate Gaussian processes (MVGPs). The MVGPs are then used to calibrate the free parameters of the multi-physics models against experiments, sidestepping the use of prohibitively expensive Monte Carlo-based calibration. This framework thus makes it possible to efficiently evaluate the impact of varying process parameter inputs on the characteristics of the melt pool during AM. We demonstrate the framework on the calibration of a thermal model for Laser-Powder Bed Fusion AM of Ti-6Al-4V against experiments carried out over a wide window in the process parameter space. While this work deals with problems related to AM, its applicability is wider as the proposed framework could potentially be used in many other ICME-

based problems where it is essential to link expensive computational materials science models to available experimental data.

3.3.1 Melt pool Modeling through FEM based thermal modeling

Formally, we define the melt pool as the region in the laser-powder interface at which metal powder particles fuse to form a pool of molten metal that eventually solidifies after the laser beam moves to another location. In this paper, we developed a three-dimensional FEM based thermal model implemented in COMSOL Multiphysics software to study melt pool characteristics, including geometry and thermal profiles, during the fabrication of single tracks printed in a thin layer of powder on top of a solid substrate. The powder layer was assumed as a $30\,\mu\mathrm{m}$ continuum medium over a $1\,\mathrm{mm}$ thick substrate. Ti-6Al-4V alloy was selected as the material for both the powder layer and the substrate. To ensure accurate analysis, a fine mesh element was used for the laser-powder interaction zones, while a coarser element was employed for the rest of the simulation domain. Second-order quadrilateral Lagrange elements were used for the entire domain, while the $30\,\mu\mathrm{m}$ fine elements were found suitable for the powder-bed based on the mesh convergence analysis. Single track simulations were run for a $3\,\mathrm{mm}$-long track. Figure 3.5 shows a sample output of the model with melt pool temperature profiles [1].

An appreciable number of FEM based thermal models have been developed to predict the thermal history and melt pool geometry during L-PBF. In these works, the effects of process parameters (e.g., laser power, scanning velocity, hatch spacing), material properties, and powder properties (e.g., particle size distribution, layer thickness) have been investigated. For these melt pool models, an appropriate powder-bed model should be employed. Modeling of the powder-bed has been done in two different ways: powder-scale (refer to [33, 121, 122, 99, 123, 124, 125, 126]) and continuum-scale (refer to [127, 128, 96, 129, 130, 131, 97, 132]). Although the first approach enables simulating the size variations and the local changes in the melt pool such as incomplete melting or formation of pores [33, 121], it is computationally expensive such that it is almost impossible to use it for full-part simulation. The latter approach, on the other hand, has been widely employed due to its relatively low computational cost and ease of implementation. While some

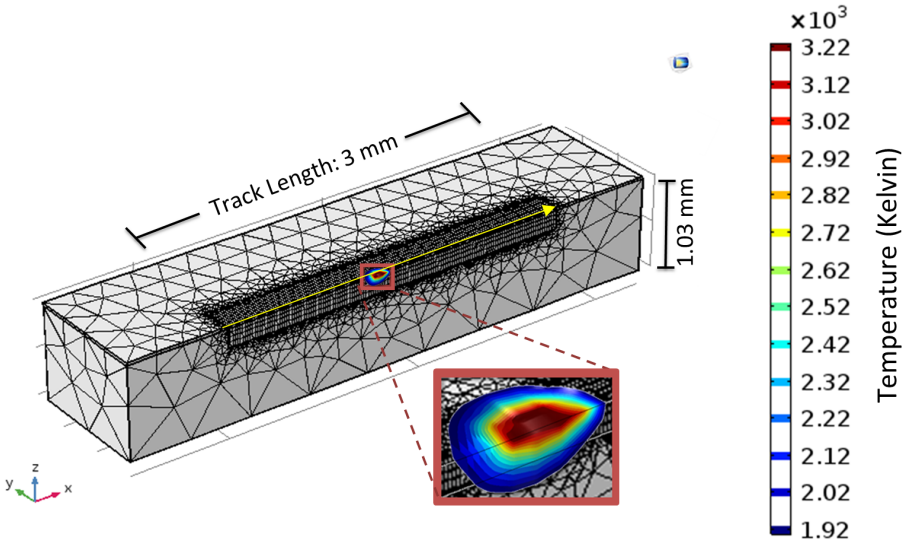

Figure 3.5: Sample output of the melt pool model for Ti-6Al-4V powder on a Ti-6Al-4V substrate, showing the melt pool temperature profiles in three-dimensions. Reprinted with permission. Copyright © 2018 by Springer-Verlag London Ltd. [1]

studies have taken fluid dynamics effects in the melt pool into account (e.g., Marangoni convection in [124, 133, 134]), a significant number of works in the literature have neglected those effects to simplify the model (see for example [96, 129, 130, 132]). The change in volume during melting of the powder [97, 135, 136] and layer built-up were modeled in some studies [128, 131, 137, 138]. We refer the interested readers to review papers on numerical modeling and simulation of AM for more information [139, 140, 141].

The model used in this work accounts for several heat transfer mechanisms that take place during metal L-PBF. In particular, conduction, convection, radiation, phase transitions (namely, solid-to-liquid and liquid-to-gas transitions), latent heat of melting/evaporation, temperature dependent material properties, and the effective thermo-physical properties for the powder layer were considered. Furthermore, heat loss due to evaporation was incorporated by employing a simple approach based on the implementation of a heat sink on the powder surface. The laser beam was defined as a two-dimensional Gaussian distributed moving heat source. The initial temperature of the build was set to the ambient temperature (298 K). Natural convection, radiation and evaporation were

employed as boundary conditions on the powder surface, while a symmetry boundary condition was applied along the scanning path to reduce the computational cost. All other boundaries were maintained at the ambient temperature.

Since the thermal model takes different physical mechanisms into account, there are multiple materials parameters that influence the model results, and thus, the predictive capabilities of the model. After preliminary simulation experiments, the following parameters were identified as most significant on variability in model outputs: (1) laser absorptivity, (2) powder-bed porosity, and (3) thermal conductivity of the liquid. It is known that the laser absorptivity is a function of temperature and has different values for powder, solid and liquid materials. There are several factors (e.g., beam intensity, wavelength, temperature, oxidation, powder size and distribution) affecting the absorptivity of the material. Therefore, it is difficult to experimentally measure it. Note that while low values of absorptivity result in insufficient energy input and incomplete melting of the powder particles, very high values lead to overheating of the particles, hence, over estimation of the melt pool size.

Moreover, to account for the effect of Marangoni convection on the melt pool size and geometry, the thermal conductivity of liquid was increased according to [142, 143, 129]. However, there is no consensus in the community on the level of this increase. Powder porosity is used as an input to predict the effective thermo-physical properties (thermal conductivity, density, heat capacity) of the powder layer. Therefore, it has a significant influence on the predicted thermal distribution. Considering the aforementioned aspects, a need for the calibration of these three parameters was realized.

The statistical calibration procedure is conducted on the FEM based thermal model described in Section 3.3.1. Following our definitions, the thermal model represents the *computer model*, and the two terms will be used interchangeably in the remainder of the text. This computer model predicts the three-dimensional thermal profiles of the moving melt pool during L-PBF AM. It is reported in the literature that the melt pool temperature and geometry (depth and width) are important factors influencing the outcome of the L-PBF process [59]. The inputs and outputs of the computer model

are described as follows:

- Two control inputs
  - x_1: laser power (W)
  - x_2: laser scan speed ($\mathrm{mm/s}$)
- Three calibration parameters
  - θ_1: powder-bed porosity ($\%$)
  - θ_2: laser absorptivity($\%$)
  - θ_3: coefficient of thermal conductivity for liquid ($\frac{\mathrm{W}}{\mathrm{m \cdot K}}$)
- Three model outputs (or quantities of interest, QoIs)
  - y_1^S, y_1^E : melt pool depth into the solid substrate ($\mu\mathrm{m}$)
  - y_2^S, y_2^E: melt pool width ($\mu\mathrm{m}$)
  - y_3^S, y_3^E: melt pool peak temperature ($^\circ\mathrm{C}$).

The chosen control inputs (laser power and speed) are known to have the most significant effect on the melt pool characteristics, and are commonly studied by AM researchers, see for example [32]. In terms of the notation defined in Section **??**, we have the length of the control inputs vector $p = 2$, and lengths of the calibration parameters vector and computer model outputs vector $t = q = 3$. We test the performance of the proposed multivariate calibration procedure through studying the melt pool conditions while fabricating single track of Ti-6Al-4V. We derive the posterior distributions of the calibration parameters $\boldsymbol{\theta}$ using a synthesis of computer model simulations denoted by matrices $\boldsymbol{X}^S$ and $\boldsymbol{Y}^S$, and experimental observations denoted by matrices $\boldsymbol{X}^E$ and $\boldsymbol{Y}^E$. We start by constructing a GP-based surrogate model using a data set of computer model simulations (Section 3.3.2). Next, we conduct manufacturing and characterization experiments to collect the data required for calibrating the model (Section 3.2). Finally, we conduct model calibration and prediction (see Section 3.3.3).

3.3.2 Building the surrogate model

Since L-PBF processes involve complicated physical phenomena with different forms of heat and mass transfer and material phase transitions, the run-times for computer simulation models are typically long. This necessitates the use of computationally efficient surrogate models, both for the purpose of conducting calibration or for process planning and optimization. In the present case, the execution time for the FEM based thermal model developed was dependent on the model inputs (control inputs and calibration parameters). From initial test simulation runs, execution times ranged between 30 minutes to 5 hours. Hence, performing a traditional Markov chain Monte Carlo (MCMC) with 50,000 iterations would take approximately 800 weeks. Furthermore, MCMC sampling strategies preclude the use of embarrassingly parallel modes of execution to improve computational time. Instead, we use the two-stage surrogate-modeling approach explained in Section 3.1.1 to address this challenge.

To build the surrogate model, a training data set from the original FEM based thermal model is first needed. This data set consists of the two matrices $\boldsymbol{X}^S$ and $\boldsymbol{Y}^S$ introduced earlier, representing simulation inputs and outputs, respectively. We use the Latin Hypercube sampling (LHS) strategy to uniformly select design points from the control input and calibration parameters space, $\mathcal{X} \times \mathcal{T}$. The lower and upper bounds for the control input space $\mathcal{X}$ was chosen as $\mathcal{X}_{min} = \{30\,\mathrm{W}, 80\,\mathrm{mm/s}\}$, and $\mathcal{X}_{max} = \{500\,\mathrm{W}, 400\,\mathrm{mm/s}\}$. These bounds were determined based on prior knowledge of the commercial metal L-PBF system used in this study and machine specifications. The lower and upper bounds for the calibration parameter space were chosen as $\mathcal{T}_{min} = \{20\%, 40\%, 1\}$, and $\mathcal{T}_{max} = \{70\%, 90\%, 25\}$. These bounds were specified by the AM researchers based on previous values reported in the literature to construct an initial region within which the true values of $\boldsymbol{\theta}$ are believed to lie. A simulation data set of size $N = 130$ was generated over the $\mathcal{X} \times \mathcal{T}$ space. Hence, $\boldsymbol{X}^S$ is an $N \times (p + t)$ matrix with 130 different and uniformly selected $(\boldsymbol{x}, \boldsymbol{\theta})$ combinations, and $\boldsymbol{Y}^S$ is an $N \times q$ with elements representing outputs of the thermal model for input $\boldsymbol{X}^S$. Code parallelization was conducted on a 843-node high-performance supercomputer.

Recall from Equation 3.6 that the conditional posterior distribution of $\boldsymbol{f}(\cdot)$ given the simulation training data $(\boldsymbol{X}^S, \boldsymbol{Y}^S)$ and roughness parameters $\boldsymbol{r}$ is a q-variate T Process. The Bayesian approach was then used to estimate the roughness parameters. To ensure their positivity, log-logistic prior distributions for the elements of $\boldsymbol{r}$ with both scale and shape parameters equal to 1 were used (see Equation 3.10). Next, using the single-component Metropolis-Hastings algorithm, the posterior distributions of $\boldsymbol{r}$ were generated after 50,000 iterations with 25% burn-in period and thinning every fifth sample. Figure 3.6 shows the histograms and kernel density estimates of the posterior distributions for the roughness parameters. The posteriors are very informative, and hence the modes were used as the estimates for the roughness parameters $\boldsymbol{r}$. At this stage, the surrogate model is built and ready to use, since essentially when the roughness parameters have been estimated, the output of the computer model at any given combination of $(\boldsymbol{x}, \boldsymbol{\theta})$ can be estimated using Equation 3.7. A confidence interval for this estimate can also be determined using Equation 3.8.

It is necessary to validate and assess the performance of the surrogate model once the hyperparameters $\boldsymbol{\Phi}_{\text{sim}}$ are estimated. A 10-fold cross validation was performed for the surrogate model and the results are displayed in Figures 3.7a, 3.7b, and 3.7c, corresponding to the the three model outputs: melt pool depth, width, and peak temperature, respectively. In the plots, the horizontal axes represent the outputs of the computer simulation model, while the vertical axes show the predicted outputs using the surrogate model with the bars representing confidence intervals for these predictions. In other words, the red line represents the ideal case with surrogate model predictions $\mathbb{E}[f(\boldsymbol{x})|\boldsymbol{X}^S, \boldsymbol{Y}^S, \boldsymbol{\theta}]$ being in full agreement with computer model simulations $y^S(\boldsymbol{x}, \boldsymbol{\theta})$.

It can be visually seen that the predictive performance of the surrogate model is satisfactory. For a quantitative assessment, the computed MAPE values for the three outputs are reported in Table 3.1, also indicating satisfactory performance. Note that since the predictive accuracy, represented by MAPE, was deemed acceptable, there was no need for further sampling using the adaptive sampling technique described in Section 3.1.1.

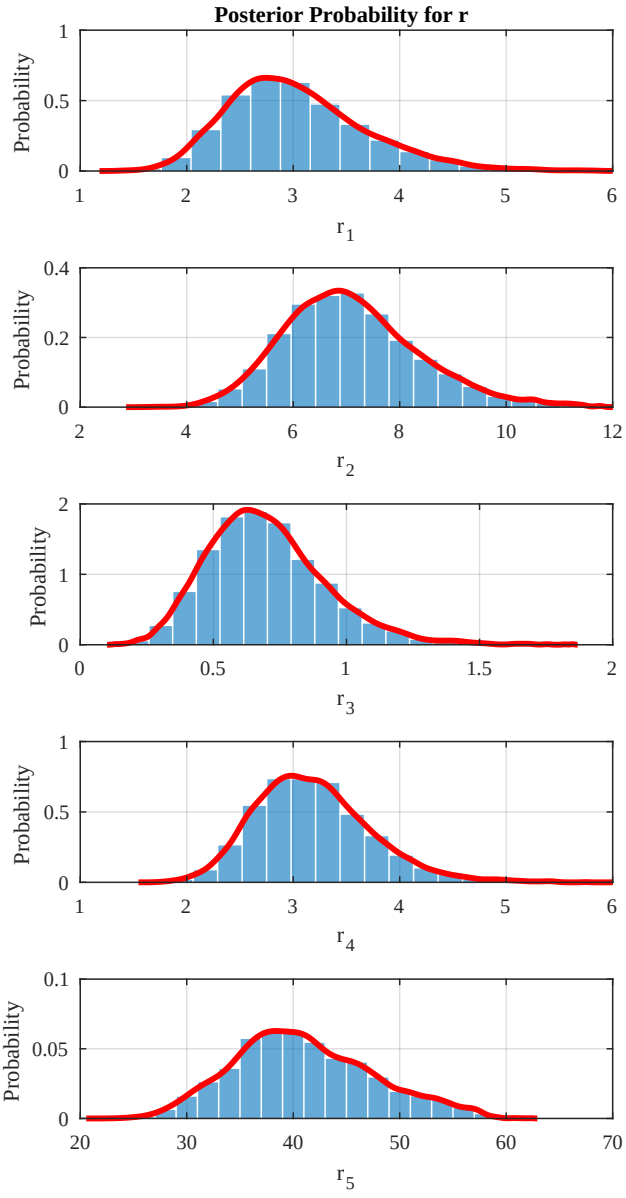

Figure 3.6: Histograms and kernel density estimates of the posterior distributions for the roughness parameters $\boldsymbol{r}$ for the surrogate model. Reprinted with permission. Copyright © 2018 by Springer-Verlag London Ltd.

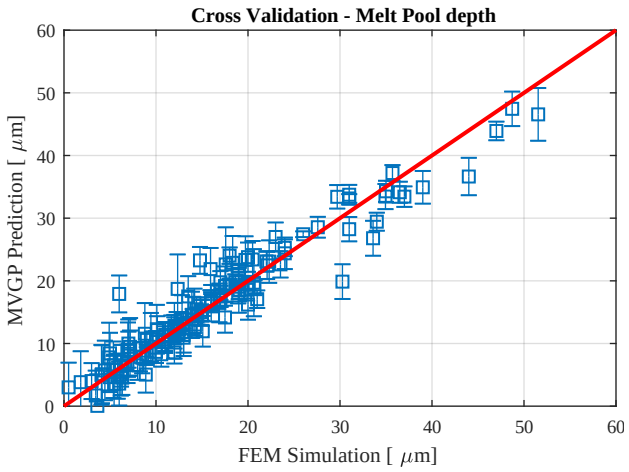

(a)

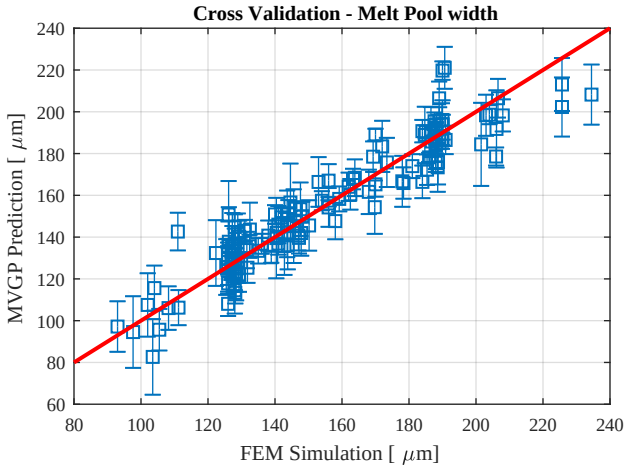

(b)

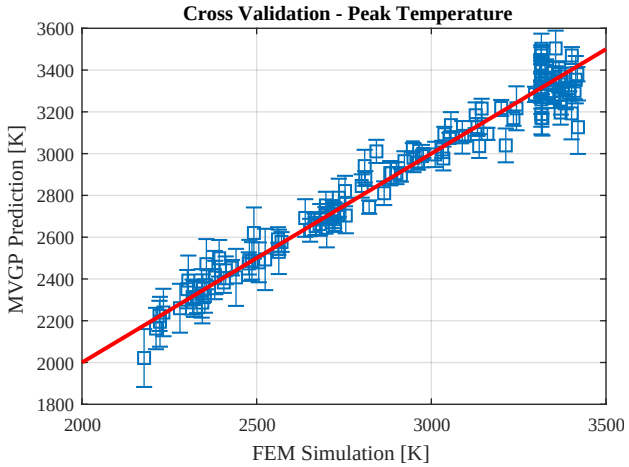

(c)

Figure 3.7: Results of a 10-fold cross validation of the surrogate model for (a) melt pool depth, (b) melt pool width, and (c) melt pool peak temperature. Reprinted with permission. Copyright © 2018 by Springer-Verlag London Ltd.

Table 3.1: Mean absolute predictive error (MAPE) of the surrogate model for the three outputs. Reused with permission. Copyright © 2018 by Springer-Verlag London Ltd.

Melt pool property	Depth	Width	Peak Temperature
Observed range in simulation	$51.3\,\mu\text{m}$	$147.8\,\mu\text{m}$	$1284\,\text{K}$
Mean absolute predictive error (MAPE)	$2.01\,\mu\text{m}$	$8.05\,\mu\text{m}$	$56.5\,\text{K}$
MAPE as % of the simulation range	4%	5%	4%

3.3.3 Performance of the calibration

With the surrogate model fully defined and the experimental measurements conducted, we are now able to estimate the calibration parameters $\boldsymbol{\theta}$, as well as the remaining hyperparameters $\boldsymbol{\Phi}_{\text{cal}}$ required for the statistical model ($\boldsymbol{r}_\delta, \boldsymbol{\sigma}_\delta$, and $\boldsymbol{\psi}$, introduced in Equations 1.1, 3.11, and 3.12). As instructed in Section 3.1.2, we use the Bayesian framework and Metropolis-Hastings MCMC to estimate the set of hyperparameters $\boldsymbol{\Phi}_{\text{cal}} = \{\boldsymbol{\theta}, \boldsymbol{r}_\delta, \boldsymbol{\sigma}_\delta, \boldsymbol{\psi}\}$. The following prior distributions are selected for the hyperparameters:

$$\theta_i \sim \text{Uniform}(\alpha_i^\theta, \beta_i^\theta)$$

$$r_{\delta_i} \sim \text{Log-Logistic}(\alpha = 1, \beta = 1)$$

$$\sigma_i \sim \text{Inverse-Gamma}(\alpha = 2, \beta = 1)$$

$$\psi_i \sim \text{Inverse-Gamma}(\alpha = 2, \beta = 1)$$

Note that the priors for the calibration parameters θ_i are all uniform and hence non-informative to avoid bias in estimation, and since no information beyond the suggested lower and upper bounds were available. Examples of constructing informative prior distributions using additional prior knowledge can be found in [144, 145]. The lower and upper bounds for these prior distributions, $(\alpha_i^\theta, \beta_i^\theta)$, were set equal to the lower and upper bounds of the parameters space $\mathcal{T}_{min} = \{20\%, 40\%, 1\}$, and $\mathcal{T}_{max} = \{70\%, 90\%, 25\}$. For the roughness parameters r_{δ_i}, log-logistic priors were used as recommended by [117]. For the variance parameters σ_i and ψ_i, inverse gamma priors

Table 3.2: Posterior distribution parameters for the calibration parameters. Reused with permission. Copyright © 2018 by Springer-Verlag London Ltd.

Parameter	Posterior mean	Posterior mode	Posterior std. dev.
Powder porosity, θ_1	0.423	0.400	0.112
Laser absorptivity, θ_2	0.782	0.782	0.066
Coefficient of thermal conductivity for liquid, θ_3	6.727	6.709	0.922

are selected because they represent conjugate priors for the multivariate normal likelihood function in our model.

Similar to Section 3.3.2, single-component Metropolis-Hastings procedure was used to compute the posterior distributions for the hyperparameters. Figure 3.8 shows the histograms and kernel density estimates for these parameters after 100,000 MCMC iterations with 25% burn-in period and thinning every fifth sample. In the plots, we observe unimodal and well-informative posteriors for all of the calibration parameters with θ_1 and θ_3 showing symmetric density functions and θ_2 showing a density function skewed to the right. Table 3.2 reports the posterior mean, mode, and standard deviation for the posterior distributions of the calibration parameters.

Porosity, θ_1, is used to calculate the effective thermo-physical properties of the powder-bed (i.e., thermal conductivity and density). It was observed during simulations that by changing the porosity from 0.3 to 0.5 the thermal conductivity of the powder changes up to $2\ \frac{\mathrm{W}}{\mathrm{m \cdot K}}$, which leads to an insignificant change in the thermal history and only a few microns change in the melt pool size. Thus, by considering the variability in experimental measurements for melt pool dimensions, this change becomes negligible, and the wide nature of the posterior distribution for θ_1 is physically consistent. Furthermore, a posterior mean of 0.423 is reasonable since it agrees with the reported range of porosity for similar powder sizes and layer thicknesses, see [146, 143].

The posterior distribution of absorptivity (θ_2) shows a more informative posterior distribution with mean of 0.782. This value demonstrates reasonable agreement with reported experimental results in the literature [147, 148]. However, considering the difficulties associated with experi-

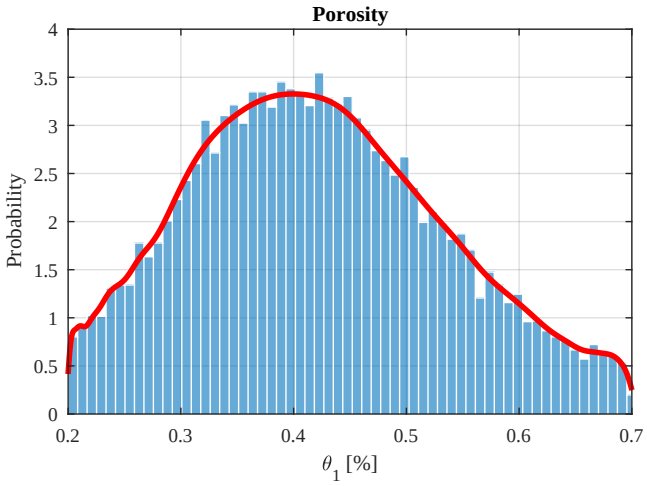

(a)

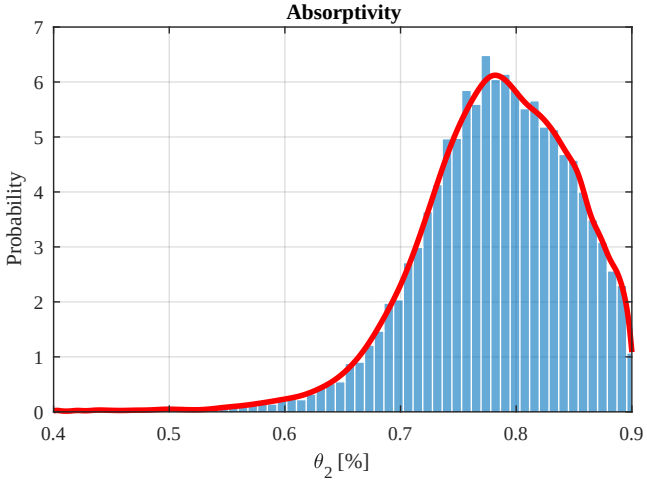

(b)

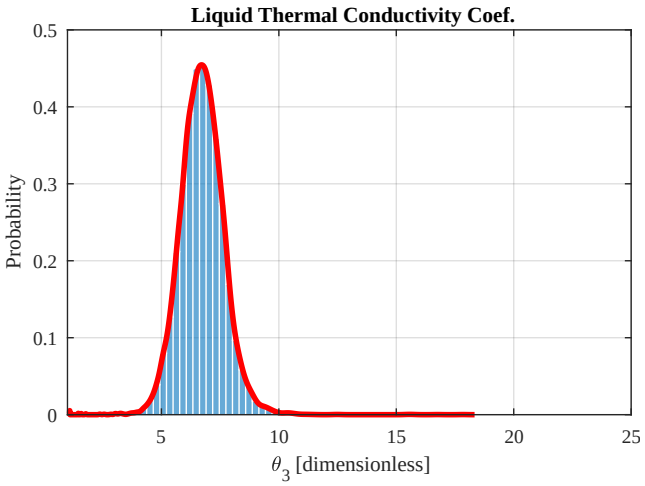

(c)

Figure 3.8: Histograms and kernel density estimates of the posterior distributions for calibration parameters (a) θ_1: laser absorptivity, (b) θ_2: powder-bed porosity, and (c) θ_3: thermal conductivity of the liquid. Reprinted with permission. Copyright © 2018 by Springer-Verlag London Ltd.

mentally measuring absorptivity due to its dependence on multiple parameters (i.e., wavelength, temperature, oxidation, powder size, powder distribution, powder porosity), these experimental results might involve high uncertainty. Therefore, we confidently agree that the estimated distribution for absorptivity is is consistent with the underlying physical phenomena controlling the interactions between the laser and the powder bed.

The narrow range of the posterior distribution of θ_3 can be attributed to its significant effect on the thermal profile and the melt pool size. A unit increase in the liquid thermal conductivity coefficient might lead to a change on the order of $100\,\mathrm{K}$ in the thermal history and in a change between 5 to $10\,\mu\mathrm{m}$ in the melt pool size. Additionally, if extremely high values are used for this parameter, the applied energy would be rapidly transferred to the surroundings and the energy input will reduce, thus the melt pool peak temperature would decrease in an unrealistic manner. Therefore, only a small region of this parameter results in physically meaningful simulations, explaining the narrow posterior distribution.

Next, we use the predictive distributions from Equation 3.15 to assess the performance of the calibrated model via a 6-fold cross validation. Figure 3.9 displays the results of the 6-fold cross validation for each of the three outputs y_i. In the plots, the horizontal axes represent experimental measurements, while the vertical axes are the predicted outputs using the calibrated model with the bars representing the confidence intervals for the predictions. In other words, each point on the plots compares the experiment $y^E(\boldsymbol{x}, \boldsymbol{\theta})$ versus the calibrated model prediction $\mathbb{E}[y^P(\boldsymbol{x})|\boldsymbol{X}^E, \boldsymbol{Y}^E, \boldsymbol{X}^S, \boldsymbol{Y}^S, \boldsymbol{\theta}^*]$, and the red straight line is a reference line representing ideal predictions.

Upon visual inspection, the plots qualitatively show acceptable predictive performance for y_1 (melt pool depth) and y_2 (melt pool width), but less accurate predictions for y_3 (peak temperature), particularly in the case with too low and too high values of y_3. Quantitatively, the error metric MAPE for each output are reported in Table 3.3. We notice that the MAPEs for melt pool depth and width, y_1 and y_2, are relatively low compared to the full range of simulations: 5% and 3%, respectively. These results show that the calibration model is effectively correcting the simula-

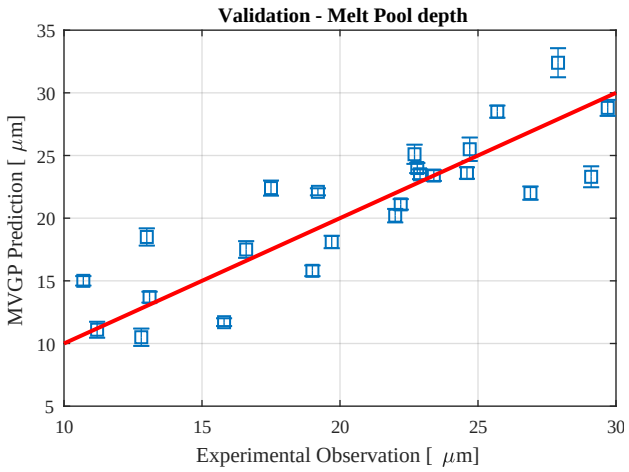

(a)

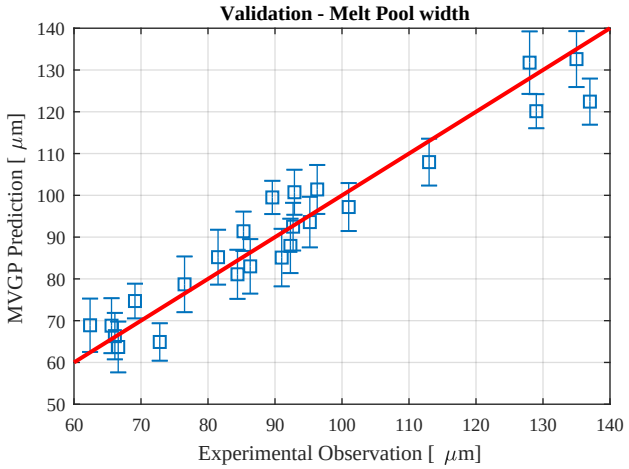

(b)

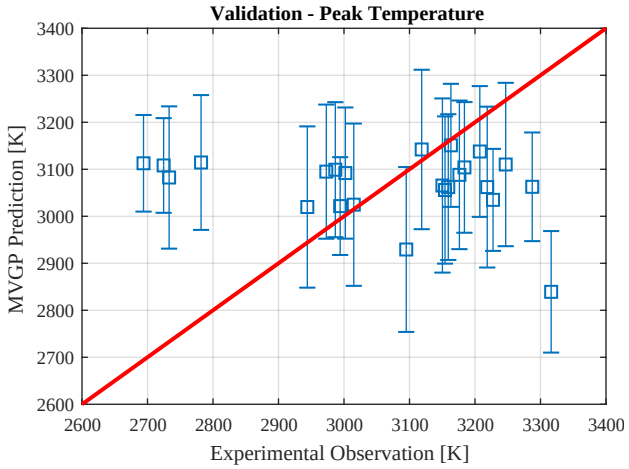

(c)

Figure 3.9: Results of the 6-fold cross validation for the predictions using the calibrated model for (a) y_1: melt pool depth, (b) y_2: melt pool width, and (c) y_3: melt pool peak temperature. Reprinted with permission. Copyright © 2018 by Springer-Verlag London Ltd.

Table 3.3: Mean absolute predictive error (MAPE) of the predictions using the calibrated model. Reused with permission. Copyright © 2018 by Springer-Verlag London Ltd.

Melt pool property	Depth	Width	Peak Temperature
Mean absolute predictive error (MAPE)	$2.42\,\mu\mathrm{m}$	$4.93\,\mu\mathrm{m}$	$159.5\,\mathrm{K}$
MAPE as % of the experimental range	5%	3%	12%

tion model output when we use the Kriging technique in Equation 3.15. However, the predictions for melt pool peak temperature, y_3, show a higher value of MAPE (12% of the simulation range) compared to the predictions for melt pool depth and width. We believe that this is due to the inherent high uncertainty associated with experimental temperature measurements using contactless temperature measurement through pyrometry [60]. The uncertainty in the temperature data can be measured by computing its standard deviation. The average standard deviation of the experimental measurements for y_1, y_2, and y_3 are $3.03\,\mu\mathrm{m}$, $8.14\,\mu\mathrm{m}$, and $306.3\,^{\circ}\mathrm{C}$, respectively. We notice low standard deviations for y_1 and y_2 (6% of the simulation ranges), in contrast to a relatively high standard deviation for y_3 (24% of the simulation range). This is the likely explanation for the high MAPE associated with the predictions of y_3 due to high measurement noise, which signals the need for improving existing measurement techniques or developing new sensors with lower measurement noise.

To support our argument that uncertainty in experimental temperature measurements explain the high reported value of MAPE for y_3, we re-implemented the multivariate calibration procedure with only the melt pool depth and width (y_1 and y_2, respectively) as model outputs. In other words, we excluded the melt pool temperature y_3 as a model output. Figure 3.10 shows the results of the 6-fold cross validation for this calibrated model. We observe that that the cross validation plots show improvement in predictive performance, indicated by more proximity of the blue data points to the red line, narrower confidence intervals, and lower MAPE error values of $2.42\,\mu\mathrm{m}$ and $4.96\,\mu\mathrm{m}$ for y_1 and y_2, respectively. This both supports our claim regarding measurement errors associated with temperature measurements, and also demonstrates satisfactory performance of the

calibrated model.

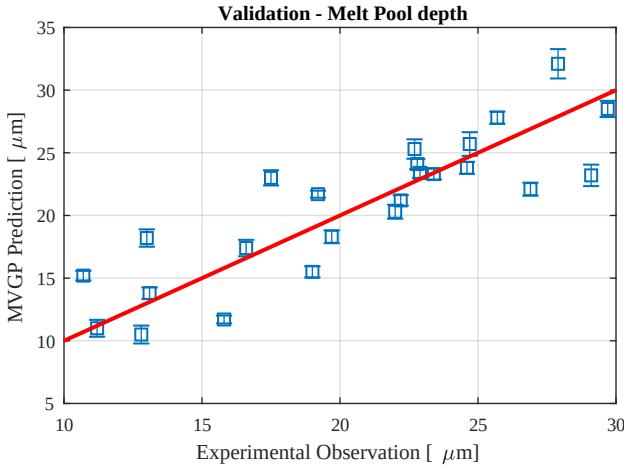

(a)

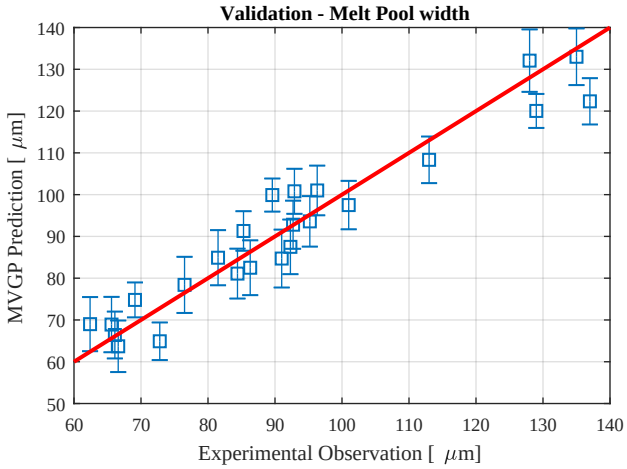

(b)

Figure 3.10: Results of the 6-fold cross validation for the predictions using the calibrated model with only two outputs (a) y_1, (b) y_2. Reprinted with permission. Copyright © 2018 by Springer-Verlag London Ltd.

4. CALIBRATION OF HIERARCHICAL COMPUTER MODELS

The body of literature on statistical calibration of a single computer model is rich, many of them use the so-called two-stage framework by Kennedy and O'Hagan [52]. However, in most engineering problems, the processes are often described not by a single computer model, but by a system of computer models. Many new problems arise when one decides to perform uncertainty quantification (UQ) for a complex system with multiple simulation models. A limited number of research works have investigated the problem of UQ for multiple models, see for example [149, 150, 151, 152, 153]. Additionally, in most cases the models predict multiple quantities of interest (QoI's) rather than merely predicting a single scalar QoI [117, 154], and portions of these QoI's are often unobservable, i.e. no direct experimental measurement can be acquired for the purpose of validation and calibration. Figure 4.1 shows a schematic of a network of integrated computational materials models. The network is used to predict the performance of an additive manufacturing process using various simulation models that are connected through their input and output variables.

In our work, we propose using Bayesian networks, which enables us to handle the challenge of statistical calibration of multi-model systems with unobservable variables. Using a BN, we can have a UQ framework for "a system of computer simulation models" for analyses in two directions: (1) forward and (2) inverse. The BN aggregates information from all available sources (e.g., models, data, etc.) to quantify the uncertainty in the final system QoI [152, 155].

4.1 Hierarchical Models

The following challenges are identified when conducting UQ for engineering systems. First, the system is not analyzed using a single simulation model, but using multiple hierarchically built models to analyze a final quantity of interest (QoI) [149]. Second, the models predict a multiple QoI's – sometimes functional – rather than merely predicting a single scalar QoI [117, 154]. Last but not least, portions of QoI's are often unobservable, i.e. no direct experimental measurement can

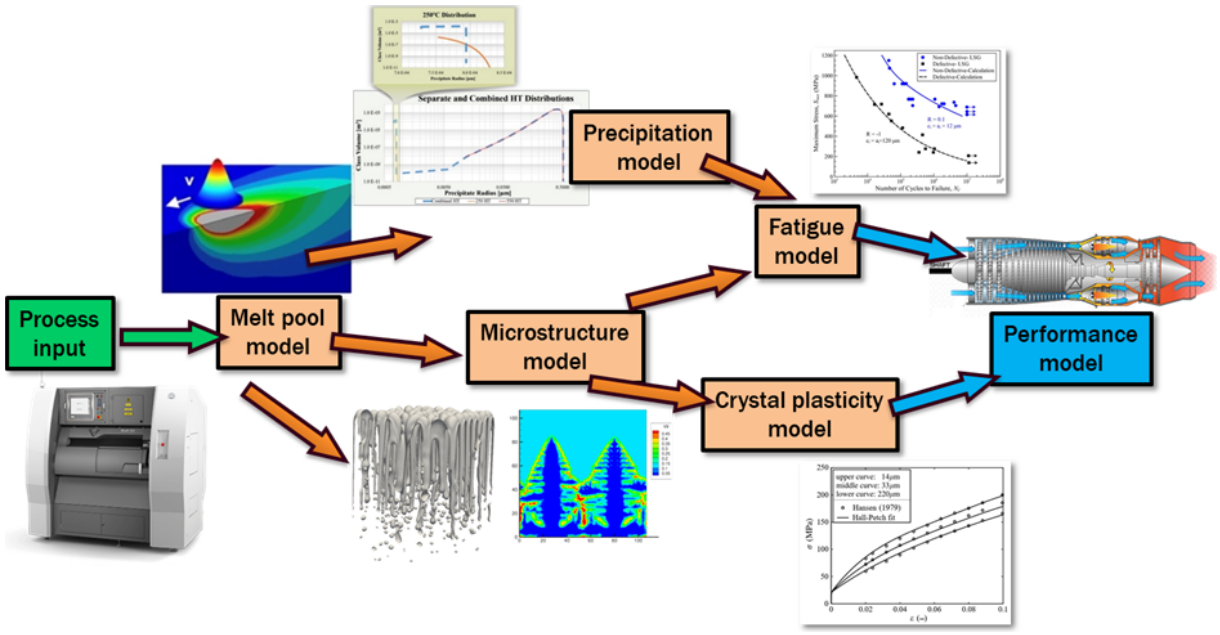

Figure 4.1: Hierarchical modeling in LPBF

be acquired for the purpose of validation and calibration. In our work, we propose using Bayesian networks, which enables us to handle the aforementioned challenges. Using a BN, we can have a UQ framework for "a system of computer simulation models" for analyses in two directions: (1) forward and (2) inverse. The BN aggregates information from all available sources (e.g., models, data, etc.) to quantify the uncertainty in the final system QoI [152, 155].

4.1.1 UQ for hierarchical models

In this section we develop a framework for formal UQ for a system of L-PBF simulation models by utilizing Bayesian networks explained in Section 4.1. The assumption here is that these models – regardless of the number of them – are integrated in a hierarchical fashion. Hence, no feedback is present between the variables. Note that although the models are connected through their input and output variables, often an intermediate data processing is needed in order for outputs of a specific model to be used as inputs to another model. This additional data processing step can be either due to the different time and length scales that each model work with, or different data structure that each model uses. Figure 4.2 shows an example of two L-PBF models in which the complete

coupling cannot be done without a series of intermediate data processing.

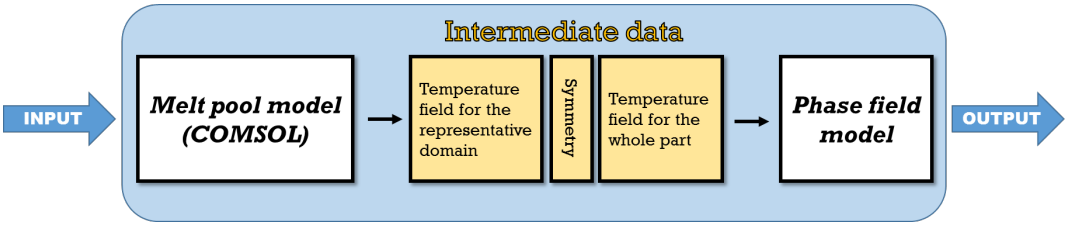

Figure 4.2: Schematic showing the process of coupling a melt pool model with a solidification (phase field) model using the intermediate data processing

The first model (melt pool model) in Fig. 4.2 produces outputs the temperature as a function of location and time $T(x, y, z, t)$ for a specific geometric domain in the part. This temperature information then needs to be expanded for the whole additively manufactured part using the part symmetry. Next, the temperatures at specific points of a 2D plane can be used as inputs and boundary conditions $T_i(x, y, t)$ for the second model (phase field model).

4.2 Methodology

In this section we describe our methodology to solve a problem which arises in many engineering settings including metal additive manufacturing. Mathematical examples are provided to demonstrate the performance of the proposed methodology.

4.2.1 Bayesian calibration of hierarchical models

Consider a complex process for which modeling and analysis is done using N multiple physics-based computer simulation models. We denote each model by $M_i, i = 1, \cdots, N$. Each model M_i takes as input two distinct vectors: (1) a vector of *control inputs*, denoted by $\boldsymbol{x}_i$, and (2) a vector of *calibration parameters*, $\boldsymbol{\theta}_i$. The true QoI's that each model aims to estimate is denoted by $\boldsymbol{y}_i$, and the vector of predictions generated by running the model M_i is denoted by $\hat{\boldsymbol{y}}_i$. The models are connected hierarchically, which means that the outputs of some of the models are used as inputs to some other models. Figure 4.3 shows a graph for a sample network consisted of four simulation

models. It can be seen that only part of the output of M_1 – denoted by $\hat{y}_{1b}$ – has been used as input to M_2. Similarly, we notice that outs of both M_2 and M_3 have been used as inputs to M_4. The final QoI that the system aims to predict is y_4.

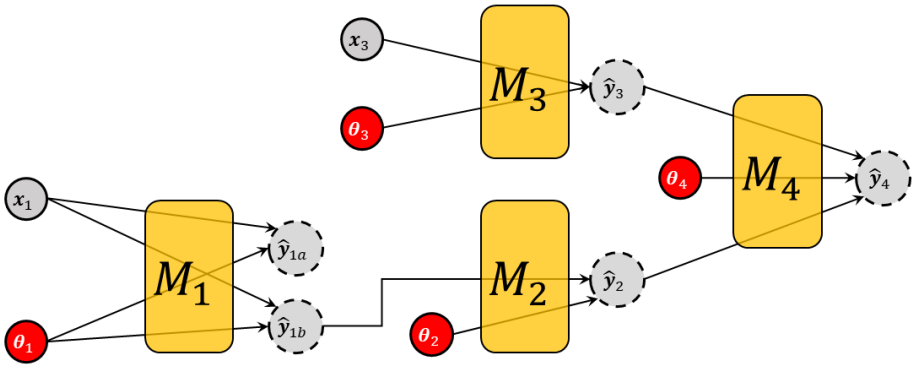

Figure 4.3: Graph of a sample hierarchical network of simulation models

Statistical calibration of the physics-based models using experimental observations is a vital task without which one cannot confidently rely on the simulation model predictions. When dealing with hierarchical models, an efficient approach for simultaneous calibration of multiple models is to use a Bayesian network (BN), see for example [149, 152]. BN is a tool that captures the relationships between variables and parameters in a network of models using a directed graph and conditional probabilities [156].

We proceed with briefly reviewing the mechanics of calibrating a hierarchical system consisted of two computer models using a BN. Consider a process that can be modeled using two computer models M_1 and M_2 that are used hierarchically as follows: the first model M_1 takes vector $\boldsymbol{x}$ as the control input and $\boldsymbol{\theta}_1$ as the calibration parameter. Outputs of M_1 can be split into two vectors of observable and unobservable quantities $\hat{\boldsymbol{y}}_{1Q}$ and $\hat{\boldsymbol{y}}_{1U}$, respectively. The output $\boldsymbol{y}_{1U}$ is unobservable in the sense that experimental observations needed for calibration is not available. The reason for this lack of experimental data can be due to technological limitations or other considerations such as cost. For the observable output $\boldsymbol{y}_{1Q}$, we have the experimental dataset $\boldsymbol{D}_{1Q}$. The second model

M_2 takes vectors $\hat{\boldsymbol{y}}_{1U}$ as input and $\boldsymbol{\theta}_2$ as the calibration parameters. The output of M_2 is the vector $\hat{\boldsymbol{y}}_2$, which is observed by the dataset $\boldsymbol{D}_2$. The Bayesian network for this two-model system is shown in Figure 4.4.

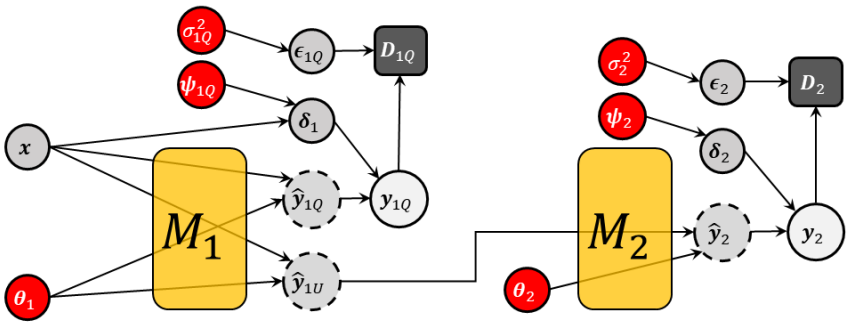

Figure 4.4: Bayesian network for a two-model system with unobservable variables

Notice that in the network of Figure 4.4, additional nodes of $\boldsymbol{\epsilon}_{1Q}$ and $\boldsymbol{\delta}_{1Q}$ are added for the first model M_1. Similarly, nodes $\boldsymbol{\epsilon}_2$ and $\boldsymbol{\delta}_2$ are added for M_2. The reason for these additional nodes is that the Bayesian calibration model by Kennedy and O'Hagan [52] requires a model inadequacy function $\boldsymbol{\delta}(\cdot)$ with hyperparameter vector ψ (see [109]), along with a zero-mean measurement error $\boldsymbol{\epsilon}$ with unknown variance σ^2 for each experimental dataset. We have:

$$\boldsymbol{y}_{1Q} = \hat{\boldsymbol{y}}_{1Q}\left(\boldsymbol{x}; \boldsymbol{\theta}_1\right) + \boldsymbol{\delta}_{1Q}(\boldsymbol{x}) + \boldsymbol{\epsilon}_{1Q} \tag{4.1}$$

$$\boldsymbol{y}_2 = \hat{\boldsymbol{y}}_2\left(\boldsymbol{y}_{1U}; \boldsymbol{\theta}_2\right) + \boldsymbol{\delta}_2(\boldsymbol{y}_{1U}) + \boldsymbol{\epsilon}_2. \tag{4.2}$$

We define the set of network parameters $\boldsymbol{\Phi} = \left\{\boldsymbol{\theta}_1, \boldsymbol{\theta}_2, \boldsymbol{\psi}_{1Q}, \boldsymbol{\psi}_2, \sigma^2_{1Q}, \sigma^2_2\right\}$. It follows that the posterior probability density function of $\boldsymbol{\Phi}$ is proportional to the joint likelihood $L(\boldsymbol{D}_{1Q}, \boldsymbol{D}_2|\boldsymbol{\Phi})$ multiplied by the prior density function $\pi(\boldsymbol{\Phi})$. Assuming independent datasets we get two separable likelihoods:

$$P(\boldsymbol{\Phi}|\boldsymbol{D}_{1Q}, \boldsymbol{D}_2) \propto \pi(\boldsymbol{\Phi}) L(\boldsymbol{D}_{1Q}, \boldsymbol{D}_2|\boldsymbol{\Phi}) = \pi(\boldsymbol{\Phi}) L(\boldsymbol{D}_{1Q}|\boldsymbol{\Phi}) L(\boldsymbol{D}_2|\boldsymbol{\Phi}) \tag{4.3}$$

$$\pi(\boldsymbol{\Phi}) = \pi(\boldsymbol{\theta}_1)\pi(\boldsymbol{\theta}_2)\pi(\boldsymbol{\psi}_{1Q})\pi(\boldsymbol{\psi}_2)\pi(\sigma^2_{1Q})\pi(\sigma^2_2) \tag{4.4}$$

Equation 4.4 is simply due to the assumption of independence among the parameters. Throughout this report, we conduct Bayesian updating to estimate the network parameters Φ using Metropolis-Hastings sampling.

4.2.2 Handling lack-of-data

Here, we introduce a auxiliary variable $\boldsymbol{\xi}_2$ to account for the lack of data (knowledge) about $\boldsymbol{y}_{1U}$. We use the Kenendy and O'Hagan's tradition and assume this variable to follow a Gaussian process with mean zero and some covariance structure. Then, using the data about $\boldsymbol{y}_2$, we would like to make inference about the hyperparameters of $\boldsymbol{\xi}_2$. The network corresponding to this example is shown in Figure 4.5.

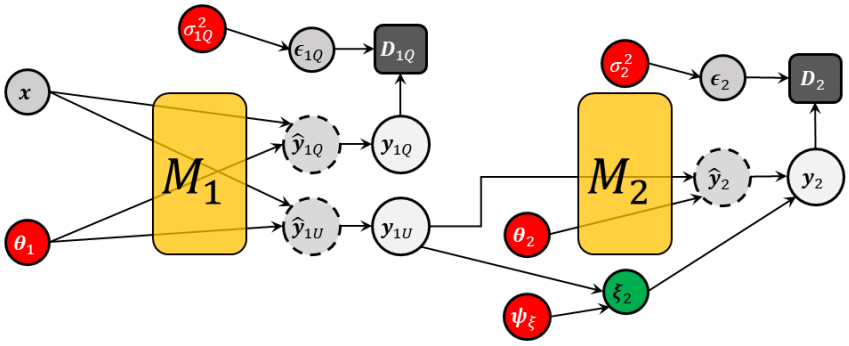

Figure 4.5: Bayesian network of a two-model system with unobservable response for model 1

For our example, we rewrite the equations for each model:

$$\boldsymbol{y}_1 = \begin{pmatrix} y_{1Q} \\ y_{1U} \end{pmatrix} = \begin{pmatrix} \hat{y}_{1Q}\left(x, \theta_1\right) + \boldsymbol{\epsilon} \\ \hat{y}_{1U}\left(x, \theta_1\right) + \boldsymbol{\epsilon} \end{pmatrix}, \tag{4.5}$$

$$y_2 = \hat{y}_2\left(y_{1U}, \theta_2\right) + \xi_2(y_{1U}) + \boldsymbol{\epsilon}. \tag{4.6}$$

Next, we write down the joint probability distribution of the network $f(\mathcal{U})$ as follows.

$$f(\mathcal{U}) = \pi(\theta_1) \cdot \pi(\theta_2) \cdot \pi(r_\xi) \cdot \pi\left(\sigma_\xi^2\right) \cdot p\left(\boldsymbol{D}_{1Q} | y_{1Q}\right) \cdot p\left(\boldsymbol{D}_2 | y_2\right). \tag{4.7}$$

For the auxiliary variable $\boldsymbol{\xi}_t$, we assume a zero-mean Gaussian distribution with squared exponential (SE) covariance structure as follows.

$$\boldsymbol{\xi}_t \sim \mathcal{N}(\mathbf{0}, \Sigma_\xi) \tag{4.8}$$

$$\Sigma_\xi = \left[C_\xi(\boldsymbol{x}_i, \boldsymbol{x}_j)\right]_{i,j} = \left[\sigma_\xi^2 \exp\left(-\left(\boldsymbol{x}_i - \boldsymbol{x}_j\right)^T \boldsymbol{r}_\xi \left(\boldsymbol{x}_i - \boldsymbol{x}_j\right)\right)\right]_{i,j} \tag{4.9}$$

Following the KO's tradition, we assume a zero-mean Gaussian distribution for the measurement errors ε_{1Q} and ε_2. In a general multi-dimensional setting we get

$$\boldsymbol{\varepsilon} \sim \mathcal{N}(\mathbf{0}, \Sigma_\varepsilon) \tag{4.10}$$

$$\Sigma_\varepsilon = \sigma_\varepsilon^2 \boldsymbol{I}. \tag{4.11}$$

We denote the tuple of hyperparameters with $\Psi = \left(\sigma_\xi^2, \boldsymbol{r}_\xi\right)$. The following prior distributions are used for the calibration parameters and the hyperparameters.

$$\sigma_\xi^2 \sim \text{inverse-gamma}(\alpha = 2, \beta = 1) \tag{4.12}$$

$$r_\xi \sim \text{log-normal}(\alpha = 1, \beta = 1) \tag{4.13}$$

4.2.2.1 *Prediction*

Now that the estimates for all the parameters are known, we use the kriging formula and cross-validate the calibrated model. Consider we want to predict the output of S new inputs; hence $\boldsymbol{X}^P$ is of size $S \times \kappa$. For computing the output $\boldsymbol{Y}^P$, we essentially use the experimental values in addition to running the simulation with calibrated set of parameters $\boldsymbol{\theta}^*$. We have:

$$\mathbb{E}[\boldsymbol{Y}^P|\boldsymbol{Y}^E] = \boldsymbol{\mu}(\boldsymbol{X}^P) + \boldsymbol{\Sigma}^{PE}(\boldsymbol{\Sigma}^{EE})^{-1}(\boldsymbol{Y}^E - \boldsymbol{\mu}(\boldsymbol{X}^E)), \tag{4.14}$$

where:

$$\boldsymbol{\mu}(\boldsymbol{X}^P) = \hat{y}_2(\boldsymbol{X}^P; \boldsymbol{\theta}_2^*) \tag{4.15}$$

$$\boldsymbol{\Sigma}^{PE} = [C_\xi(\boldsymbol{x}_i^P, \boldsymbol{x}_j^E; \boldsymbol{\Psi}^*)]_{\substack{i=1\ldots S \\ j=1\ldots N_2}}, \tag{4.16}$$

$$\boldsymbol{\Sigma}^{EE} = \boldsymbol{\Sigma}_\epsilon + \boldsymbol{\Sigma}_\xi = \boldsymbol{\Sigma}_\epsilon + [C_\xi(\boldsymbol{x}_i^E, \boldsymbol{x}_j^E; \boldsymbol{\Psi}^*)]_{\substack{i=1\ldots N_2 \\ j=1\ldots N_2}}. \tag{4.17}$$

4.2.3 Illustrative example

In this section, we conduct Bayesian multi-level calibration for a mathematical example. Instead of using simulation models, we employ analytical functions according to the Figure 4.5. Briefly, the first model has two responses y_{1Q} and y_{1U} that are observable and unobservable, respectively. The second model has a single response y_2, which is observable. These response are become computation nodes $(\hat{y}_{1Q}, \hat{y}_{1U}, \hat{y}_2)$ according to the following polynomial functions:

$$\hat{y}_{1Q}(x; \theta_1) = c_1 x + \theta_1 \tag{4.18}$$

$$\hat{y}_{1U}(x; \theta_1) = x^2 + \theta_1^2 \tag{4.19}$$

$$\hat{y}_2(y_{1U}; \theta_2) = c_2(\theta_2^2 + y_{1U}^2) + \theta_2. \tag{4.20}$$

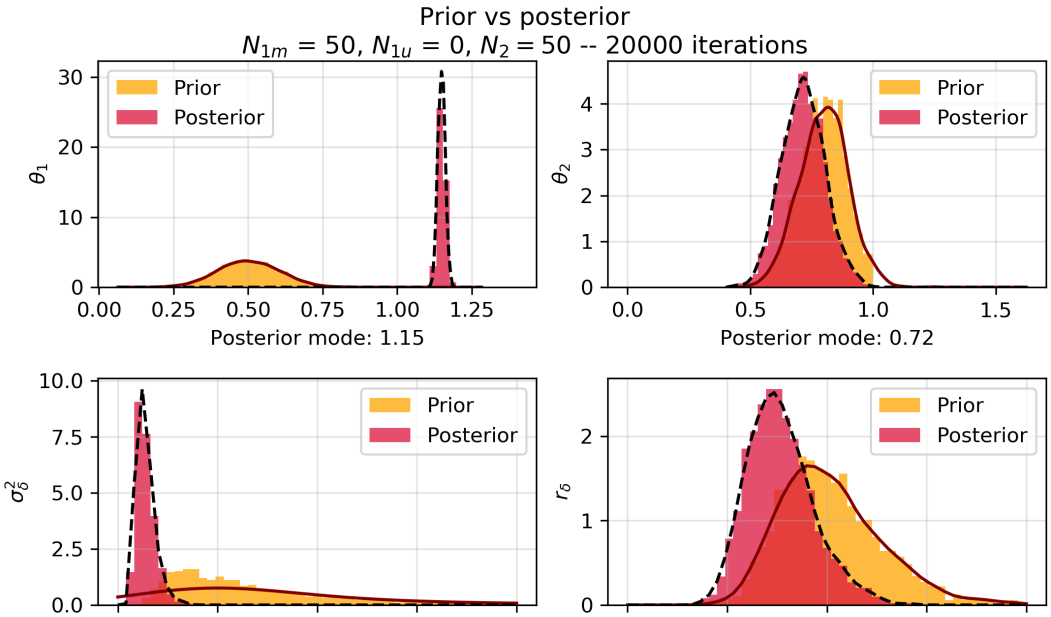

Figure 4.6: Histograms and kernel density estimates of the posterior distributions for the example parameters and hyperparameters

Using single-component Metropolis-Hastings algorithm, the posterior distributions of parameters θ_1 and θ_2 along with the hyperparameters σ_δ^2 and r_δ that are defined in Equations 4.7-4.10 are computed after 20,000 iterations with 25% burn-in period and thinning every fifth sample. Figure 4.6 shows the histograms and kernel density estimates of the posterior distributions for $\theta_1, \theta_2, \sigma_\delta^2$, and r_δ. Note that in this example, we do not estimate the measurement error; instead, we assume that it is known and we use it in generating synthetic data for the example.

Given a reasonable measurement error, the model performance is excellent. The posterior distribution of the θ_1 has a mode of 1.15, which is very close to the true value of 1.20. The posterior distribution of the θ_2 is informative with mode 0.72, while the true value of θ_2 is 0.50. However, for prediction purposes we use the estimates of ψ_ξ to correct for lack of data. Figure 4.7 shows a 10-fold cross-validation when predicting y_2. It can be seen that the auxiliary variable introduced in the model appropriately adjusts the predictions and results in high accuracy.

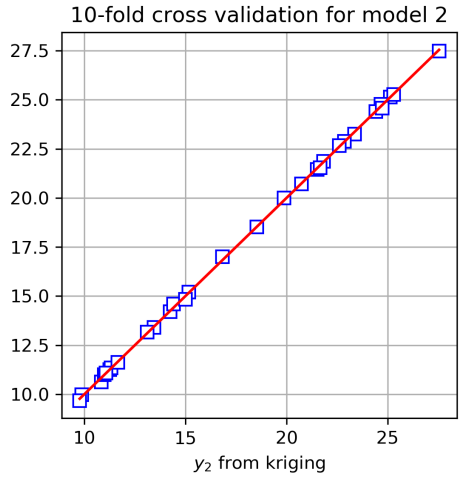

Figure 4.7: Cross validation for M_2

4.3 Case Study of LPBF

In this section we apply the model presented in Section 4.2.2 to a real-world problem related to LPBF, where calibrating hierarchical models is needed. In general, LPBF is a complex process that many researchers have been studying and developing computer simulation models for, see for example [157, 33, 158]. The complexity of LPBF requires modeling and simulation for different parts of the process and at different scales, as schematically suggested by the hierarchical network of simulation models in Figure 4.1. Indeed, systematic calibration and uncertainty quantification of model parameters for this network is a vital task for robust predictions and usability of the models to guide the design and optimization [159]. The current case study demonstrates how our approach to calibration is effective when one seeks to (1) calibrate multiple physics-based models that are connected in a hierarchical fashion, and (2) some of these models have unobservable variables.

4.3.1 The hierarchical models

For this case study, we deem to calibrate a two-model hierarchical network. We explain the hierarchical network as follows. The network starts with a finite element thermal model (also called the *melt pool* model) as the upstream model. Outputs of this melt pool model are partially used as inputs to another downstream physics-based model called the *phase field* (PF) model. Figure

4.8 schematically shows the relationships between the variables of each of these two models. We notice that given the process parameters such as laser power and speed the melt pool model predicts useful quantities including the melt pool dimensions, along with temperature and solidification gradients at different locations on the melt pool surface. Given the solidification gradient and solidification speed for a particular location (G_0 and S_0, respectively), we can use the PF model to predict quantities such as primary dendrite arm spacing (PDAS), denoted by λ, which is of great importance when studying the microstructure of an additively manufactured part. More details about the melt pool model and the phase field model are provided in Sections 4.3.1.1 and 4.3.1.2, respectively.

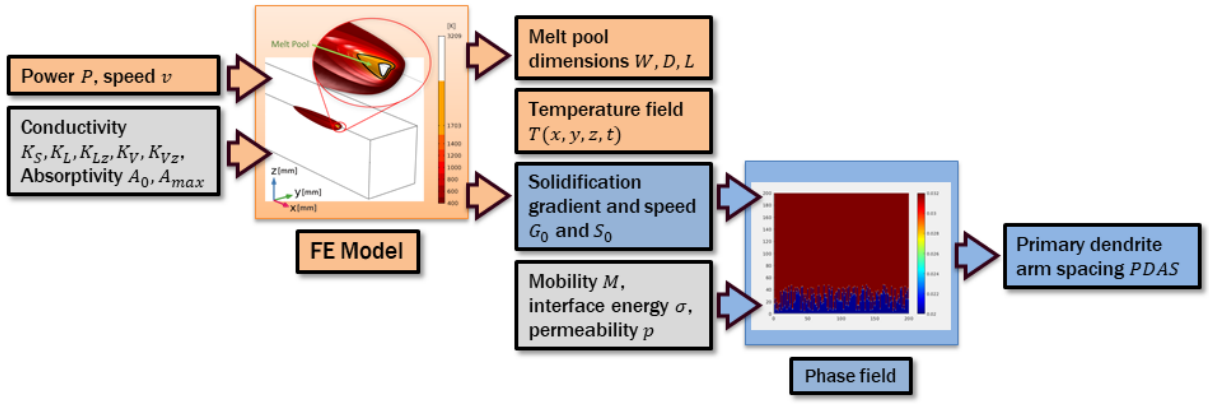

Figure 4.8: Relationships between the variables of a two-model system

4.3.1.1 The melt pool model

The melt pool model used here is an improved version of the melt pool model described in Section 3.3.1. The model was modified for analyzing a new alloy system (IN718) with shorter computation time. Our collaborators developed a three-dimensional FE based thermal model implemented in COMSOL Multiphysics® heat transfer module to study melt pool characteristics, including geometry and thermal profiles, during the fabrication of single tracks printed in a thin layer of powder on top of a solid substrate. The thermal model includes phase-dependent ther-

mophysical properties which are used to approximate heat and mass transport phenomena such as melting, solidification, vaporization, and keyhole formation. The powder layer was assumed as a $30\ \mu\mathrm{m}$ continuum medium over a $1\ \mathrm{mm}$ thick substrate. Ni5wt%Nb (NiNb) alloy as a binary proxy of IN718 was selected as the material for both the powder layer and the substrate.

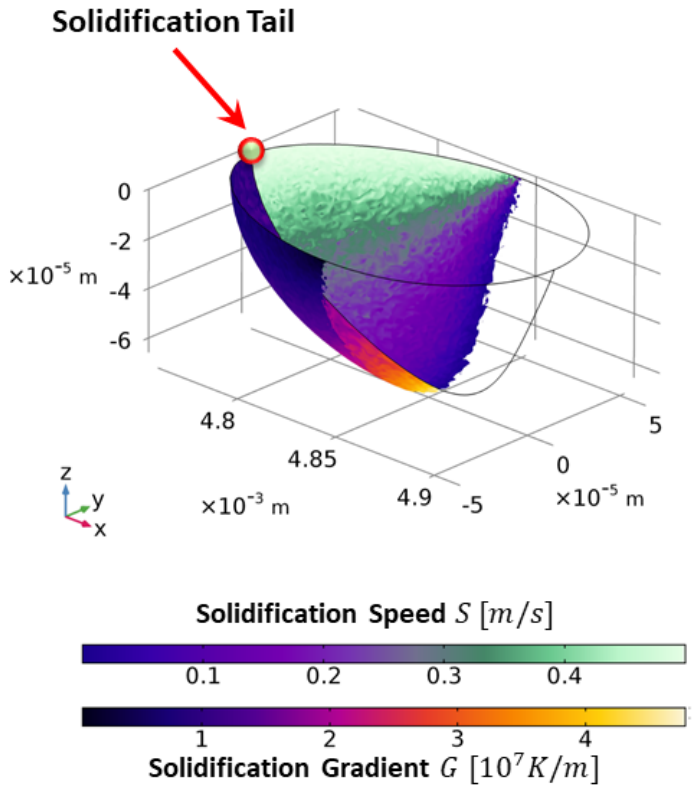

Figure 4.9: A sample outputs of the melt pool model

Note that compared with Section 3.3.1, we are working with a different set of melt pool model outputs. Particularly, not only we are looking at quantities such as melt pool dimensions and temperature gradients, but also we are quantifying the solidification gradient and solidification speed (denoted by G and S, respectively) for every point on the surface of the melt pool. A representative output of the melt pool model that shows G and S surface is shown in Figure 4.9(a). We can see that the melt pool shape is computed in three dimensions. Additionally, solidification gradient and speed are evaluated across the entire melt pool boundary and color coded. Both of

Table 4.1: Specifications of the melt pool model

The melt pool model	
Control Inputs, $\boldsymbol{x}_1$	
P: Laser power	$[\mathrm{W}]$
v: Laser speed	$[\mathrm{m/s}]$
Model Parameters, $\boldsymbol{\theta}_1$	
K_S: Thermal conductivity coefficient solid	$[\mathrm{W/mK}]$
K_L: Thermal conductivity coefficient liquid	$[\mathrm{W/mK}]$
K_{Lz}: Anisotropic thermal conductivity coefficient liquid	$[\mathrm{W/mK}]$
K_V: Thermal conductivity coefficient vapor	$[\mathrm{W/mK}]$
K_{Vz}: Anisotropic thermal conductivity coefficient vapor	$[\mathrm{W/mK}]$
A_0: Bulk absorptivity of powder	$[\%]$
$A_{\max}$: Max absorptivity of powder	$[\%]$
Outputs, $\boldsymbol{y}_1$	
D: Melt pool depth	$[\mu\mathrm{m}]$
W: Melt pool width	$[\mu\mathrm{m}]$
L: Melt pool length	$[\mu\mathrm{m}]$
T_0: Temperature	$[^\circ\mathrm{C}]$
S_0: Solidification rate	$[\mathrm{m/s}]$
G_0: Solidification gradient	$[^\circ\mathrm{C/m}]$

these quantities (G and S) are symmetric about the laser scan path. Hence, for a specific point such as the solidification tail (as indicated in the Figure), we can report temperature, solidification gradient, and solidification speed. We denote these three values by T_0, G_0 and S_0, respectively. We can specify the whole melt pool model by defining three vectors: (1) control inputs $\boldsymbol{x}_1$, (2) model parameters $\boldsymbol{\theta}_1$, and (3) outputs $\boldsymbol{y}_1$. These vectors are described in detail in Table 4.1. As we will describe in the next subsection, part of this model outputs is used as input to the PF model.

4.3.1.2 The phase field model

A phase field model is used in this section to investigate the solidification microstructure of AM parts. It is a powerful technique for describing complex microstructural evolutions without needing to track the moving interface, as opposed to the classical sharp interface models. By coupling the PF model with a FE based thermal model, quantifiable predictions of solidification phenomenon during LPBF can be achieved. In this work, our collaborators adopt the phase field

model with finite interface dissipation introduced by Steinbach et al. [160], Zhang and Steinbach [161] to investigate the rapid solidification process during LPBF of Ni-5 wt.% Nb (Ni-3.2 at.% Nb) alloy. The model has been proven to be a capable tool to describe the extremely non-equilibrium conditions as seen in rapid solidification. At its heart, the PF model uses finite difference method to numerically solve the following phase-field and concentration evolution equations:

$$\phi_\alpha \dot{c_\alpha} = \nabla(\phi_\alpha D_\alpha \nabla c_\alpha) + p^{\text{int}} \phi_\alpha \phi_\beta \left(\frac{\partial f_\beta}{\partial c_\beta} - \frac{\partial f_\alpha}{\partial c_\alpha} \right) + \phi_\alpha \dot{\phi_\alpha} \left(c_\beta - c_\alpha \right) \tag{4.21}$$

$$\phi_\beta \dot{c_\beta} = \nabla(\phi_\beta D_\beta \nabla c_\beta) + p^{\text{int}} \phi_\alpha \phi_\beta \left(\frac{\partial f_\alpha}{\partial c_\alpha} - \frac{\partial f_\beta}{\partial c_\beta} \right) + \phi_\beta \dot{\phi_\beta} \left(c_\alpha - c_\beta \right) \tag{4.22}$$

$$\dot{\phi_\alpha} = K \left\{ \sigma_{\alpha\beta} [\nabla^2 \phi_\alpha + \frac{\pi^2}{\eta^2} (\phi_\alpha - \frac{1}{2})] - \frac{\pi^2}{8\eta} \Delta g_{\alpha\beta}^{phi} \right\} \tag{4.23}$$

$$K = \frac{8 p^{\text{int}} \eta \mu_{\alpha\beta}}{8 p^{\text{int}} \eta + \mu_{\alpha\beta} \pi^2 (c_\alpha - c_\beta)^2} \tag{4.24}$$

$$\Delta g_{\alpha\beta}^{\phi} = f_\alpha - f_\beta + \left(\phi_\alpha \frac{\partial f_\alpha}{c_\alpha} - \phi_\beta \frac{\partial f_\beta}{c_\beta} \right) (c_\alpha - c_\beta) \tag{4.25}$$

In the above equations, $\sigma_{\alpha\beta}$, η, $\phi_{\alpha/\beta}$, $c_{\alpha/\beta}$, and c are the interfacial energy, the interface width, the phase fractions of α/β phases, the phase concentrations of α/β phases, and the overall concentration, respectively. D_α, D_β are the chemical diffusivities in the α and β phases, respectively, and p^{int} is the interface permeability defined as: $p^{\text{int}} = \frac{8M}{a\eta}$. M is the atomic mobility and a is the lattice constant. $\mu_{\alpha\beta}$ is the interfacial mobility, K is the kinetic coefficient describing the effect of finite diffusion and redistribution at the interface and $\Delta_{\alpha\beta}^{\phi}$ phi is the chemical driving force. Further information on the physical meaning of the interface permeability, p^{int}, can be found in the referenced papers [160].

A dynamic time step is adopted to ensure the numerical stability. Neumann boundary conditions are applied to all boundaries. A Fortran code with OpenMP parallelization directives was

utilized to reduce the computational time. To investigate the general features of the microstructure, a 2-dimensional simulation domain was used. Figure 4.10 shows a representative output of the PF model. Similar to the melt pool model, We can specify the phase field model by defining three vectors: (1) control inputs $\boldsymbol{x}_2$, (2) model parameters $\boldsymbol{\theta}_2$, and (3) outputs $\boldsymbol{y}_2$. These vectors are described in detail in Table 4.2.

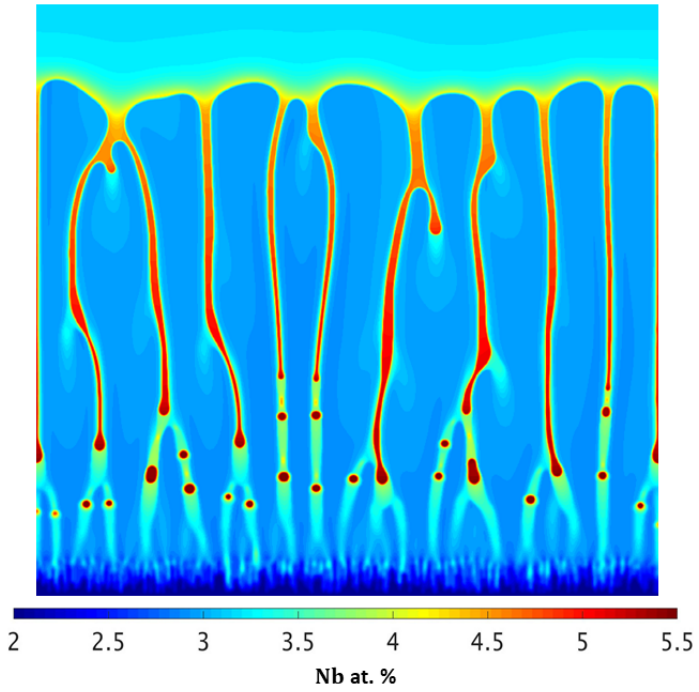

Figure 4.10: A sample output of the phase field model

4.3.2 Coupling models using GP surrogates

For any analysis, uncertainty quantification, and calibration purposes we need a framework for connecting the computer models in our network. To achieve this, we replace these computer models with fast GP surrogates in the form of Python objects. In fact, directly coupling computer codes can be extremely difficult due to programming and logistic reasons. Recent examples of using surrogates for coupling multiple simulation models can be seen in [149, 162, 163]. To build the GP surrogates we used LHS of the size 100-200 depending on the simulations run time to train

Table 4.2: Specifications of the phase field model

The phase field model	
Control Inputs, $\boldsymbol{x}_2$	
S: Solidification rate	$[\mathrm{m/s}]$
G: Solidification gradient	$[^{\circ}\mathrm{C/m}]$
Model Parameters, $\boldsymbol{\theta}_2$	
σ: Interface energy	$[\mathrm{J/cm^2}]$
M: Interface mobility	$[\mathrm{cm^4/Js}]$
p^{int}: Interface permeability	$[\mathrm{cm^3/Js}]$
Outputs, $\boldsymbol{y}_2$	
λ: Primary dendrite arm spacing (PDAS)	$[\mathrm{nm}]$
k_V: Velocity dependent partition coefficient	[-]

the GP and estimate the hyperparameters. Note that compared to the Section 3.1.1, for simplicity we have used multiple independent GP surrogates for each model instead of building a single multi-output GP. Another difference is that instead of using square exponential covariance structure, we used the Matérn covariance function $C_\nu(d)$ in which covariance between two points separated by d distance units is given by

$$C_\nu(d) = \frac{2^{1-\nu}}{\Gamma(\nu)} \left(\frac{\sqrt{2\nu}d}{l} \right)^{\nu} K_\nu \left(\frac{\sqrt{2\nu}d}{l} \right) \tag{4.26}$$

where Γ is the gamma function, K_ν is the modified Bessel function of the second kind, and l and ν are non-negative parameters of the covariance. We chose $\nu = 1.5$ which guarantees differentiability.

To estimate the hyperparameters Python default optimizer was used which employs the L-BFGS-B algorithm developed by Byrd et al. [164]. To evaluate the accuracy of the GP surrogates, k-fold cross-validation was conducted for each GP training. Figures 4.11(a) and 4.11(b) show the results of cross-validation for melt pool width (W) and solidification gradient at the tail (G_0), respectively. A total of 238 simulation runs were used with an average of approximately 5 minutes per run. The data were randomly divided into 17 folds. Figure 4.11(c) shows the result of

cross-validation for primary dendrite arm spacing at the melt pool solidification tip, (λ). A total of 91 simulation runs were used with an average of approximately 4 hours per run. The data were randomly divided into 13 folds. A 10-fold cross validation was performed for the surrogate model and the results are displayed in In the plots, the horizontal axes represent the outputs of the computer simulation model, while the vertical axes show the predicted outputs using the GP surrogates with the bars representing confidence intervals for these predictions. The orange line represents the ideal case with surrogate model predictions are in full agreement with computer model simulations. It can be seen that the predictive performance of the surrogate models are satisfactory. Also, the reported MAPE values in the Figure indicate satisfactory performance.

In order for the reader to understand better how the two hierarchical models are coupled, we summarize the procedure as follows. Consider that we are interested in analyzing the microstructure of the solidification tail, as shown in Figure 4.9, for a specific LPBF process parameters (P and v). The process parameters constitute the input vector $\boldsymbol{x}_1$ as described in Table 4.1. Once $\boldsymbol{x}_1$ is known, we can use the trained GP surrogate model and input $\boldsymbol{x}_1$ and $\boldsymbol{\theta}_1$ to estimate G_0 and S_0. Note that, because the solidification tail is the very last point on the melt pool solidification front, its solidification speed equals the laser scan speed, hence $S_0 = v$. This means that we will not need to use the surrogate model to estimate S_0. Solidification speed and gradient of the solidification tail constitute the input vector $\boldsymbol{x}_2$ as described in Table 4.2. We can then use the trained GP surrogate model and input $\boldsymbol{x}_2$ and $\boldsymbol{\theta}_2$ to estimate the microstructure the primary dendrite arm spacing (λ).

It is worthwhile to remember that each of the described models have their own set of calibration parameters, as shown in the gray boxes in Figure 4.8. Also, note that out of six different outputs of the melt pool model (W, D, L, T_0, S_0, G_0), experimental observation of only melt pool width and depth (W and D) are practical. When dealing with calibrating the described two-model system one faces the following challenges. First, although the melt pool model can be calibrated independently using melt pool width and depth experimental observations; however, there is no guarantee that the unobservable outputs of the calibrated melt pool model (e.g. solidification gradients) result in satisfactory PDAS predictions when used in the PF model. Second, the PF model cannot be

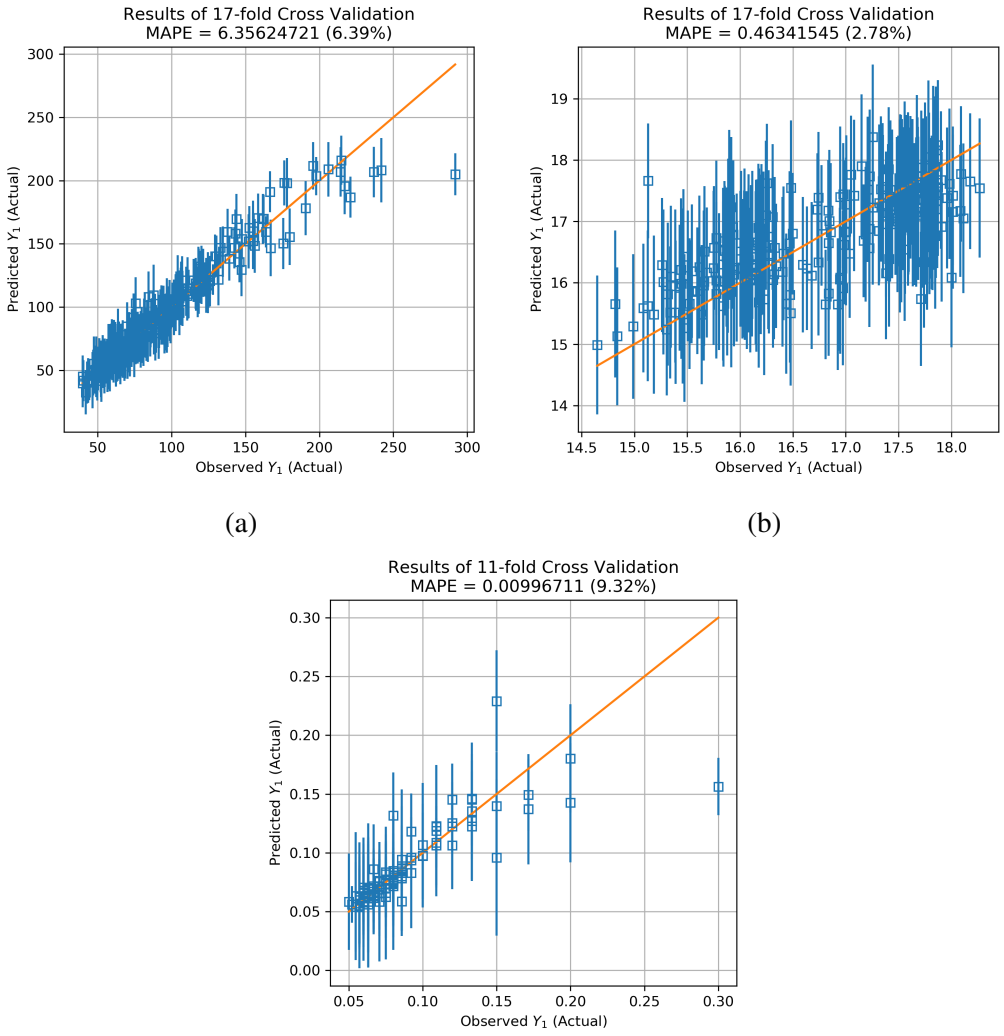

Figure 4.11: Cross-validation of GP surrogates for (a) melt pool width, W; (b) solidification gradient at the tail, G_0; and (c) primary dendrite arm spacing, λ

independently calibrated because the inputs are not observable experimentally. We proceed with employing the model proposed in Section 4.2.2 to rise to the aforementioned challenges.

4.3.3 Experiments

Gas atomized Ni-5wt.%Nb powder was provided by Nanoval GmbH & Co. KG and used to additively manufacture LPBF NiNb. Single tracks were printed using a 3D Systems ProX DMP 200 equipped with a fiber laser with a Gaussian profile λ = 1070 nm, and beam size = 100 μm.

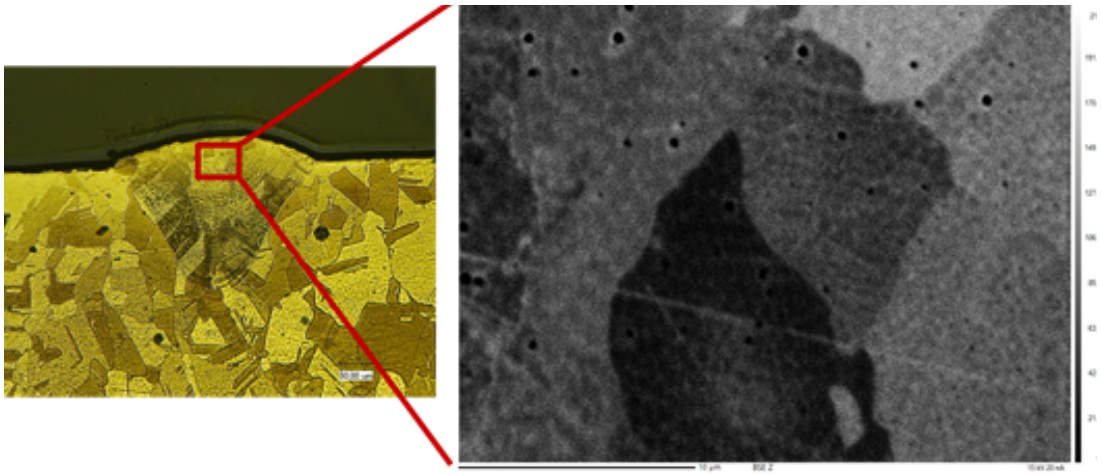

Figure 4.12: Sample melt pool from a single track and segregation

Argon was used as inert protective atmosphere during fabrication. Tracks with $10\,\mathrm{mm}$ length and spaced $1\,\mathrm{mm}$ apart were printed on a Ni-5wt.%Nb base plate. Cross sections of the single tracks were wire cut using wire electrical discharge machining (EDM), and these specimens were polished down to 0.25 μm with water-based diamond suspension polishing solutions. Kalling's Solution No. 2 (5 g $CuCl_2$, 100 mL HCl, and 100 mL ethanol) was used to etch the Ni-5wt.%Nb single tracks to obtain optical micrographs.

Optical microscopy (OM) was carried out using a Keyence VH-X digital microscope equipped with a VH-Z100 wide range zoom lens. Width and depth measurements were taken using the VH-X software. Three cross sections were measured for each track, and the displayed width and depth values are averaged from these measurements. Backscattered electron (BSE) images of polished single tracks were captured at 15 kV and 30 nA. BSE images were processed using ImageJ® software [165] in order to determine PDAS at different locations along select single tracks. The displayed PDAS values were averaged from 30 measurements at each location. Figure 4.12 shows sample OM and SEM images for a representative single track. The images were demonstrate transverse cross-sections of melt pools. The microstructure can conveniently be characterized using the SEM images and segregation can be quantified.

4.3.4 Calibration results

We employed a fully Bayesian approach to estimate the network calibration parameters, $\boldsymbol{\theta}_1, \boldsymbol{\theta}_2$, and the set of hyperparameters, $\boldsymbol{\Psi} = \left\{r_{1Q,\delta}, r_{2,\xi}, \sigma^2_{1Q,\delta}, \sigma^2_{2,\epsilon}, \sigma^2_{1Q,\epsilon}, \sigma^2_{2,\epsilon}\right\}$ as introduced in Section 4.2.2. The following prior distributions were used:

$$\theta_\cdot \sim \text{Uniform}(\alpha_i^\theta, \beta_i^\theta) \tag{4.27}$$

$$r_{\cdot,\delta} \sim \text{Log-Normal}(\alpha = 0, \beta = 1/4) \tag{4.28}$$

$$\sigma^2_{\cdot,\epsilon} \sim \text{Inverse-Gamma}(\alpha = 2, \beta = 1), \tag{4.29}$$

where $(\alpha_i^\theta, \beta_i^\theta)$ indicate the lower and upper bounds for the uniform distributions as recommended by the domain expert. For the roughness parameters, $r_{\cdot,\delta}$ log-normal priors were used to ensure positivity. For the measurement error variance $\sigma^2_{\cdot,\epsilon}$ inverse gamma priors were selected because they represent conjugate priors for the multivariate normal likelihood function in our model. Note that the priors for the calibration parameters θ_i are all uniform and hence non-informative to avoid any bias in estimation.

Using single-component Metropolis-Hastings algorithm, the posterior distributions of calibration parameters, $\boldsymbol{\theta}_1, \boldsymbol{\theta}_2$, and hyperparameters, $\boldsymbol{\Psi}$ were generated after 20,000 iterations with 25% burn-in period and thinning every fifth sample. Implementation and programming was done in Python version 3.7. Figure 4.13 shows the histograms and kernel density estimates of the posterior distributions for the calibration parameters of each model. The posteriors are single-modal and informative, and hence the modes were used as the estimates. Table 4.3 lists for each calibration parameter the lower and upper bounds of search in addition to the final estimate after the Bayesian calibration.

Using the posterior estimates from Table 4.3, we can compute the posterior mean estimates for the whole input variable space using Equation 4.14. Because the input space is 2-dim, we can plot the posterior mean estimates as surfaces, which are functions of laser power and speed (P and v). These surfaces are shown in Figure 4.14(c) and 4.14(f) for the melt pool model and the

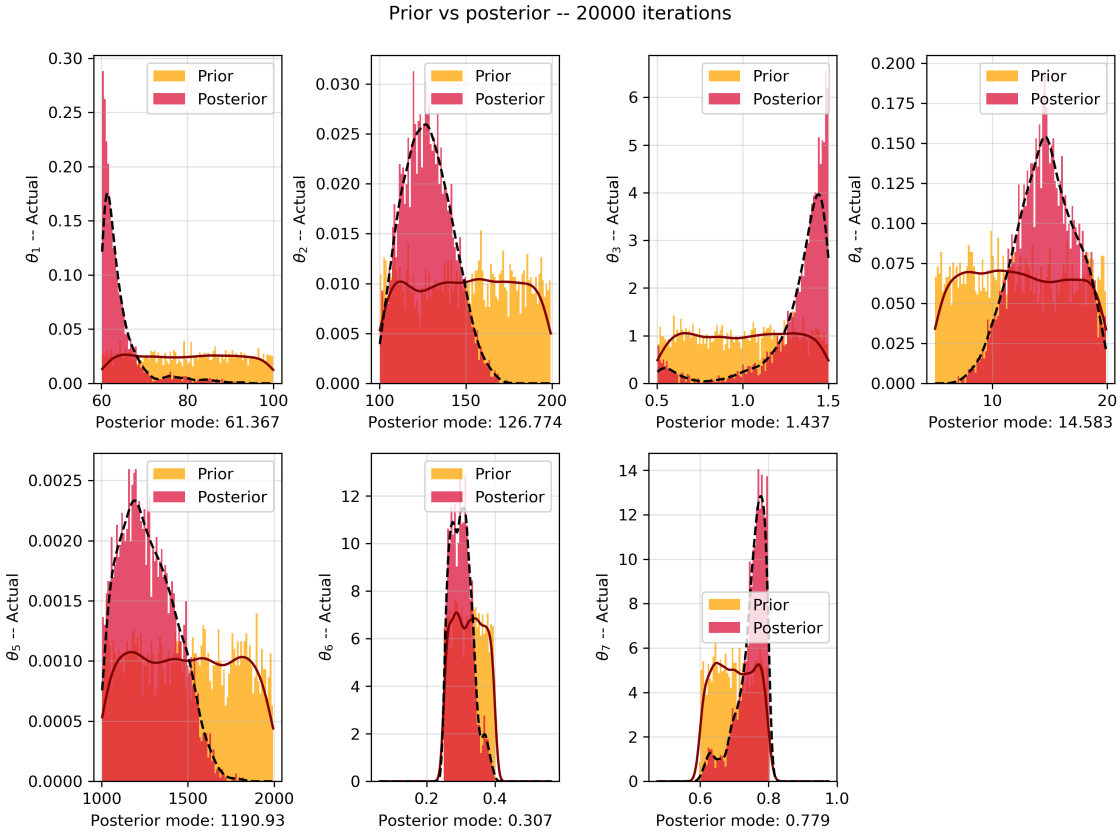

(a)

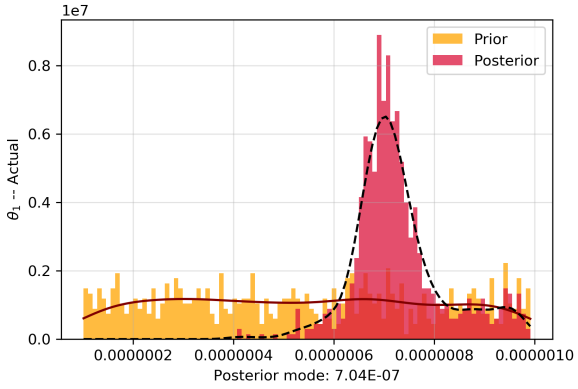

(b)

Figure 4.13: Histograms and kernel density estimates of the posterior distributions for calibration parameters for (a) the melt pool model, and (b) the phase field model

Table 4.3: Posterior estimates of the calibration parameters

Parameter	**Range**	**Estimate**	**Unit**
M_1 **parameters**, $\boldsymbol{\theta}_1$			
K_S	[60, 100]	61.4	$[\mathrm{W/mK}]$
K_L	[100, 200]	126.8	$[\mathrm{W/mK}]$
K_{Lz}	[0.5, 2]	1.44	$[\mathrm{W/mK}]$
K_V	[5, 20]	14.6	$[\mathrm{W/mK}]$
K_{Vz}	[1000, 3000]	1190.9	$[\mathrm{W/mK}]$
A_0	[0.25, 0.4]	0.307	[%]
$A_{\max}$	[0.6, 0.8]	0.779	[%]
M_2 **parameters**, $\boldsymbol{\theta}_2$			
σ	$[10^{-7}, 10^{-6}]$	7.04×10^{-7}	$[\mathrm{J/cm^2}]$

phase field model, respectively. Note that these surfaces are the summation of surrogate models $\hat{y}_\cdot(\boldsymbol{x}; \boldsymbol{\theta}^*)$ (shown in 4.14(a),(d)) and the discrepancy functions $\delta_\cdot$ (shown in 4.14(b),(e)). In all of these plots, the experimental data is shown with red dots. It can be seen that the discrepancy functions appropriately correct the emulator outputs and significantly reduce the error.

4.3.5 Discussion

In this section we take a more careful look at the results that were presented in the previous subsection. Generally, we deem to calibrate multiple models for the whole input space, which is defined by the process. For example, the melt pool model in this study is defined over the laser power-speed input parameter space $\mathcal{X}$. The lower and upper bounds for this space $\mathcal{X}$ was chosen according to the process and machine limitations as $\mathcal{X}_{min} = \{80\,\mathrm{W}, 50\,\mathrm{mm/s}\}$, and $\mathcal{X}_{max} = \{250\,\mathrm{W}, 2000\,\mathrm{mm/s}\}$.

The important matter is that the rest of the models in our network, are not necessarily defined over the whole $\mathcal{X}$ domain. The reason is that the physical phenomena that are simulated by different models do not necessarily exist in the whole domain of $\mathcal{X}$. Hence, different models have different *working regions*. Only after fully understanding the working region for each model we can successfully gather experimental data for calibration and uncertainty quantification purposes.

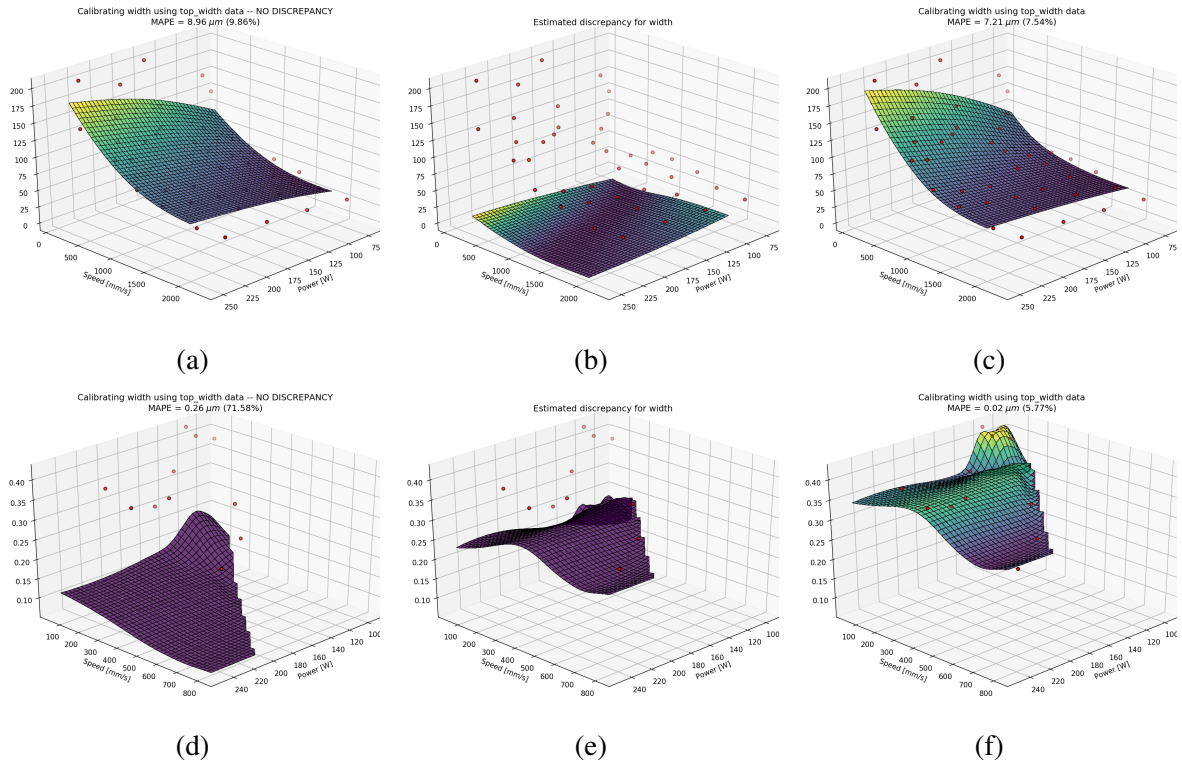

Figure 4.14: Posterior mean estimates for $\hat{y}_{1Q}(\boldsymbol{x};\boldsymbol{\theta}^*)$, δ_{1Q}, and their sum, $y_{1Q}(\boldsymbol{x};\boldsymbol{\theta}^*)$. The experimental observations are shown by the red dots.

In our case study, we noticed that the segregation phenomenon that the phase field model investigates only happen in a specific region of $\mathcal{X}$ that can be characterized by high laser power and low laser speed. Figure 4.15 shows the experimental data for each of the models. Based on these data sets, the working regions are color-coded for each of the models. It can be observed that the density of data points in the green region corresponding to the working region of M_2 is higher. This guarantees that we have enough data points for calibrating M_2.

Figure 4.16 shows the contour maps associate with the prediction error after calibration for melt pool width, $y_{1Q}(\boldsymbol{x};\boldsymbol{\theta}_1^*)$ and PDAS, $y_2(y_{1U}(\boldsymbol{x});\boldsymbol{\theta}_2^*)$. From these maps, we can find out for what areas of the input space the model has too much error perhaps due to missing physics compared to the areas where predictions are satisfactory. Note that in these maps we have not used the discrepancy functions – only the surrogate models with the optimized calibration parameters are used for prediction. Looking at Figure 4.16(a), we realize that the melt pool model has acceptable

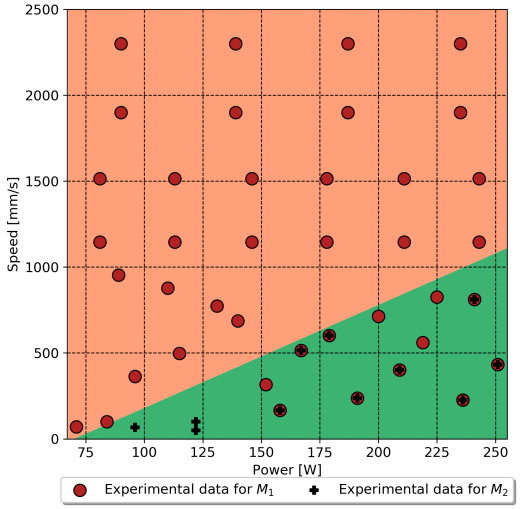

Figure 4.15: Experimental data grid

performance except for high laser power and low speed the model. This region corresponds to the so-called keyholing heat transfer mode. The performance of the model for other areas of the input space is uniformly satisfactory and the error is low. For the phase field model; however, the situation is different. We notice that the error is correlated with the laser speed: at low laser speeds error is high, whereas at high laser speeds the error is decreased. The value of discrepancy function is evident from these error maps, because after adding the discrepancy term final predictions significantly improve.

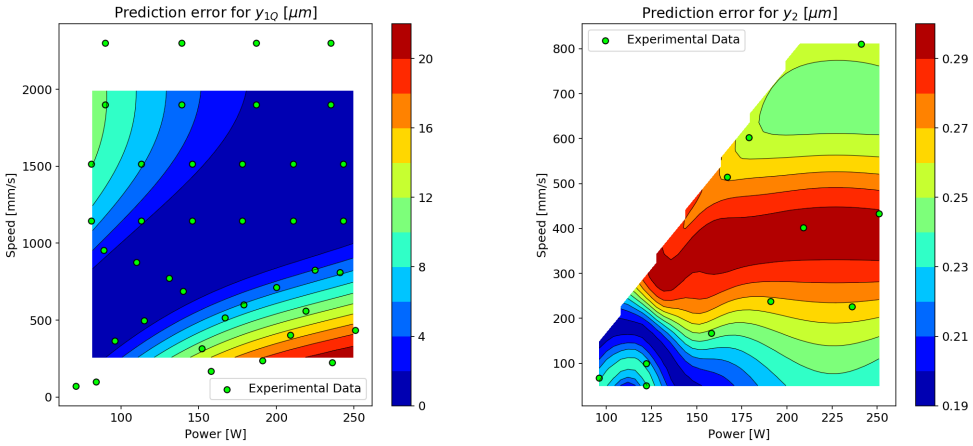

(a) (b)

Figure 4.16: Contour plots of the prediction error after calibration for (a) $y_{1Q}(\boldsymbol{x}; \boldsymbol{\theta_1^*})$ and (b) $y_2(y_{1U}(\boldsymbol{x}); \boldsymbol{\theta_2^*})$

5. SUMMARY

5.1 Contributions of the Dissertation

In this Chapter we summarize the contributions of each part of the Dissertation.

5.1.1 Contributions of Process Monitoring

In Chapter 2, we developed a novel anomaly detection framework for metal laser powder bed fusion additive manufacturing processes (L-PBF AM). The proposed framework detects process deviations through thermal signatures captured using thermal imaging of melt pools during fabrication, where the melt pool represents the interface between the laser beam and metallic powder being processed. These monitored thermal signatures are analyzed through a step-by-step procedure whose building blocks include image segmentation, clustering, spatial statistics, and classification techniques.

The key contributions of the process monitoring work are summarized as follows. First, we address an important gap in the literature on process monitoring and control in metal-based AM processes. More specifically, most of the existing works focus on developing sensors and hardware to enable in-situ process monitoring. However, very few works provide data analysis frameworks to utilize the data acquired from process monitoring for detecting process anomalies. Second, our data-driven approach is guided by process physics through accounting for spatial dependence among successive melt pools at the laser-powder interface in the spatial SIZER used to analyze the data.

Validation experiments indicate that the propsoed framework is capable of detecting process anomalies through experiments conducted on a commercial L-PBF AM system instrumented with a dual-wavelength imaging pyrometer for thermal process monitoring. The current work thus represents an important foundation towards enabling layer-wise quality control in metal AM, which has been identified as an important technological need in most recently published research roadmaps.

5.1.2 Contributions of Uncertainty Quantification

In Chapter 3 we developed an efficient procedure for conducting formal calibration (also known as inverse UQ analysis) of computational materials models. In addition to providing one of the first efforts to systematically perform UQ analysis for ICME purposes, we also present a versatile multivariate statistical framework to perform such analysis in the case of models with multiple QoI's, in contrast to many previous research efforts that typically focus on a univariate scalar QoI. The proposed framework involves a two-step procedure that starts with constructing a computationally efficient multivariate Gaussian Process-based surrogate model that can be used in lieu of the original expensive computational model. The surrogate model can then be used to generate sufficiently large numbers of simulations needed to conduct calibration through a synthesis with experimental measurements.

We implemented the proposed multivariate statistical framework to calibrate a finite element based thermal model for LPBF metal additive manufacturing. The model predicts the thermal history and melt pool geometry during fabrication, and can potentially become one of the core elements of an ICME platform for the LPBF process. Our results indicate that the multivariate surrogate model is capable of adequately approximating the original FE based thermal model to a good degree of accuracy. Furthermore, predictions made using the calibrated model showed good agreement with experimental measurements conducted in a case study on fabricating single tracks of Ti-6Al-4V using a commercial LPBF system instrumented with in-situ temperature monitoring capability.

In Chapter 4 we presented an approach to calibrate a system of models with unobservable variables, when the models are connected in a hierarchical manner. To handle the relationships between the models, the notion of Bayesian network (BN) was used. BN is a probabilistic graphical tool that conveniently allows modeling the relationships between variables of each model using conditional probability distributions. BN also allows any available experimental data at any level (upstream or downstream) to be incorporated into the analysis. Once the data are added to the network, we can update our knowledge about the uncertain parameters, i.e. calibration parameters.

When the network of models include variables that are 'unobservable', which means that experimental observations are not available for all of the models. The reason for this lack of experimental data can be technological limitations or due high costs of experiments. To address this problem, we introduced an auxiliary variable to account for the lack-of-data of the models with unobservable output. Using a Bayesian updating scheme, we estimated the unknown parameters and hyper-parameters so that the desired QoI of the process is predicted with high accuracy.

It is worthy to emphasize another important feature of BNs, which is the compatibility with GP surrogate models. In practice, whenever the actual simulation models are computationally expensive, they can be replaced with the fast GP surrogate models.

Similar to Chapter 3, in order to evaluate the performance of the proposed method, a case study of two hierarchical simulation models used for LPBF was conducted. The first model was an improved version of the thermal model to predict melt pool geometry and temperature. The second model – which used part of the first model output as input – was a phase field model to study the sub-grain structure of the fabricated alloy, in particular the primary dendrite arm spacing (PDAS). The unobservable variable in this network was the temperature gradients that are both outputs of the first model and inputs for the second model. We demonstrated how our framework can be used for calibrating such a network of simulation model by fabricating single tracks of NiNb alloy using a commercial LPBF system.

Another important contribution of our UQ work is the ability to analyze the model discrepancy after calibration. Knowing how severe the model discrepancy is for different inputs, we know for what purposes the models are useful and reliable and vice versa, i.e. when not to rely on the model predictions without enough experimental validation. In our case study of NiNb single tracks, for example, we realized how accurate each model is performing after analyzing a heat map of the discrepancy function. For the first model (the thermal melt pool model), we noted that when operating at high powers and low laser scan speeds – which corresponds to the keyhole heat transfer mode – we will have high prediction errors. For the second model, we noticed a slight increase in the prediction error with higher laser speeds. Additionally, the error map contour lines

were mostly horizontal signaling independence of the model error from laser power.

5.2 Future work

Some directions for future research in process monitoring for LPBF include developing efficient methods for running the spatial SIZER to enable analyzing parts with large cross sectional areas. Currently, the framework was only validated for a specific type of defects (namely, cavities). Metal AM processes are prone to other types of defects such as lack of fusion, delamination, and powder coating problems. Extending the framework to account for other types of defects is an important direction for future research. Finally, the proposed framework focuses on detecting process anomalies, which should be subsequently integrated with feedback control in order to mitigate or minimize defects.

In the area of UQ for LPBF, the current work represents a foundation for numerous future investigations. First, more case studies can be conducted to order to accomplish a complete multi-model ICME platform for laser-based AM. In other words, upgrading the system from two models to a network with many models can be a research challenge that must be addressed. Additionally, more validation experiments with other measurement instruments can be carried out to achieve better accuracy or observing the responses that are currently considered observable.

Another area for future research is conducting UQ for LPBF models when the output has a specific condition. For example, calibration of ICME simulation models with high-dimensional output (e.g. fully explicit microstructure simulations) will be very useful but has not been conducted yet. Another example can be models with binary or categorical response, e.g. when a solidification model predicts if the microstructure would be planar, cellular, or equiaxed.

Note that utilizing the notion of Bayesian networks limits us to hierarchical network; however, many ICME frameworks include models with feedback response. This challenge needs to be addressed with more comprehensive sampling techniques that allow system-level evaluations.

REFERENCES

[1] K. Karayagiz, A. Elwany, G. Tapia, B. Franco, L. Johnson, J. Ma, I. Karaman, and R. Arroyave, "Numerical and experimental analysis of heat distribution in the laser powder bed fusion of ti-6 al-4 v," *IISE Transactions*, no. just-accepted, pp. 1–44, 2018.

[2] "Standard terminology for additive manufacturing technologies," ASTM International, West Conshohocken, PA, Standard, 2012.

[3] G. Tapia and A. Elwany, "A review on process monitoring and control in metal-based additive manufacturing," *Journal of Manufacturing Science and Engineering*, vol. 136, no. 6, p. 060801, 2014.

[4] I. Tolosa, F. Garciandía, F. Zubiri, F. Zapirain, and A. Esnaola, "Study of mechanical properties of aisi 316 stainless steel processed by "selective laser melting", following different manufacturing strategies," *The International Journal of Advanced Manufacturing Technology*, vol. 51, no. 5, pp. 639–647, 2010.

[5] M. Garibaldi, I. Ashcroft, M. Simonelli, and R. Hague, "Metallurgy of high-silicon steel parts produced using selective laser melting," *Acta Materialia*, vol. 110, pp. 207–216, 2016.

[6] M. Mahmoudi, A. Elwany, A. Yadollahi, S. M. Thompson, L. Bian, and N. Shamsaei, "Mechanical properties and microstructural characterization of selective laser melted 17-4 ph stainless steel," *Rapid Prototyping Journal*, vol. 23, no. 2, pp. 280–294, 2017.

[7] L. Facchini, N. Vicente, I. Lonardelli, E. Magalini, P. Robotti, and A. Molinari, "Metastable austenite in 17–4 precipitation-hardening stainless steel produced by selective laser melting," *Advanced Engineering Materials*, vol. 12, no. 3, pp. 184–188, 2010.

[8] M. Masoomi, N. Shamsaei, R. A. Winholtz, J. Milner, T. Gnäupel-Herold, A. Elwany, M. Mahmoudi, and S. M. Thompson, "Residual stress measurements via neutron diffraction of additive manufactured stainless steel 17-4 ph," *Data in Brief*, 2017.

[9] A. Yadollahi, N. Shamsaei, S. M. Thompson, A. Elwany, L. Bian, and M. Mahmoudi, "Fatigue behavior of selective laser melted 17-4 ph stainless steel," in *Proceedings of 26th*

International Solid Freeform Fabrication Symposium, Austin, TX, 2015.

[10] S. Li, H. Hassanin, M. M. Attallah, N. J. Adkins, and K. Essa, "The development of tini-based negative poisson's ratio structure using selective laser melting," *Acta Materialia*, vol. 105, pp. 75–83, 2016.

[11] L. Murr, S. Quinones, S. Gaytan, M. Lopez, A. Rodela, E. Martinez, D. Hernandez, E. Martinez, F. Medina, and R. Wicker, "Microstructure and mechanical behavior of ti–6al–4v produced by rapid-layer manufacturing, for biomedical applications," *Journal of the mechanical behavior of biomedical materials*, vol. 2, no. 1, pp. 20–32, 2009.

[12] A. El-Desouky, M. Carter, M. Mahmoudi, A. Elwany, and S. LeBlanc, "Influences of energy density on microstructure and consolidation of selective laser melted bismuth telluride thermoelectric powder," *Journal of Manufacturing Processes*, vol. 25, pp. 411–417, 2017.

[13] Q. Jia and D. Gu, "Selective laser melting additive manufacturing of inconel 718 superalloy parts: Densification, microstructure and properties," *Journal of Alloys and Compounds*, vol. 585, pp. 713–721, 2014.

[14] B. Franco, J. Ma, B. Loveall, G. Tapia, K. Karayagiz, J. Liu, A. Elwany, R. Arroyave, and I. Karaman, "A sensory material approach for reducing variability in additively manufactured metal parts," *Scientific Reports*, vol. 7, 2017.

[15] J. Ma, B. Franco, G. Tapia, K. Karayagiz, L. Johnson, J. Liu, R. Arroyave, I. Karaman, and A. Elwany, "Spatial control of functional response in 4d-printed active metallic structures," *Scientific Reports*, vol. 7, 2017.

[16] G. Tapia, L. Johnson, B. Franco, K. Karayagiz, J. Ma, R. Arroyave, I. Karaman, and A. Elwany, "Bayesian calibration and uncertainty quantification for a physics-based precipitation model of nickel–titanium shape-memory alloys," *Journal of Manufacturing Science and Engineering*, vol. 139, no. 7, p. 071002, 2017.

[17] M. Elahinia, N. S. Moghaddam, M. T. Andani, A. Amerinatanzi, B. A. Bimber, and R. F. Hamilton, "Fabrication of niti through additive manufacturing: A review," *Progress in Materials Science*, vol. 83, pp. 630–663, 2016.

[18] T. Bormann, R. Schumacher, B. Müller, M. Mertmann, and M. de Wild, "Tailoring selective laser melting process parameters for niti implants," *Journal of Materials Engineering and Performance*, vol. 21, no. 12, pp. 2519–2524, 2012.

[19] C. Haberland, M. Elahinia, J. M. Walker, H. Meier, and J. Frenzel, "On the development of high quality niti shape memory and pseudoelastic parts by additive manufacturing," *Smart Materials and Structures*, vol. 23, no. 10, p. 104002, 2014.

[20] J. M. Walker, C. Haberland, M. Taheri Andani, H. E. Karaca, D. Dean, and M. Elahinia, "Process development and characterization of additively manufactured nickel–titanium shape memory parts," *Journal of Intelligent Material Systems and Structures*, vol. 27, no. 19, pp. 2653–2660, 2016.

[21] J. Parthasarathy, B. Starly, and S. Raman, "A design for the additive manufacture of functionally graded porous structures with tailored mechanical properties for biomedical applications," *Journal of Manufacturing Processes*, vol. 13, no. 2, pp. 160–170, 2011.

[22] P. Muller, P. Mognol, and J.-Y. Hascoet, "Modeling and control of a direct laser powder deposition process for functionally graded materials (fgm) parts manufacturing," *journal of materials processing technology*, vol. 213, no. 5, pp. 685–692, 2013.

[23] J. Hunt, F. Derguti, and I. Todd, "Selection of steels suitable for additive layer manufacturing," *Ironmaking & Steelmaking*, vol. 41, no. 4, pp. 254–256, 2014.

[24] C. Selcuk, "Laser metal deposition for powder metallurgy parts," *Powder Metallurgy*, vol. 54, no. 2, pp. 94–99, 2011.

[25] K. Kempen, L. Thijs, B. Vrancken, S. Buls, J. Van Humbeeck, and J. Kruth, "Producing crack-free, high density m2 hss parts by selective laser melting: pre-heating the baseplate," in *Proceedings of the 24th international solid freeform fabrication symposium. Laboratory for freeform fabrication, Austin, TX*, 2013, pp. 131–139.

[26] W. J. Sames, F. List, S. Pannala, R. R. Dehoff, and S. S. Babu, "The metallurgy and processing science of metal additive manufacturing," *International Materials Reviews*, vol. 61, no. 5, pp. 315–360, 2016.

[27] H. Gu, H. Gong, D. Pal, K. Rafi, T. Starr, and B. Stucker, "Influences of energy density on porosity and microstructure of selective laser melted 17-4ph stainless steel," in *2013 Solid Freeform Fabrication Symposium*, 2013, p. 474.

[28] S. Kleszczynski, J. Zur Jacobsmühlen, J. Sehrt, and G. Witt, "Error detection in laser beam melting systems by high resolution imaging," in *Proceedings of the Twenty Third Annual International Solid Freeform Fabrication Symposium*, 2012.

[29] U. S. Bertoli, A. J. Wolfer, M. J. Matthews, J.-P. R. Delplanque, and J. M. Schoenung, "On the limitations of volumetric energy density as a design parameter for selective laser melting," *Materials & Design*, vol. 113, pp. 331–340, 2017.

[30] M. Averyanova, E. Cicala, P. Bertrand, and D. Grevey, "Experimental design approach to optimize selective laser melting of martensitic 17-4 ph powder: part i–single laser tracks and first layer," *Rapid Prototyping Journal*, vol. 18, no. 1, pp. 28–37, 2012.

[31] W. E. King, H. D. Barth, V. M. Castillo, G. F. Gallegos, J. W. Gibbs, D. E. Hahn, C. Kamath, and A. M. Rubenchik, "Observation of keyhole-mode laser melting in laser powder-bed fusion additive manufacturing," *Journal of Materials Processing Technology*, vol. 214, no. 12, pp. 2915–2925, 2014.

[32] G. Tapia, S. Khairallah, M. Matthews, W. E. King, and A. Elwany, "Gaussian process-based surrogate modeling framework for process planning in laser powder-bed fusion additive manufacturing of 316l stainless steel," *The International Journal of Advanced Manufacturing Technology*, pp. 1–13, 2017.

[33] S. A. Khairallah, A. T. Anderson, A. Rubenchik, and W. E. King, "Laser powder-bed fusion additive manufacturing: Physics of complex melt flow and formation mechanisms of pores, spatter, and denudation zones," *Acta Materialia*, vol. 108, pp. 36–45, 2016.

[34] M. Megahed, H.-W. Mindt, N. N'Dri, H. Duan, and O. Desmaison, "Metal additive-manufacturing process and residual stress modeling," *Integrating Materials and Manufacturing Innovation*, vol. 5, no. 1, p. 4, 2016.

[35] D. Zhang, Q. Cai, J. Liu, L. Zhang, and R. Li, "Select laser melting of w–ni–fe powders:

simulation and experimental study," *The International Journal of Advanced Manufacturing Technology*, vol. 51, no. 5-8, pp. 649–658, 2010.

[36] M. Masoomi, S. M. Thompson, and N. Shamsaei, "Laser powder bed fusion of ti-6al-4v parts: Thermal modeling and mechanical implications," *International Journal of Machine Tools and Manufacture*, vol. 118, pp. 73–90, 2017.

[37] A. O'Hagan, "Bayesian analysis of computer code outputs: a tutorial," *Reliability Engineering & System Safety*, vol. 91, no. 10, pp. 1290–1300, 2006.

[38] National Research Council, *Integrated computational materials engineering: a transformational discipline for improved competitiveness and national security*., National Academies Press, 2008.

[39] A. Chernatynskiy, S. R. Phillpot, and R. LeSar, "Uncertainty quantification in multiscale simulation of materials: A prospective," *Annual Review of Materials Research*, vol. 43, pp. 157–182, 2013.

[40] J. H. Panchal, S. R. Kalidindi, and D. L. McDowell, "Key computational modeling issues in integrated computational materials engineering," *Computer-Aided Design*, vol. 45, no. 1, pp. 4–25, 2013.

[41] D. L. McDowell and S. R. Kalidindi, "The materials innovation ecosystem: a key enabler for the materials genome initiative," *MRS Bulletin*, vol. 41, no. 4, pp. 326–337, 2016.

[42] J. M. Murphy, D. M. Sexton, D. N. Barnett, G. S. Jones *et al.*, "Quantification of modelling uncertainties in a large ensemble of climate change simulations," *Nature*, vol. 430, no. 7001, p. 768, 2004.

[43] J. A. Witteveen, S. Sarkar, and H. Bijl, "Modeling physical uncertainties in dynamic stall induced fluid–structure interaction of turbine blades using arbitrary polynomial chaos," *Computers & structures*, vol. 85, no. 11, pp. 866–878, 2007.

[44] M. Van Oijen, J. Rougier, and R. Smith, "Bayesian calibration of process-based forest models: bridging the gap between models and data," *Tree Physiology*, vol. 25, no. 7, pp. 915–927, 2005.

[45] M. N. Avramova and K. N. Ivanov, "Verification, validation and uncertainty quantification in multi-physics modeling for nuclear reactor design and safety analysis," *Progress in Nuclear Energy*, vol. 52, no. 7, pp. 601–614, 2010.

[46] L. Kilian and T. Zha, "Quantifying the uncertainty about the half-life of deviations from ppp," *Journal of Applied Econometrics*, vol. 17, no. 2, pp. 107–125, 2002.

[47] M. A. Scales, "A roadmapping study for connecting materials models and simulations across length and time scales (the minerals, metals and materials society, 2015)," 2016.

[48] D. Howe, B. Goodlet, J. Weaver, and G. Spanos, "Insights from the 3rd world congress on integrated computational materials engineering," *JOM*, vol. 68, no. 5, pp. 1378–1384, 2016.

[49] T. G. Trucano, L. P. Swiler, T. Igusa, W. L. Oberkampf, and M. Pilch, "Calibration, validation, and sensitivity analysis: What's what," *Reliability Engineering & System Safety*, vol. 91, no. 10, pp. 1331–1357, 2006.

[50] J. Sacks, W. J. Welch, T. J. Mitchell, and H. P. Wynn, "Design and analysis of computer experiments," *Statistical science*, pp. 409–423, 1989.

[51] R. Haylock and A. O'Hagan, "On inference for outputs of computationally expensive algorithms with uncertainty on the inputs," *Bayesian statistics*, vol. 5, pp. 629–637, 1996.

[52] M. C. Kennedy and A. O'Hagan, "Bayesian calibration of computer models," *Journal of the Royal Statistical Society: Series B (Statistical Methodology)*, vol. 63, no. 3, pp. 425–464, 2001.

[53] J. Oakley and A. O'hagan, "Bayesian inference for the uncertainty distribution of computer model outputs," *Biometrika*, vol. 89, no. 4, pp. 769–784, 2002.

[54] C. E. Rasmussen and C. K. I. Williams, *Gaussian Processes for Machine Learning*., Cambridge, MA: The MIT Press, 2006.

[55] G. Tapia, A. Elwany, and H. Sang, "Prediction of porosity in metal-based additive manufacturing using spatial gaussian process models," *Additive Manufacturing*, vol. 12, pp. 282–290, 2016.

[56] J. Friedman, T. Hastie, and R. Tibshirani, *The elements of statistical learning*., Berlin:

Springer, 2001.

[57] R. Mao, H. Zhu, L. Zhang, and A. Chen, "A new method to assist small data set neural network learning," in *Intelligent Systems Design and Applications, 2006. ISDA'06. Sixth International Conference on*, vol. 1., IEEE, 2006, pp. 17–22.

[58] M. Mahmoudi, A. A. Ezzat, and A. Elwany, "Layerwise anomaly detection in laser powder-bed fusion metal additive manufacturing," *Journal of Manufacturing Science and Engineering*, vol. 141, no. 3, p. 031002, 2019.

[59] M. Mani, S. Feng, B. Lane, A. Donmez, S. Moylan, and R. Fesperman, *Measurement science needs for real-time control of additive manufacturing powder bed fusion processes.*, US Department of Commerce, National Institute of Standards and Technology, 2015.

[60] M. Grasso and B. M. Colosimo, "Process defects and in situ monitoring methods in metal powder bed fusion: a review," *Measurement Science and Technology*, vol. 28, no. 4, p. 044005, 2017.

[61] S. Kerwien, S. Collings, F. Liou, and M. Bytnar, "Measurement science roadmap for metal-based additive manufacturing," *NIST*, 2013.

[62] P. K. Rao, J. P. Liu, D. Roberson, Z. J. Kong, and C. Williams, "Online real-time quality monitoring in additive manufacturing processes using heterogeneous sensors," *Journal of Manufacturing Science and Engineering*, vol. 137, no. 6, p. 061007, 2015.

[63] C. Kousiatza and D. Karalekas, "In-situ monitoring of strain and temperature distributions during fused deposition modeling process," *Materials & Design*, vol. 97, pp. 400–406, 2016.

[64] K. Bastani, P. K. Rao, and Z. Kong, "An online sparse estimation-based classification approach for real-time monitoring in advanced manufacturing processes from heterogeneous sensor data," *IIE Transactions*, vol. 48, no. 7, pp. 579–598, 2016.

[65] M. Khanzadeh, S. Chowdhury, L. Bian, and M. A. Tschopp, "A methodology for predicting porosity from thermal imaging of melt pools in additive manufacturing thin wall sections," in *ASME 2017 12th International Manufacturing Science and Engineering Conference collocated with the JSME/ASME 2017 6th International Conference on Materials and Process-*

ing., American Society of Mechanical Engineers, 2017, pp. V002T01A044–V002T01A044.

[66] M. Abdelrahman, E. W. Reutzel, A. R. Nassar, and T. L. Starr, "Flaw detection in powder bed fusion using optical imaging," *Additive Manufacturing*, vol. 15, pp. 1–11, 2017.

[67] M. Aminzadeh and T. Kurfess, "Vision-based inspection system for dimensional accuracy in powder-bed additive manufacturing," in *ASME 2016 11th International Manufacturing Science and Engineering Conference*., American Society of Mechanical Engineers, 2016, pp. V002T04A042–V002T04A042.

[68] H. Gong, K. Rafi, H. Gu, T. Starr, and B. Stucker, "Analysis of defect generation in ti–6al–4v parts made using powder bed fusion additive manufacturing processes," *Additive Manufacturing*, vol. 1, pp. 87–98, 2014.

[69] H. Gong, K. Rafi, H. Gu, G. J. Ram, T. Starr, and B. Stucker, "Influence of defects on mechanical properties of ti–6al–4v components produced by selective laser melting and electron beam melting," *Materials & Design*, vol. 86, pp. 545–554, 2015.

[70] T. G. Spears and S. A. Gold, "In-process sensing in selective laser melting (slm) additive manufacturing," *Integrating Materials and Manufacturing Innovation*, vol. 5, no. 1, p. 2, 2016.

[71] S. K. Everton, M. Hirsch, P. Stravroulakis, R. K. Leach, and A. T. Clare, "Review of in-situ process monitoring and in-situ metrology for metal additive manufacturing," *Materials & Design*, vol. 95, pp. 431–445, 2016.

[72] J.-P. Kruth, P. Mercelis, J. Van Vaerenbergh, and T. Craeghs, "Feedback control of selective laser melting," in *Proceedings of the 3rd international conference on advanced research in virtual and rapid prototyping*, 2007, pp. 521–527.

[73] T. Craeghs, F. Bechmann, S. Berumen, and J.-P. Kruth, "Feedback control of layerwise laser melting using optical sensors," *Physics Procedia*, vol. 5, pp. 505–514, 2010.

[74] S. Berumen, F. Bechmann, S. Lindner, J.-P. Kruth, and T. Craeghs, "Quality control of laser- and powder bed-based additive manufacturing (am) technologies," *Physics procedia*, vol. 5, pp. 617–622, 2010.

[75] T. Craeghs, S. Clijsters, J.-P. Kruth, F. Bechmann, and M.-C. Ebert, "Detection of process failures in layerwise laser melting with optical process monitoring," *Physics Procedia*, vol. 39, pp. 753–759, 2012.

[76] S. Clijsters, T. Craeghs, S. Buls, K. Kempen, and J.-P. Kruth, "In situ quality control of the selective laser melting process using a high-speed, real-time melt pool monitoring system," *The International Journal of Advanced Manufacturing Technology*, vol. 75, no. 5-8, pp. 1089–1101, 2014.

[77] H. Krauss, C. Eschey, and M. Zaeh, "Thermography for monitoring the selective laser melting process," in *Proceedings of the Solid Freeform Fabrication Symposium*, 2012.

[78] H. Krauss, T. Zeugner, and M. F. Zaeh, "Layerwise monitoring of the selective laser melting process by thermography," *Physics Procedia*, vol. 56, pp. 64–71, 2014.

[79] Y. Chivel and I. Smurov, "On-line temperature monitoring in selective laser sintering/melting," *Physics Procedia*, vol. 5, pp. 515–521, 2010.

[80] M. Pavlov, M. Doubenskaia, and I. Smurov, "Pyrometric analysis of thermal processes in slm technology," *Physics Procedia*, vol. 5, pp. 523–531, 2010.

[81] M. Doubenskaia, M. Pavlov, S. Grigoriev, E. Tikhonova, and I. Smurov, "Comprehensive optical monitoring of selective laser melting." *Journal of Laser Micro/Nanoengineering*, vol. 7, no. 3, 2012.

[82] Y. Chivel, "Optical in-process temperature monitoring of selective laser melting," *Physics Procedia*, vol. 41, pp. 904–910, 2013.

[83] M. Doubenskaia, S. Grigoriev, I. Zhirnov, and I. Smurov, "Parametric analysis of slm using comprehensive optical monitoring," *Rapid Prototyping Journal*, vol. 22, no. 1, pp. 40–50, 2016.

[84] M. Grasso, A. Demir, B. Previtali, and B. Colosimo, "In situ monitoring of selective laser melting of zinc powder via infrared imaging of the process plume," *Robotics and Computer-Integrated Manufacturing*, vol. 49, pp. 229–239, 2018.

[85] EOS. (2018) Eostate monitoring suite – real-time monitoring for industrial 3d printing. [On-

line]. Available: https://www.eos.info/software/monitoring-software

[86] Renishaw. (2018) Infiniam spectral. [Online]. Available: http://www.renishaw.com/en/infiniam-spectral--42310

[87] M. Grasso, V. Laguzza, Q. Semeraro, and B. M. Colosimo, "In-process monitoring of selective laser melting: spatial detection of defects via image data analysis," *Journal of Manufacturing Science and Engineering*, vol. 139, no. 5, p. 051001, 2017.

[88] M. Khanzadeh, P. Rao, R. Jafari-Marandi, B. K. Smith, M. A. Tschopp, and L. Bian, "Quantifying geometric accuracy with unsupervised machine learning: Using self-organizing map on fused filament fabrication additive manufacturing parts," *Journal of Manufacturing Science and Engineering*, vol. 140, no. 3, p. 031011, 2018.

[89] M. Khanzadeh, S. Chowdhury, M. A. Tschopp, H. R. Doude, M. Marufuzzaman, and L. Bian, "In-situ monitoring of melt pool images for porosity prediction in directed energy deposition processes," *IISE Transactions*, no. just-accepted, 2017.

[90] A. Vaughan, M. Jun, and C. Park, "Statistical inference and visualization in scale-space for spatially dependent images," *Journal of the Korean Statistical Society*, vol. 41, no. 1, pp. 115–135, 2012.

[91] M. Fuentes, "A high frequency kriging approach for non-stationary environmental processes," *Environmetrics*, vol. 12, no. 5, pp. 469–483, 2001.

[92] L. Michalski, K. Eckersdorf, and J. McGhee, *Temperature measurement*., Wiley, 1991.

[93] B. Müller and U. Renz, "Development of a fast fiber-optic two-color pyrometer for the temperature measurement of surfaces with varying emissivities," *Review of scientific instruments*, vol. 72, no. 8, pp. 3366–3374, 2001.

[94] A. Hijazi, S. Sachidanandan, R. Singh, and V. Madhavan, "A calibrated dual-wavelength infrared thermometry approach with non-greybody compensation for machining temperature measurements," *Measurement Science and Technology*, vol. 22, no. 2, p. 025106, 2011.

[95] J. C. Heigel, B. M. Lane, M. Ljubicic, N. Ivezic, B. Kulvatunyou, S. Nieman, N. Anicic, Z. Marjanovic, A. Brodsky, M. Krishnamoorthy *et al.*, "Measurement of the melt pool length

during single scan tracks in a commercial laser powder bed fusion process," *Proc. MSEC, Los Angeles, CA*, pp. 575–591, 2017.

[96] F. Verhaeghe, T. Craeghs, J. Heulens, and L. Pandelaers, "A pragmatic model for selective laser melting with evaporation," *Acta Materialia*, vol. 57, no. 20, pp. 6006–6012, 2009.

[97] L.-E. Loh, C.-K. Chua, W.-Y. Yeong, J. Song, M. Mapar, S.-L. Sing, Z.-H. Liu, and D.-Q. Zhang, "Numerical investigation and an effective modelling on the selective laser melting (slm) process with aluminium alloy 6061," *International Journal of Heat and Mass Transfer*, vol. 80, pp. 288–300, 2015.

[98] A. Masmoudi, R. Bolot, and C. Coddet, "Investigation of the laser–powder–atmosphere interaction zone during the selective laser melting process," *Journal of Materials Processing Technology*, vol. 225, pp. 122–132, 2015.

[99] C. Qiu, C. Panwisawas, M. Ward, H. C. Basoalto, J. W. Brooks, and M. M. Attallah, "On the role of melt flow into the surface structure and porosity development during selective laser melting," *Acta Materialia*, vol. 96, pp. 72–79, 2015.

[100] A. M. Aboutaleb, L. Bian, A. Elwany, N. Shamsaei, S. M. Thompson, and G. Tapia, "Accelerated process optimization for laser-based additive manufacturing by leveraging similar prior studies," *IISE Transactions*, vol. 49, no. 1, pp. 31–44, 2017.

[101] R. C. Gonzalez and R. E. Woods, *Digital image processing*., Prentice hall New Jersey, 2008.

[102] P. Chaudhuri and J. S. Marron, "Sizer for exploration of structures in curves," *Journal of the American Statistical Association*, vol. 94, no. 447, pp. 807–823, 1999.

[103] F. Godtliebsen, J. S. Marron, and P. Chaudhuri, "Statistical significance of features in digital images," *Image and Vision Computing*, vol. 22, no. 13, pp. 1093–1104, 2004.

[104] R. Tarjan, "Depth-first search and linear graph algorithms," *SIAM journal on computing*, vol. 1, no. 2, pp. 146–160, 1972.

[105] S. Suriano, H. Wang, C. Shao, S. J. Hu, and P. Sekhar, "Progressive measurement and monitoring for multi-resolution data in surface manufacturing considering spatial and cross correlations," *IIE Transactions*, vol. 47, no. 10, pp. 1033–1052, 2015.

[106] T. Hastie, R. Tibshirani, and J. Friedman, "The elements of statistical learning: data mining, inference, and prediction 2 edition springer," *New York*, 2009.

[107] T. Toeppel, P. Schumann, M.-C. Ebert, T. Bokkes, K. Funke, M. Werner, F. Zeulner, F. Bechmann, and F. Herzog, "3d analysis in laser beam melting based on real-time process monitoring," in *Mater Sci Technol Conf*, 2016.

[108] C. Elkan, "The foundations of cost-sensitive learning," in *International joint conference on artificial intelligence*, vol. 17, no. 1, 2001, pp. 973–978.

[109] M. Mahmoudi, G. Tapia, K. Karayagiz, B. Franco, J. Ma, R. Arroyave, I. Karaman, and A. Elwany, "Multivariate calibration and experimental validation of a 3d finite element thermal model for laser powder bed fusion metal additive manufacturing," *Integrating Materials and Manufacturing Innovation*, vol. 7, no. 3, pp. 116–135, 2018.

[110] B. Liu and Q. Xu, "Advances on microstructure modeling of solidification process of shape casting," *Tsinghua Science and Technology*, vol. 9, no. 5, pp. 497–505, 2004.

[111] P. Liu and M. T. Lusk, "Parametric links among monte carlo, phase-field, and sharp-interface models of interfacial motion," *Physical Review E*, vol. 66, no. 6, p. 061603, 2002.

[112] E. Holm, D. J. Srolovitz, and J. Cahn, "Microstructural evolution in two-dimensional two-phase polycrystals," *Acta metallurgica et materialia*, vol. 41, no. 4, pp. 1119–1136, 1993.

[113] J. Spittle and S. Brown, "Computer simulation of the effects of alloy variables on the grain structures of castings," *Acta Metallurgica*, vol. 37, no. 7, pp. 1803–1810, 1989.

[114] P. Zhu and R. Smith, "Dynamic simulation of crystal growth by monte carlo method i. model description and kinetics," *Acta metallurgica et materialia*, vol. 40, no. 4, pp. 683–692, 1992.

[115] D. Higdon, J. Gattiker, B. Williams, and M. Rightley, "Computer model calibration using high-dimensional output," *Journal of the American Statistical Association*, vol. 103, no. 482, pp. 570–583, 2008.

[116] R. Paulo, G. García-Donato, and J. Palomo, "Calibration of computer models with multivariate output," *Computational Statistics & Data Analysis*, vol. 56, no. 12, pp. 3959–3974, 2012.

[117] S. Conti and A. O'Hagan, "Bayesian emulation of complex multi-output and dynamic computer models," *Journal of statistical planning and inference*, vol. 140, no. 3, pp. 640–651, 2010.

[118] A. E. Gelfand, P. Diggle, P. Guttorp, and M. Fuentes, *Handbook of Spatial Statistics*., Boca Raton, FL: CRC Press, 2010.

[119] K. Bhat, M. Haran, and M. Goes, "Computer model calibration with multivariate spatial output: A case study," *Frontiers of Statistical Decision Making and Bayesian Analysis*, pp. 168–184, 2010.

[120] G. Casella and R. L. Berger, *Statistical inference*., Duxbury Pacific Grove, CA, 2002, vol. 2.

[121] S. A. Khairallah and A. Anderson, "Mesoscopic simulation model of selective laser melting of stainless steel powder," *Journal of Materials Processing Technology*, vol. 214, no. 11, pp. 2627–2636, 2014.

[122] R. Ganeriwala and T. I. Zohdi, "A coupled discrete element-finite difference model of selective laser sintering," *Granular Matter*, vol. 18, no. 2, p. 21, 2016.

[123] K. Leitz, P. Singer, A. Plankensteiner, B. Tabernig, H. Kestler, and L. Sigl, "Multi-physical simulation of selective laser melting of molybdenum," *Proceedings of Euro PM*, pp. 4–7, 2015.

[124] C. Panwisawas, C. Qiu, M. J. Anderson, Y. Sovani, R. P. Turner, M. M. Attallah, J. W. Brooks, and H. C. Basoalto, "Mesoscale modelling of selective laser melting: Thermal fluid dynamics and microstructural evolution," *Computational Materials Science*, vol. 126, pp. 479–490, 2017.

[125] S. Ly, A. M. Rubenchik, S. A. Khairallah, G. Guss, and M. J. Matthews, "Metal vapor micro-jet controls material redistribution in laser powder bed fusion additive manufacturing," *Scientific Reports*, vol. 7, 2017.

[126] W. Pei, W. Zhengying, C. Zhen, L. Junfeng, Z. Shuzhe, and D. Jun, "Numerical simulation and parametric analysis of selective laser melting process of alsi10mg powder," *Applied Physics A*, vol. 123, no. 8, p. 540, 2017.

[127] M. Matsumoto, M. Shiomi, K. Osakada, and F. Abe, "Finite element analysis of single layer forming on metallic powder bed in rapid prototyping by selective laser processing," *International Journal of Machine Tools and Manufacture*, vol. 42, no. 1, pp. 61–67, 2002.

[128] I. A. Roberts, C. Wang, R. Esterlein, M. Stanford, and D. Mynors, "A three-dimensional finite element analysis of the temperature field during laser melting of metal powders in additive layer manufacturing," *International Journal of Machine Tools and Manufacture*, vol. 49, no. 12, pp. 916–923, 2009.

[129] N. Shen and K. Chou, "Thermal modeling of electron beam additive manufacturing process. powder sintering effects," *ASME Paper No. MSEC2012-7253*, 2012.

[130] A. Hussein, L. Hao, C. Yan, and R. Everson, "Finite element simulation of the temperature and stress fields in single layers built without-support in selective laser melting," *Materials & Design*, vol. 52, pp. 638–647, 2013.

[131] C. Fu and Y. Guo, "3-dimensional finite element modeling of selective laser melting ti-6al-4v alloy," in *25th Annual International Solid Freeform Fabrication Symposium*, 2014.

[132] J. Romano, L. Ladani, and M. Sadowski, "Thermal modeling of laser based additive manufacturing processes within common materials," *Procedia Manufacturing*, vol. 1, pp. 238–250, 2015.

[133] T. Heeling, M. Cloots, and K. Wegener, "Melt pool simulation for the evaluation of process parameters in selective laser melting," *Additive Manufacturing*, vol. 14, pp. 116–125, 2017.

[134] M. Xia, D. Gu, G. Yu, D. Dai, H. Chen, and Q. Shi, "Porosity evolution and its thermodynamic mechanism of randomly packed powder-bed during selective laser melting of inconel 718 alloy," *International Journal of Machine Tools and Manufacture*, vol. 116, pp. 96–106, 2017.

[135] Y. Huang, L. Yang, X. Du, and Y. Yang, "Finite element analysis of thermal behavior of metal powder during selective laser melting," *International Journal of Thermal Sciences*, vol. 104, pp. 146–157, 2016.

[136] K. Dai and L. Shaw, "Thermal and stress modeling of multi-material laser processing," *Acta*

Materialia, vol. 49, no. 20, pp. 4171–4181, 2001.

[137] L. Van Belle, G. Vansteenkiste, and J. C. Boyer, "Comparisons of numerical modelling of the selective laser melting," in *Key Engineering Materials*, vol. 504., Trans Tech Publ, 2012, pp. 1067–1072.

[138] Y. Liu, J. Zhang, and Z. Pang, "Numerical and experimental investigation into the subsequent thermal cycling during selective laser melting of multi-layer 316l stainless steel," *Optics & Laser Technology*, vol. 98, pp. 23–32, 2018.

[139] K. Zeng, D. Pal, and B. Stucker, "A review of thermal analysis methods in laser sintering and selective laser melting," in *Proceedings of Solid Freeform Fabrication Symposium Austin, TX*, 2012, pp. 796–814.

[140] B. Schoinochoritis, D. Chantzis, and K. Salonitis, "Simulation of metallic powder bed additive manufacturing processes with the finite element method: A critical review," *Proceedings of the Institution of Mechanical Engineers, Part B: Journal of Engineering Manufacture*, vol. 231, no. 1, pp. 96–117, 2017.

[141] M. Markl and C. Körner, "Multiscale modeling of powder bed–based additive manufacturing," *Annual Review of Materials Research*, vol. 46, pp. 93–123, 2016.

[142] G. Vastola, G. Zhang, Q. Pei, and Y.-W. Zhang, "Modeling the microstructure evolution during additive manufacturing of ti6al4v: a comparison between electron beam melting and selective laser melting," *JOM*, vol. 68, no. 5, pp. 1370–1375, 2016.

[143] B. Cheng, S. Price, J. Lydon, K. Cooper, and K. Chou, "On process temperature in powder-bed electron beam additive manufacturing: Model development and validation," *Journal of Manufacturing Science and Engineering*, vol. 136, no. 6, p. 061018, 2014.

[144] S. Boluki, M. S. Esfahani, X. Qian, and E. R. Dougherty, "Incorporating biological prior knowledge for bayesian learning via maximal knowledge-driven information priors," *BMC Bioinformatics*, vol. 18, no. 14, pp. 1–1, 2017.

[145] S. Boluki, M. S. Esfahani, X. Qian, and E. R. Dougherty, "Constructing pathway-based priors within a gaussian mixture model for bayesian regression and classification," *IEEE/ACM*

Transactions on Computational Biology and Bioinformatics, vol. PP, no. 99, pp. 1–1, 2017.

[146] J. Romano, L. Ladani, and M. Sadowski, "Laser additive melting and solidification of inconel 718: finite element simulation and experiment," *Jom*, vol. 68, no. 3, pp. 967–977, 2016.

[147] C. Boley, S. Khairallah, and A. Rubenchik, "Calculation of laser absorption by metal powders in additive manufacturing," *Applied optics*, vol. 54, no. 9, pp. 2477–2482, 2015.

[148] A. Rubenchik, S. Wu, S. Mitchell, I. Golosker, M. LeBlanc, and N. Peterson, "Direct measurements of temperature-dependent laser absorptivity of metal powders," *Applied optics*, vol. 54, no. 24, pp. 7230–7233, 2015.

[149] A. Urbina, S. Mahadevan, and T. L. Paez, "A bayes network approach to uncertainty quantification in hierarchically developed computational models," *International Journal for Uncertainty Quantification*, vol. 2, no. 2, 2012.

[150] K. N. Kyzyurova, J. O. Berger, and R. L. Wolpert, "Coupling computer models through linking their statistical emulators," *SIAM/ASA Journal on Uncertainty Quantification*, vol. 6, no. 3, pp. 1151–1171, 2018.

[151] J. B. Nagel and B. Sudret, "A unified framework for multilevel uncertainty quantification in bayesian inverse problems," *Probabilistic Engineering Mechanics*, vol. 43, pp. 68–84, 2016.

[152] E. C. DeCarlo, B. P. Smarslok, and S. Mahadevan, "Segmented bayesian calibration of multidisciplinary models," *AIAA Journal*, pp. 3727–3741, 2016.

[153] S. Ghoreishi and D. Allaire, "Adaptive uncertainty propagation for coupled multidisciplinary systems," *AIAA Journal*, pp. 1–11, 2017.

[154] D. Higdon, C. Nakhleh, J. Gattiker, and B. Williams, "A bayesian calibration approach to the thermal problem," *Computer Methods in Applied Mechanics and Engineering*, vol. 197, no. 29, pp. 2431–2441, 2008.

[155] S. Nannapaneni, S. Mahadevan, and S. Rachuri, "Performance evaluation of a manufacturing process under uncertainty using bayesian networks," *Journal of Cleaner Production*, vol. 113, pp. 947–959, 2016.

[156] T. D. Nielsen and F. V. Jensen, *Bayesian networks and decision graphs*., Springer Science & Business Media, 2009.

[157] W. King, A. Anderson, R. Ferencz, N. Hodge, C. Kamath, S. Khairallah, and A. Rubenchik, "Laser powder bed fusion additive manufacturing of metals; physics, computational, and materials challenges," *Applied Physics Reviews*, vol. 2, no. 4, p. 041304, 2015.

[158] K. Karayagiz, A. Elwany, G. Tapia, B. Franco, L. Johnson, J. Ma, I. Karaman, and R. Arroyave, "Numerical and experimental analysis of heat distribution in the laser powder bed fusion of ti-6al-4v," *IISE Transactions*, vol. 51, no. 2, pp. 136–152, 2019.

[159] Z. Hu and S. Mahadevan, "Uncertainty quantification in prediction of material properties during additive manufacturing," *Scripta Materialia*, vol. 135, pp. 135–140, 2017.

[160] I. Steinbach, L. Zhang, and M. Plapp, "Phase-field model with finite interface dissipation," *Acta Materialia*, vol. 60, no. 6-7, pp. 2689–2701, 2012.

[161] L. Zhang and I. Steinbach, "Phase-field model with finite interface dissipation: Extension to multi-component multi-phase alloys," *Acta Materialia*, vol. 60, no. 6-7, pp. 2702–2710, 2012.

[162] G. Stevens, S. Atamturktur, R. Lebensohn, and G. Kaschner, "Experiment-based validation and uncertainty quantification of coupled multi-scale plasticity models," *Multidiscipline Modeling in Materials and Structures*, vol. 12, no. 1, pp. 151–176, 2016.

[163] K. N. Kyzyurova, "On uncertainty quantification for systems of computer models," Ph.D. dissertation, Duke University, 2017.

[164] R. H. Byrd, P. Lu, J. Nocedal, and C. Zhu, "A limited memory algorithm for bound constrained optimization," *SIAM Journal on Scientific Computing*, vol. 16, no. 5, pp. 1190–1208, 1995.

[165] W. Rasband, "Imagej. us national institutes of health, bethesda, md, usa," 1997.

[166] C. Li and S. Mahadevan, "Sensitivity analysis of a bayesian network," *ASCE-ASME Journal of Risk and Uncertainty in Engineering Systems, Part B: Mechanical Engineering*, vol. 4, no. 1, p. 011003, 2018.

[167] F. V. Jensen, “Bayesian networks and decision graphs. series for statistics for engineering and information science,” 2001.

[168] B. Liang and S. Mahadevan, “Error and uncertainty quantification and sensitivity analysis in mechanics computational models,” *International Journal for Uncertainty Quantification*, vol. 1, no. 2, 2011.

APPENDIX A

BAYESIAN NETWORKS

Formally, a BN is a directed acyclic graph that represents the joint probability distribution of the random variables. These random variables represent the uncertain QoI's in our problem setting. When the BN has been constructed, computing the distribution of a downstream node based on the given observation of an upstream node, i.e., forward propagation of uncertainty, and estimating the posterior distribution of an upstream node at the given observation of a downstream node, i.e., backward inference can be pursued [166]. In addition, BN allows utilizing fast surrogate models to speed up the analysis when the computer models are computationally expensive to run.

At the heart of a Bayes network is establishing a relationship between the variables involved in the models. A Bayesian network consists of the following [167]

1. A set of variables (nodes) and a set of directed edges (arcs) between variables
2. The variables together with the directed edges form a directed acyclic graph (DAG).
3. To each variable B with parents $A_1, ..., A_n$, there is an associated conditional probability $P(B|A_1, ..., A_n)$

The entire network can be represented using a joint probability density function which is given by the general expression below:

$$P(\mathcal{U}) = \prod_i P(A_i|\text{parent}(A_i)) \tag{A.1}$$

An example BN is show in Fig. A.1. Using the rules explained before we can write the joint probability density function as follows.

$$P(\mathcal{U}) = P(A)P(B)P(C|A,B)P(E|C)P(D|C)P(F|E)P(G|D,E,F) \tag{A.2}$$

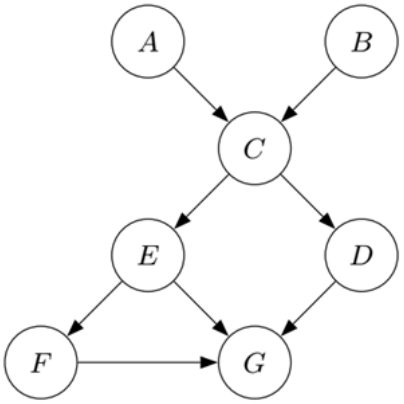

Figure A.1: An example of a Bayesian network

Now consider the basic model of Kennedy and O'Hagan [52] describe in Eq. 1.1. We rewrite the statistical model below.

$$\boldsymbol{y}^{E}(\boldsymbol{x}) = \boldsymbol{y}^{S}(\boldsymbol{x}, \boldsymbol{\theta}^{\star}) + \boldsymbol{\delta}(\boldsymbol{x}) + \boldsymbol{\epsilon}$$

We can now build a BN for this model as show in Fig. A.2.

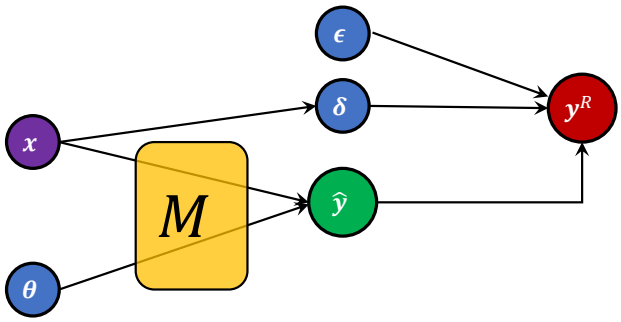

Figure A.2: Bayesian network representation of a calibration problem

A system with two hierarchically built simulation models can be treated by expanding the

network shown in Fig. A.2 as follows. We denote the two models as M_1 and M_2; we get

$$y_1^R = y_1 + \epsilon_1 = \hat{y}_1(\boldsymbol{x}; \boldsymbol{\theta}_1) + \delta_1(\boldsymbol{x}) + \epsilon_1 \tag{A.3}$$

$$y_2^R = y_2 + \epsilon_2 = \hat{y}_2(y_1; \boldsymbol{\theta}_2) + \delta_2(\boldsymbol{x}) + \epsilon_2 \tag{A.4}$$

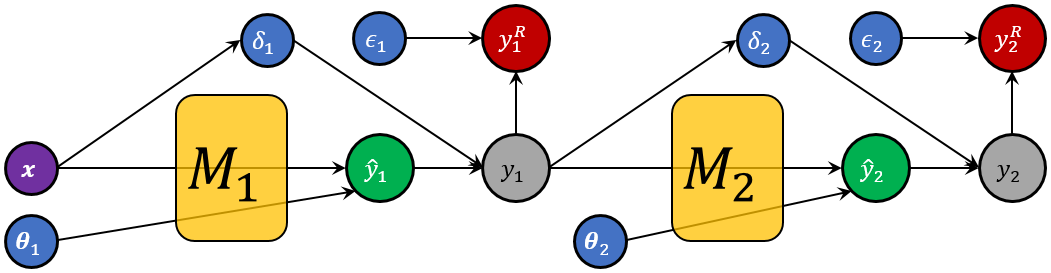

Figure A.3: Bayesian network for a system with two hierarchically built models

APPENDIX B

GLOBAL SENSITIVITY ANALYSIS

In contrast to gradient-based local sensitivities at a chosen nominal value, a global sensitivity analysis uses the probability information of the variable and quantifies both the individual and interactive effects of the various uncertainty sources on the model output uncertainty. This is particularly important in a multi-model calibration in which many uncertain and interrelated parameters are present [168].

Based on the variance decomposition theorem stated in Eq. B, the overall variance in a model output $\hat{y}$ can be decomposed into 1) the variance of the expectation of $\hat{y}$ conditioned on a fixed input θ^i with all other inputs (θ^{-i}) allowed to vary, and 2) the expectation of the variance of $\hat{y}$ conditioned on the same set [20,21]:

$$\mathrm{Var}(\hat{\mathrm{y}}) = \mathrm{Var}_{\theta^{\mathrm{i}}}[\mathbb{E}_{\theta^{-\mathrm{i}}}(\hat{\mathrm{y}}|\theta^{\mathrm{i}})] + \mathbb{E}_{\theta^{\mathrm{i}}}[\mathrm{Var}_{\theta^{-\mathrm{i}}}(\hat{\mathrm{y}}|\theta^{\mathrm{i}})] \tag{B.1}$$

There are two quantities to consider in global sensitivity analysis: the first-order effects and the total effects of θ^i. The first-order effects index quantifies the individual contribution of θ^i to variance in the output $\hat{y}$ and is given as

$$S^i_{1,y} = \frac{\mathrm{Var}_{\theta^{\mathrm{i}}}[\mathbb{E}_{\theta^{-\mathrm{i}}}(\hat{\mathrm{y}}|\theta^{\mathrm{i}})]}{\mathrm{Var}(\hat{\mathrm{y}})} \tag{B.2}$$

In Eq. B, the denominator $\mathrm{Var}\hat{\mathrm{y}}$ is the total variance of a model output $\hat{y}$ considering uncertainty in all parameters θ. In addition to individual contribution, a parameter may contribute additional uncertainty in the output through interactions with other parameters. The total effects index considers the interactions between the ith parameter and all other parameters and is essential to make

informed decisions regarding calibration. The total effects index is given in Eq. B:

$$S^i_{T,y} = 1 - \frac{\mathrm{Var}_{\theta^{-\mathrm{i}}}[\mathbb{E}_{\theta^{\mathrm{i}}}(\hat{\mathrm{y}}|\theta^{-\mathrm{i}})]}{\mathrm{Var}(\hat{\mathrm{y}})} \tag{B.3}$$